

REPORT DOCUMENTATION PAGE			Form Approved OMB No. 0704-0188	
Public reporting burden for this collection of information is estimated to average 1 hour per response, including the time for reviewing instructions, searching existing data sources, gathering and maintaining the data needed, and completing and reviewing the collection of information. Send comments regarding this burden estimate or any other aspect of this collection of information, including suggestions for reducing this burden, to Washington Headquarters Services, Directorate for Information Operations and Reports, 1215 Jefferson Davis Highway, Suite 1204, Arlington, VA 22202-4302, and to the Office of Management and Budget, Paperwork Reduction Project (0704-0188), Washington, DC 20503.				
1. AGENCY USE ONLY (Leave blank)		2. REPORT DATE 29 NOVEMBER 2007		3. REPORT TYPE AND DATES COVERED FINAL REPORT, 04 JUNE 2006 - 03 AUGUST 2007
4. TITLE AND SUBTITLE Microwave Magnetic Materials for Radar and Signal Processing Devices - Thin Film and Bulk Oxides and Metals			5. FUNDING NUMBERS N00014-06-1-0889	
6. AUTHOR(S) Carl E. Patton				
7. Performing organization name(s) and address(es) Department of Physics Colorado State University Fort Collins, CO 80523-1875			8. PERFORMING ORGANIZATION REPORT NUMBER None	
9. SPONSORING/MONITORING AGENCY NAME(S) AND ADDRESS(ES) Office of Naval Research (ONR) 875 North Randolph Street Arlington, VA 22203-1995			10. SPONSORING/MONITORING AGENCY REPORT NUMBER None	
11. SUPPLEMENTARY NOTES The view, opinions and/or findings contained in this report are those of the author(s) and should not be construed as an official Office of Naval Research position, policy, or decision, unless so designated by other documentation.				
12a. DISTRIBUTION/AVAILABILITY STATEMENT Approved for public release; distribution unlimited.			12b. DISTRIBUTION CODE	
13. ABSTRACT (Maximum 200 words) ONR Grant ONR N00014-06-1-0889 has supported a program on new magnetic materials in thin film and bulk form for Navy microwave devices and systems in particular and overall defense applications in general. During the funding period from June 4, 2006 to August 3, 2007, there were numerous accomplishments. Seven archival papers were published on (1) ferromagnetic resonance (FMR) measurements in Permalloy films with an emphasis on the comparison of measurement methods, (2) FMR resonance saturation and Suhl instability processes in Permalloy films, (3) low field effective linewidth in polycrystalline ferrites, (4) Fermi-Pasta-Ulam recurrence for spin wave solitons in yttrium iron garnet (YIG) film strips in a feedback ring system, (5) the Hamiltonian formulation of two magnon scattering microwave relaxation, (6) fundamental properties and structure connections for Fe-Ti-N films, and (7) the detection and analysis of the nonlinear ferromagnetic resonance response in Permalloy films by the magneto-optic Kerr effect. Additional work, not yet published, was done on the FMR response and microscopic loss processes in Co-Cr-Pt thin films, oblique pumping and the nonlinear first order Suhl response in Permalloy films, and the fabrication of barium ferrite - barium strontium titanate ferrimagnetic-ferroelectric heterostructures for multifunctional high frequency devices. (196 words)				
14. SUBJECT TERMS Microwave ferrites, yttrium iron garnet, hexagonal ferrites, polycrystalline ferrites, single crystal ferrites, thin films, ferromagnetic resonance, ferromagnetic resonance linewidth, effective linewidth, spin wave instability, spin wave linewidth, metal alloy films, magneto-optic Kerr effect, Suhl processes, barium ferrite, barium strontium titanate, multiferroic heterostructures.			15. NUMBER OF PAGES 73	
			16. PRICE CODE	
17. SECURITY CLASSIFICATION OF REPORT Unclassified	18. SECURITY CLASSIFICATION OF THIS PAGE Unclassified	19. SECURITY CLASSIFICATION OF ABSTRACT Unclassified	20. LIMITATION OF ABSTRACT UL	

ORGANIZATION COVER PAGE

**FINAL REPORT
to the
UNITED STATES OFFICE OF NAVAL RESEARCH**

**Microwave Magnetic Materials for Radar and Signal
Processing Devices -
Thin Film and Bulk Oxides and Metals**

ONR N00014-06-1-0889, 04 June 2006 - 03 August 2007

Carl E. Patton, Principal Investigator
Department of Physics
Colorado State University
Fort Collins, Colorado 80523

Date of Report:
29 November 2007

Contact Information
Telephone: (970) 491-5083
FAX: (970) 491-7947
E-MAIL: patton@lamar.colostate.edu

20071212109

A. TABLE OF CONTENTS

ORGANIZATION COVER PAGE.....	1
A. TABLE OF CONTENTS.....	2
B. ABSTRACT.....	2
C. RESULTS.....	3
1. Overview	3
2. Education and Human Resources	3
3. ONR EDMR Presentation.....	4
4. Publication list.....	10
Publications	11 - 73

B. ABSTRACT

ONR Grant ONR N00014-06-1-0889 has supported a research program for the development of new materials in thin film and bulk form, and of both the spinel and garnet magnetic oxides as well as high magnetization metallic ferromagnets, for Navy microwave devices and systems in particular and overall defense applications in general. The program has focused on (1) the development of new materials, (2) the elucidation of the loss properties and high power properties of these materials that hold the key to military applications, (3) a new push to incorporate these new magnetic materials into multifunctional systems based on the use epitaxial wide band gap semiconductor and ferroelectric films under development in related ONR programs, and (4) microwave work on new thin film materials and multiferroics. During the funding period from June 4, 2006 to August 3, 2007, there were numerous accomplishments. Seven archival papers were published on (1) ferromagnetic resonance (FMR) measurements in Permalloy films with an emphasis on the comparison of measurement methods, (2) FMR resonance saturation and Suhl instability processes in Permalloy films, (3) low field effective linewidth in polycrystalline ferrites, (4) Fermi-Pasta-Ulam recurrence for spin wave solitons in yttrium iron garnet (YIG) film strips in a feedback ring system, (5) the Hamiltonian formulation of two magnon scattering microwave relaxation, (6) fundamental properties and structure connections for Fe-Ti-N films, and (7) the detection and analysis of the nonlinear ferromagnetic resonance response in Permalloy films by the magneto-optic Kerr effect. Additional work, not yet published, was done on the FMR response and microscopic loss processes in Co-Cr-Pt thin films, oblique pumping and the nonlinear first order Suhl response in Permalloy films, and the fabrication of barium ferrite - barium strontium titanate ferrimagnetic-ferroelectric heterostructures for multifunctional high frequency devices.

C. RESULTS

1. Overview

There are few centers of expertise in the world which are capable of quality research and development work in the area of microwave magnetic materials. The Magnetism Laboratory in the Department of Physics at Colorado State University (CSU), Fort Collins, is well equipped for a wide range of high frequency magnetic measurements at low and high power, at low and high field, over a wide range of frequencies, and as a function of temperature. This team also has the resident expertise to select and investigate the critical materials problems that are relevant to the needs cited above. Much of this infrastructure has been established over the past decade with Office of Naval Research (ONR) support.

Past CSU work has addressed and solved numerous microwave loss and materials problems as they relate to both fundamental understanding and device needs. In the area of ferrites, these include (1) the role of microstructure in the low and high power loss properties of polycrystalline yttrium iron garnet (YIG), (2) the low and high power microwave properties of substituted lithium ferrite materials, (3) the microwave properties of arc plasma spray lithium ferrite, (4) the origins of the large losses in hexagonal ferrite materials for millimeter wave applications, (5) the high power microwave properties of hexagonal ferrite materials, (6) the characterization of liquid phase epitaxy yttrium iron garnet (YIG) films produced with special fluxes, (7) the characterization of ultra dense polycrystalline ferrites for microwave applications prepared by hot isostatic pressing (HIPING) techniques, (8) the growth and characterization of pulsed laser deposited (PLD) ferrite films of YIG and barium hexaferrite with losses which are as good as the best bulk single crystals, and (9) the successful PLD growth of low loss zinc lithium ferrite films.

In the area of metallic ferromagnetic films, which represents a promising system for wide band tunable filters in the microwave and millimeter regime, for example, CSU has been a key contributor to (1) the understanding of phenomenological damping in metal films, (2) the elucidation of microwave loss properties and most recently, (3) a new understanding of the high power properties as well. A significant part of this work has been accomplished during the past and current grant periods under ONR support.

In addition to the above microwave/millimeter wave materials characterization and device physics development work, the Colorado State University program has provided numerous contributions that have advanced the understanding of microwave loss processes and nonlinear spin wave interactions, both for ferrites in general and for thin films in particular. These include (1) a general formulation of the theory of magnetostatic waves in anisotropic magnetic materials, (2) theoretical analysis of spin wave instability processes, both first and second order, for materials with a general ellipsoidal shape, a general anisotropy, and a general pumping field configuration, (3) direct identification of the spin wave interactions responsible for the onset of nonlinear loss in ferrites at high power, and (4) practical theoretical models of the two magnon scattering interaction and calculations of the resulting linewidths and off resonance losses in ferrite materials. A significant part of this work has also been accomplished under ONR support.

The presentation of results in this Final Report is intended to be brief and succinct. Section C.2 lists personnel supported, in whole or in part, by category. Section C.3 contains copies of the slides presented at the annual ONR Electronic Device Materials Review (EDMR) meeting, August 7 - 10, 2007, in Troy, New York. Section C.4 contains a list of the seven archival publications realized during the funding period from June 4, 2006 to August 3, 2007 on this grant.

2. Education and Human Resources

Personnel supported in whole or in part and degrees granted during the current grant period are indicated below:

Visiting scientists:	2
Senior Staff	2
Postdoctoral fellows:	7
Ph. D. Graduate students:	2
Undergraduate students:	3
High school summer apprenticeships:	6

Names, degree specifics, and dates are available on request.

3. ONR EDMR Presentation

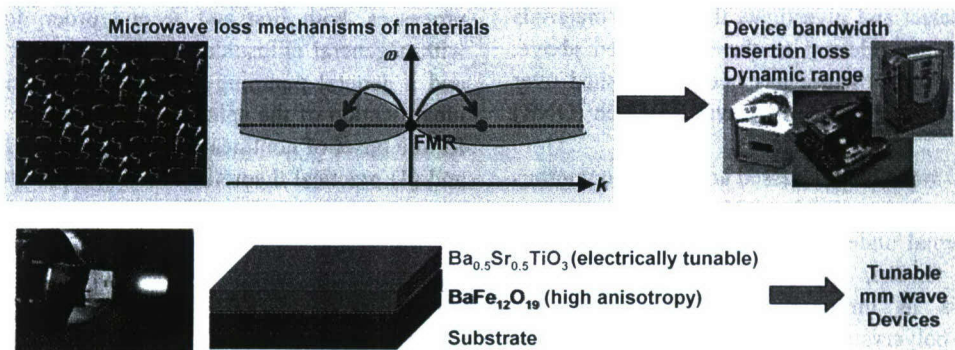
2007 ONR Electronic Device Materials Review Meeting, Troy, New York, August 9, 2007

1

Microwave Nonlinear Dynamics in Magnetic Films

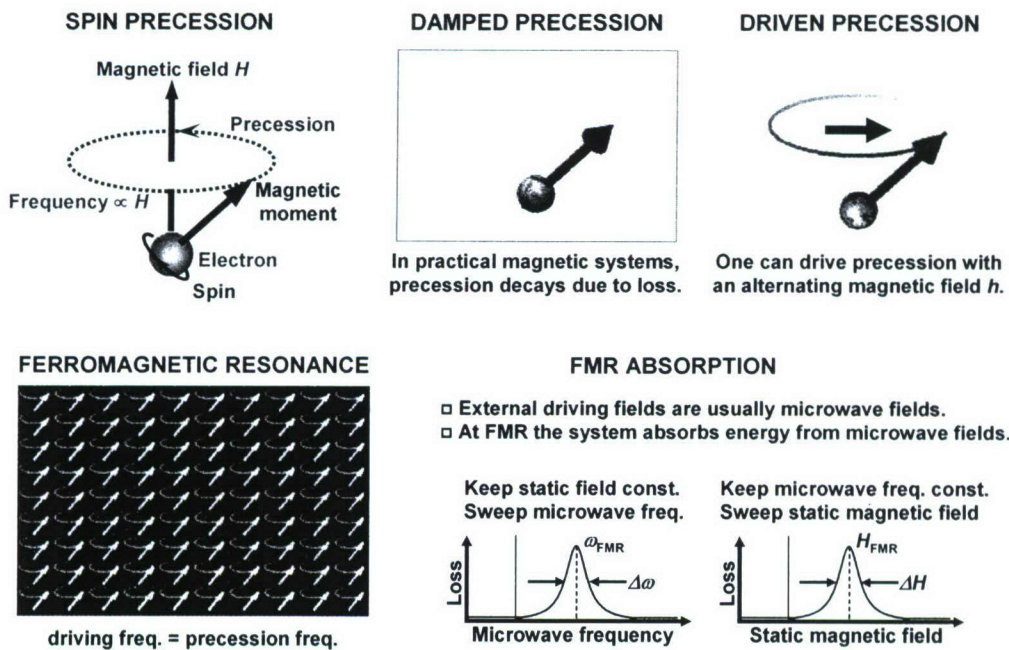
C. Scott Brown, Jaydip Das, Misbah ul Islam, Boris A. Kalinikos, Pavol Krivosik, Nan Mo, Heidi Olson,
Carl E. Patton, Wei Tong, and Mingzhong Wu
Department of Physics, Colorado State University
ONR Program Officer: Dr. Colin Wood

Topic 1: Ferromagnetic resonance linewidth of Co-Cr-Pt films ← Loss at low microwave power
Topic 2: Spin wave parametric excitation in Permalloy thin films ← Loss at high microwave power
Topic 3: Ferrimagnetic-ferroelectric layered structures



Quick Tutorial on Ferromagnetic Resonance (FMR)

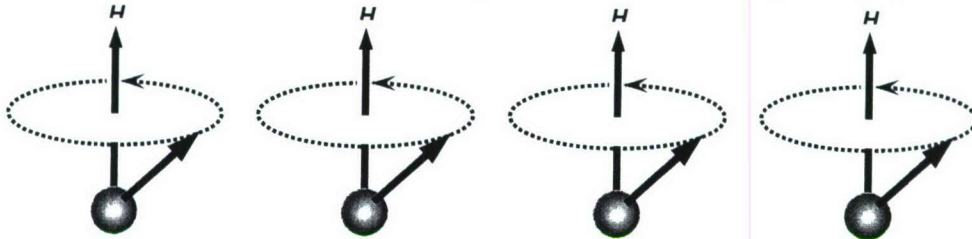
2



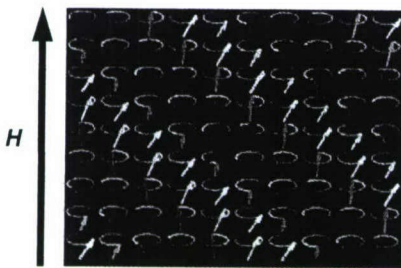
Quick Tutorial on Spin Waves

3

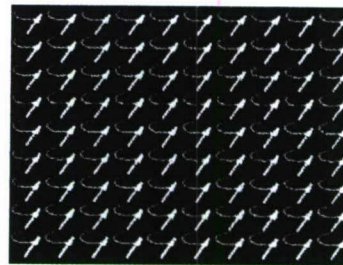
There are dipole interaction and exchange interaction between neighboring spins.



Spin wave animation



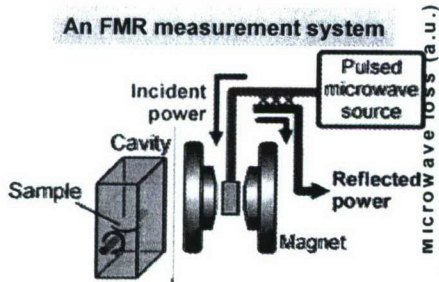
FMR mode – a special spin wave ($k=0$)



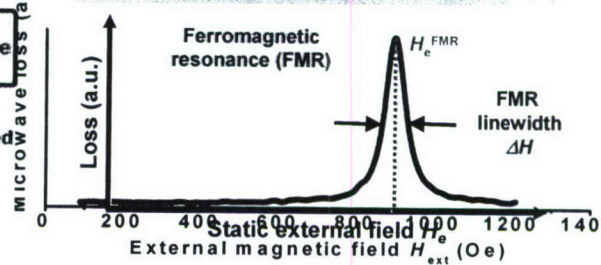
FMR Linewidth Measurement on Co-Cr-Pt Films

4

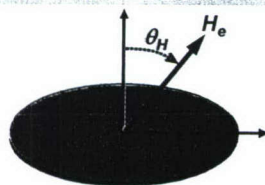
An FMR measurement system



FMR field & FMR linewidth

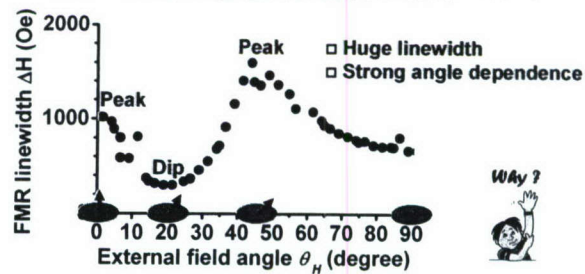


Sample and configuration



- Co_{87%}-Cr_{9%}-Pt_{4%}, 17.5 nm
- $4\pi M_s = 14$ kG; $H_e = 12$ kOe
- Microwave freq.: 9.4 GHz

Change θ_H and measure ΔH

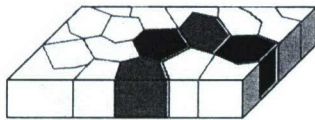


XX

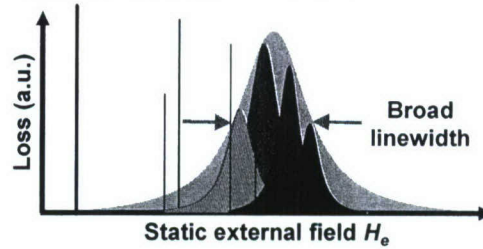
Contribution from Inhomogeneity Line Broadening

5

Local variations in $B_{s\text{-eff}} = 4\pi M_s - H_u$



Local resonances

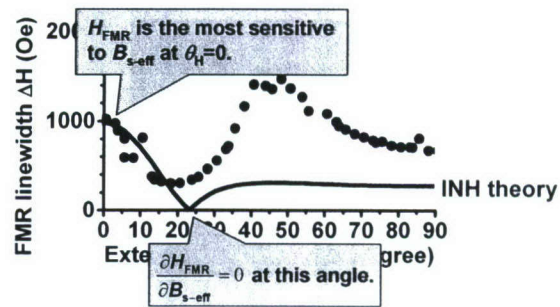


Inhomogeneity (INH) Theory

$$\Delta H_{\text{INH}} \approx \left| \frac{\partial H_{\text{FMR}}}{\partial B_{s\text{-eff}}} \right| \cdot \Delta B_{s\text{-eff}}$$

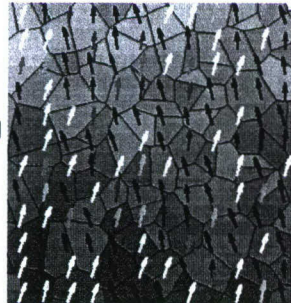
Strongly depends on the direction of the static field.

Net variation $\Delta B_{s\text{-eff}} \approx 980 \text{ Oe}$

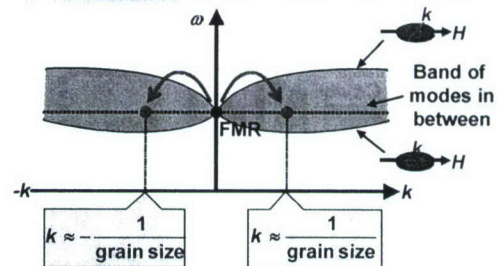


Contribution from Two Magnon Scattering

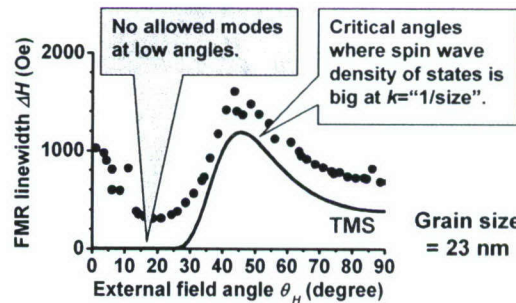
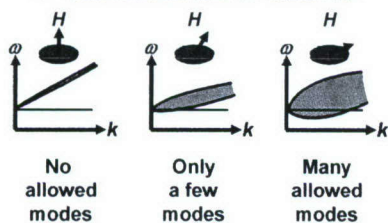
6



Two Magnon Scattering (TMS) Process

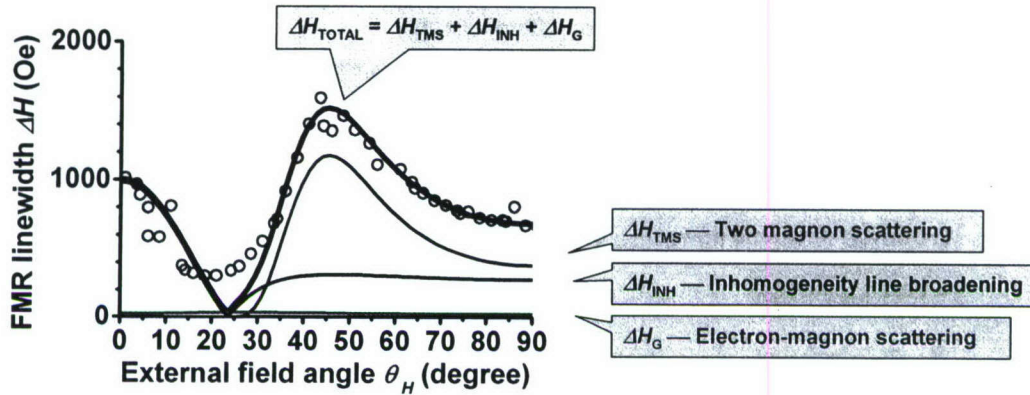


TMS Process changes with θ_H



Total FMR Linewidth

7

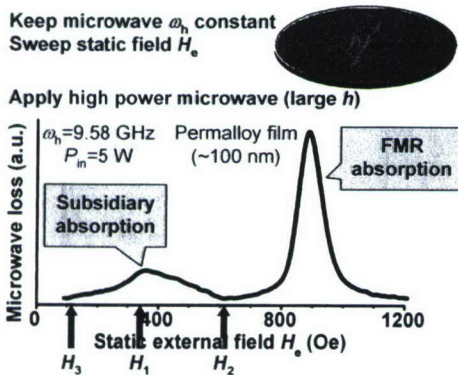


Contributions to FMR linewidth:

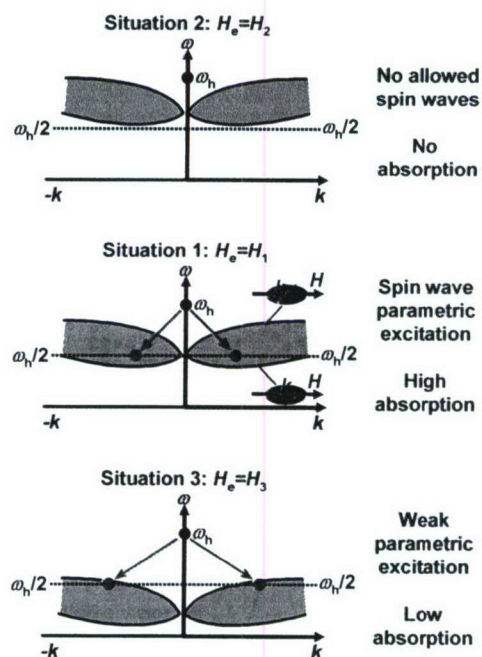
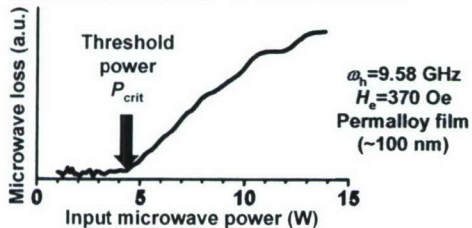
- (1) Grain boundary two magnon scattering — big
- (2) Inhomogeneity line broadening — big but not real loss
- (3) Electron-magnon — intrinsic and small

Parametric Excitation of Spin Waves in Permalloy Films

8

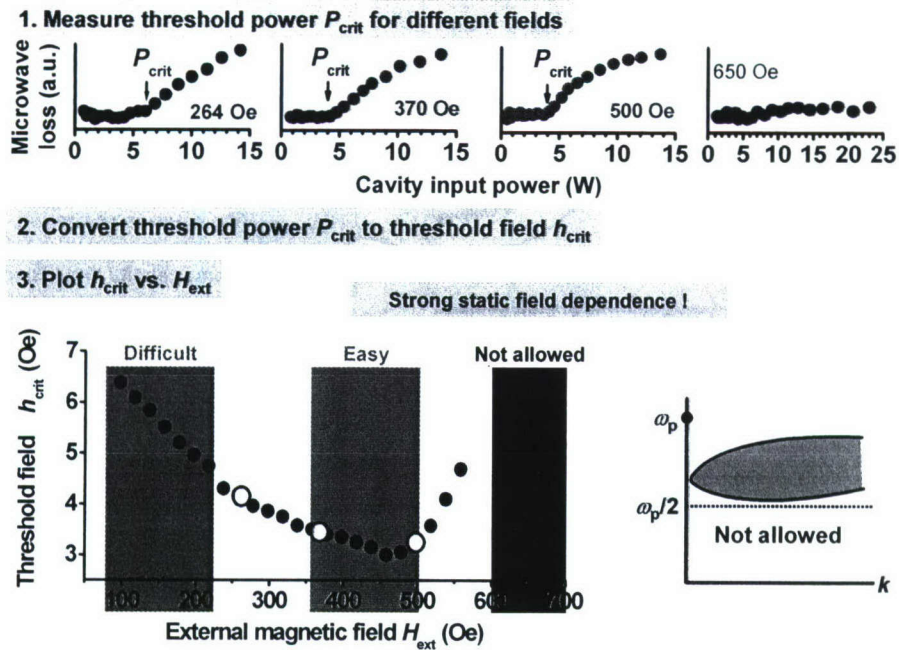


Parametric Excitation – A Threshold Effect



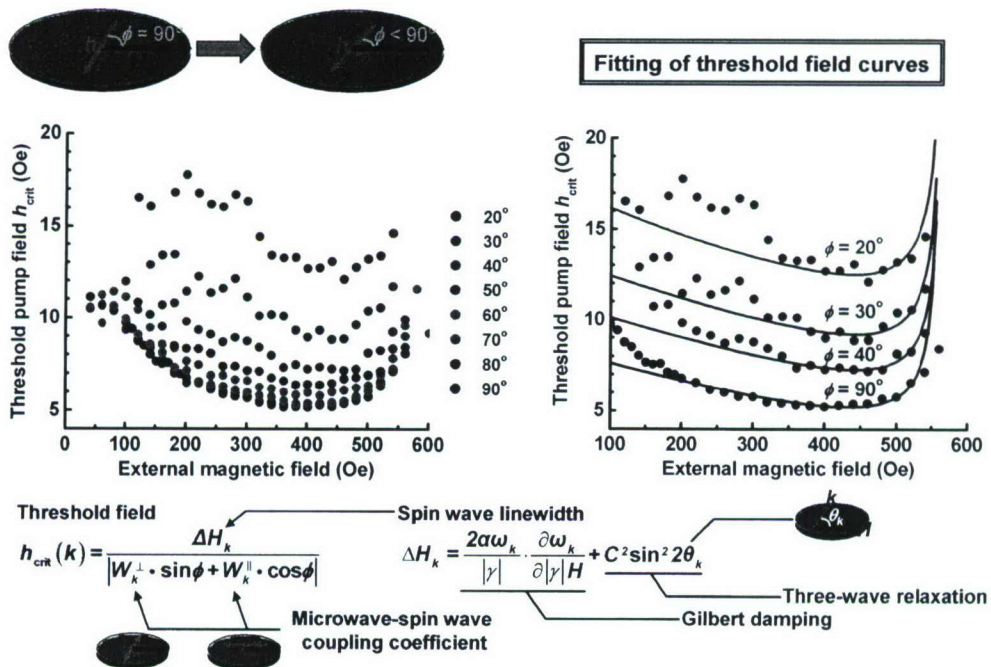
Threshold Microwave Field vs. Static Field

9



Field Angle Dependence & Theoretical Fit

10



Ferrimagnetic-ferroelectric Layered Structures

11

OBJECTIVE

BaM-BSTO layered structure for mm wave devices

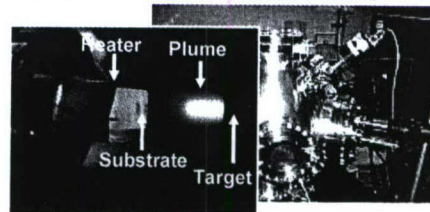


BaM Film
high anisotropy field (~17 kOe)
for mm wave devices

BSTO Layer
electrically tunable
fast, low-power

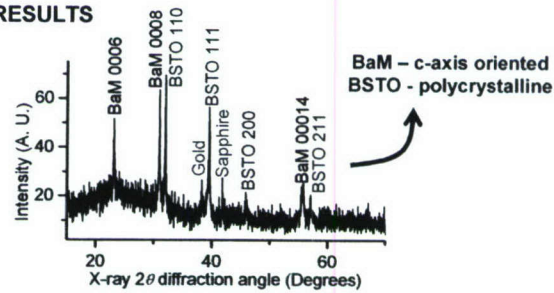
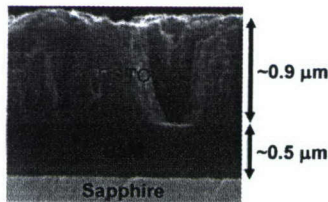
FABRICATION TECHNIQUES

BaM and BSTO layers – pulsed laser deposition



Gold layers – magnetron sputtering

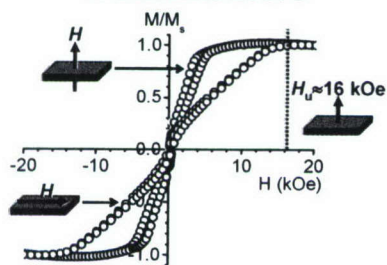
SEM & XRD RESULTS



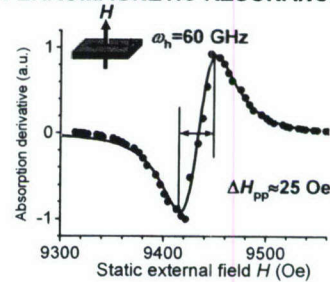
Properties of BaM-BSTO Layered Structures

12

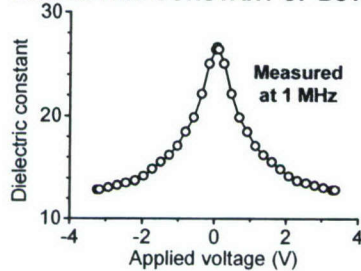
HYSTERESIS LOOPS



FERROMAGNETIC RESONANCE



DIELECTRIC CONSTANT OF BSTO



FUTURE WORK

- (1) Tunability & dielectric loss at mm frequencies
- (2) Electric tuning of magnetic properties
- (3) Barium ferrites with in-plane anisotropy
- (4) Tunable mm wave devices

4. Publication list

"Static and high frequency magnetic and dielectric properties of ferrite-ferroelectric composite materials," S. S. Kalarickal, D. Ménard, C. E. Patton, X. Zhang, L. G. Sengupta, and S. Sengupta, J. Appl. Phys. **100**, 084905-1 to 9 (2006).

"Ferromagnetic resonance linewidth in metallic thin films - comparison of measurement methods," S. S. Kalarickal, P. Krivosik, C. E. Patton, M. L. Schneider, P. Kabos, T. J. Silva, and J. P. Nibarger, J. Appl. Phys. **99**, 093909 1-7 (2006).

"The low field microwave effective linewidth in polycrystalline ferrites," N. Mo, J. J. Green, P. Krivosik, and C. E. Patton, J. Appl. Phys. **101**, 023914-1 to 10 (2007).

"Experimental observation of bona fide Fermi-Pasta-Ulam recurrence in a nonlinear ring system," M. Wu and Carl E. Patton, Phys. Rev. Lett. **98**, 047202-1 to 4 (2007).

"Fundamental magnetic properties and structural implications for nanocrystalline Fe-Ti-N thin films," J. Das, S. S. Kalarickal, K. S. Kim, and Carl E. Patton, Phys. Rev. **B75**, 094435 1 to 11 (2007).

"MOKE-NLFMR - Direct detection of nonlinear ferromagnetic resonance in thin films by the magneto-optic Kerr effect," T. Gerrits, P. Krivosik, M. L. Schneider, C. E. Patton, and T. J. Silva, Phys. Rev. Lett. **98**, 207602 1 to 4 (2007).

"Hamiltonian formalism for two magnon scattering microwave relaxation - theory and applications," P. Krivosik, N. Mo, S. Kalarickal, and C. E. Patton, J. Appl. Phys. **101**, 083901 1 to 13 (2007).

"Ferromagnetic resonance saturation and second order Suhl spin wave instability processes in thin Permalloy films," H. M. Olson, P. Krivosik, K. Srinivasan, and C. E. Patton, J. Appl. Phys. **102**, 023904 1 to 12 (2007).

Static and high frequency magnetic and dielectric properties of ferrite-ferroelectric composite materials

Sangita S. Kalarickal,^{a)} David Ménard,^{b)} Jaydip Das, and Carl E. Patton
Department of Physics, Colorado State University, Fort Collins, Colorado 80523

Xubai Zhang, Louise C. Sengupta, and Somnath Sengupta
Paratek Microwave Inc., Columbia, Maryland 21045

(Received 8 December 2005; accepted 25 July 2006; published online 20 October 2006)

A series of sintered composite materials was fabricated from Parascan™ barium strontium titanate (BSTO) and Trans-Tech nickel zinc ferrite powders. The ferrite loading was varied from zero (BSTO only) to 100 wt % (ferrite only). X-ray diffraction data show the presence of a third, nonmagnetic phase that sets the ferrite loading at values somewhat lower than the as prepared wt % amounts. The average magnetization is found to scale linearly with the loading. The initial susceptibility, saturation field, and coercive force as obtained from hysteresis loop data show trends consistent with these data. Ferromagnetic resonance linewidth and effective linewidth measurements at 10 GHz show reasonable values for the 100 wt % samples, but any amount of BSTO causes a severe degradation in both loss parameters. Similarly, it is found that any amount of ferrite causes a rapid drop in the relative dielectric constant that is consistent with standard mixing models. Loss tangent measurements gave modest values in the 0.001–0.005 range at 1 MHz and much larger values in the 0.02–0.03 range at 10 GHz. © 2006 American Institute of Physics. [DOI: 10.1063/1.2357990]

I. INTRODUCTION

Ferrites and ferroelectric materials are used in a large family of microwave and millimeter wave devices. Ferrite devices typically have high figures of merit, large bandwidths, low insertion loss, and frequency agility.¹ Current ferrite components, however, present two critical problems for advanced system applications: large size and high cost. Ferroelectric components, on the other hand, provide solutions both in size and cost.^{2,3} Size reduction arises from the large relative dielectric constants. These components are also tunable with the application of a modest voltage. Since the tunability is not as good as for ferrites, the voltage tunability and the low cost are advantageous for many applications.

It is likely that ferrite-ferroelectric composites could be used to produce small, low cost, and highly tunable elements for microwave applications. Because of the wide variety of possible applications, there has been considerable interest in composite materials.^{4–14} Previous works on multifunctional ferrite-ferroelectric composite materials have emphasized static magnetization properties^{4,14} and complex permeability and permittivity.¹⁵ The objective of this work was to prepare a series of ferrite-ferroelectric composite materials with a systematic variation in the ferrite loading and to examine the static and high frequency magnetic properties and dielectric properties of these materials. The magnetic component was a standard commercial nickel zinc spinel ferrite (NZF) from Trans-Tech, TT2-111. The ferroelectric component was specially prepared barium strontium titanate (BSTO).

X-ray diffraction (XRD) data indicate that the processing produced a titanium oxide phase in addition to the NZF and BSTO phases. Electrical permittivity measurements indicate changes that scale with loading in a manner that is consistent with electromagnetic mixing models. Static and dynamic magnetic property measurements generally scale with the amount of the ferrite component. The composites generally show high loss, both electrical and magnetic. These results indicate that further work is needed to produce composites that (1) retain the useful low loss properties of the separate phases and (2) yield the additional multifunctionality needed for tunable microwave devices.

The paper is organized as follows. Section II describes the materials preparation and the XRD results. Section III presents room temperature magnetization versus field data for all of the composites and considers these data in terms of a simple model of noninteracting magnetic particles in a nonmagnetic host. Section IV presents ferromagnetic resonance (FMR) results. Section V extends the high frequency analysis to include the microwave response at magnetic fields well above the FMR resonance field. This response is used to determine the high field effective linewidth for the different loadings. Section VI gives basic data on the dielectric properties of the composites. Section VII presents the summary and conclusions.

II. MATERIALS PREPARATION AND X-RAY CHARACTERIZATION

The composite materials consisted of thick disks of Parascan™ tunable dielectric materials, nominally ferroelectric BSTO, with different loadings of the NiZn ferrite. Different nominal weight percentages of the TT2-111 NiZn ferrite powder (0.3, 1, 5, 10, 25, and 50 wt %) were mixed with

^{a)}Present address: Institute für Experimentalphysik, Freie Universität Berlin, Arnimallee 14, 14197 Berlin, Germany; electronic mail: sangita@lamar.colostate.edu

^{b)}Present address: Polytechnique Montréal, Québec, Canada.

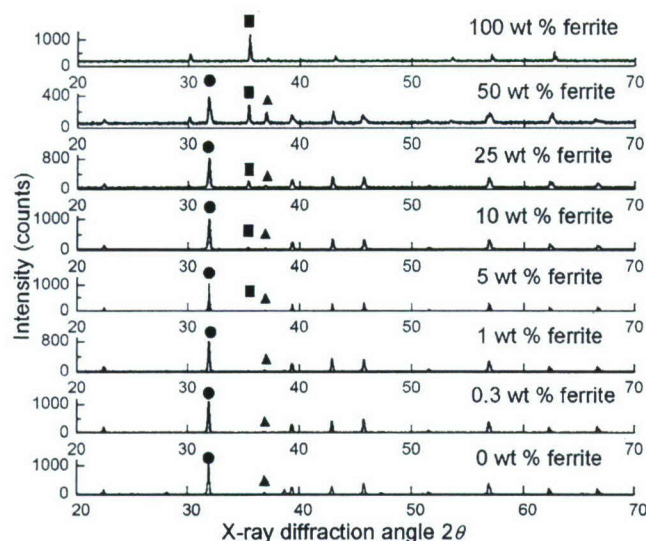


FIG. 1. X-ray diffraction results for all the samples as indicated. The solid circles, squares, and triangles indicate the main peaks for the BSTO, the ferrite phase, and the Ti-O phase.

powders of BSTO materials. In addition, pure TT2-111 powders were independently processed and sintered to produce a fully loaded ferrite reference material. All mixtures were alumina ball milled for 24 h in ethanol. The slurries were then dried and sieved. For each loading, a set of samples was pressed into 1 in. diameter disks and sintered at various temperatures of 1200–1450 °C. A sintering temperature of 760 °C was determined to yield the highest overall density for the pure BSTO material. Disk densities were then measured. Optimum density samples were used for all of the measurements reported below. Sample densities, as measured on the starting cubes for the sphere samples used for the magnetic measurements (see below), ranged from 4.20 to 5.25 g/cm³. There was no apparent correlation between loading and density.

A full x-ray diffraction analysis was done in order to check the phases in the fired materials. The measurements were made with a Bruker AXS system with a copper x-ray source, a scintillation detector, and an angular step size of 0.02°. Figure 1 shows a collage of XRD intensity versus angle of 2θ scans for all the samples. The individual scans are identified by the nominal NZF loading values in wt % for the different samples. In each scan, solid circles and solid squares serve as markers for the main BSTO and NZF diffraction peaks, respectively. The solid triangles mark the peaks that identify the additional Ti-O phase. For the 1 and 0.3 wt % samples, there are no resolved NZF peaks.

These XRD data show that the basic mixing of the BSTO and NZF components of the composite takes place as intended. The size of the BSTO peak decreases somewhat as the ferrite loading is increased, and the NZF peaks increase. The integrity of the peaks also indicates that there is no degradation of these primary phases due to the preparation process. The critical result from the XRD data is in the identification of a small titanium oxide component in the final materials. The magnetic data presented below indicate that this phase has no effect other than an overall dilution. Insofar

as the focus of this work is on magnetic properties, no work has been done to further identify the chemical makeup or the crystallographic nature of this phase.

The effective loading of the ferrite component of the composite in vol %, taken as L , will play an important role in the data presentation and discussion in subsequent sections. The L values for the different samples were deduced from the relative areas under the main peaks for the three phases identified in Fig. 1. Due to the additional titanium oxide phase, the nominal ferrite loadings of 50, 25, 10, and 5 wt % from the preparation process are converted to L values of 27, 16, 6, and 4 vol %, respectively.

Magnetic and microwave measurements were made on spherical samples with nominal diameters of 2 mm. For these measurements, spheres were fabricated from 3 mm cubes cut from the optimum density fired disks. The densities of the individual cubes and spheres were different from the densities measured on the starting disks, with about the same spread as indicated above. These variations in density may be taken as an indication of inhomogeneous starting disks. Two types of pure ferrite samples were also measured. First, the TT2-111 powders were used to fire disks and then fabricate spheres at 100 vol % ferrite loading based on the same procedures given above. Second, fired TT2-111 blocks from Trans-Tech were used to fabricate sphere samples for base line magnetic and microwave measurements.

All dielectric measurements were made directly on as fired disks. The low frequency dielectric measurements were made on 0.064 cm thick and 2 cm diam disks with screen printed with silver electrodes on both faces. The microwave dielectric measurements were made on discs with a 49.5 mm diameter and a thickness of 0.5 mm with no electrodes.

III. STATIC MAGNETIC PROPERTIES

Static magnetic induction versus field data were obtained by vibrating sample magnetometry at room temperature for applied fields up to 5 kOe. The data below are given in terms of the magnetic induction $4\pi M$. Volumes were calculated from the densities of the fired disks and the masses of the individual samples. Cubes and spheres gave similar results for all the loadings. The specific data below for the materials with partial ferrite loadings were obtained on spheres. Figures 2–4 show data on the saturation induction versus loading, data on magnetization versus field, and various hysteresis loop parameters versus loading, respectively. Considered as a whole, these data show that the static magnetic response is consistent with a model of a composite medium with an unmodified ferrite phase in a nonmagnetic matrix.

Figure 2 shows the data on average saturation induction $\langle 4\pi M \rangle_{\text{sat}}$ data versus the ferrite loading L . These measurements were made at an external field of $H=5$ kOe. As the hysteresis data in Fig. 3 will show, a 5 kOe field was sufficient to achieve magnetic saturation. The solid circles show the data for the composite samples. The solid square shows the saturation induction for the TT2-111 reference sphere. The solid line shows the linear response one would expect for an unmodified ferrite phase with a saturation induction value the same as that obtained for $L=100$ vol %.

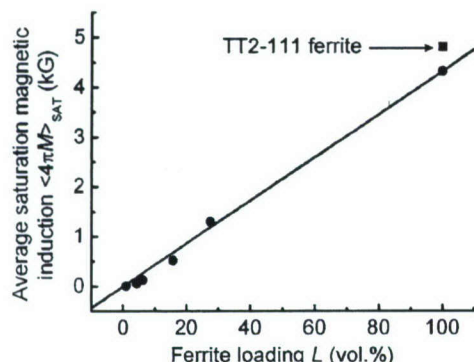


FIG. 2. Average saturation magnetic induction $\langle 4\pi M \rangle_{\text{sat}}$ as a function of ferrite loading L . The data were obtained for an applied magnetic field of 5 kOe. The solid circles show the data for the composites. The solid square shows the value for the commercial TT2-111 ferrite. The solid line shows the linear response expected for an unmodified ferrite phase.

These data serve to make two important points. First, the $\langle 4\pi M \rangle_{\text{sat}}$ value of 4.3 kG at $L=100$ vol % is close to the $\langle 4\pi M \rangle_{\text{sat}}$ value for the standard TT2-111 material. This indicates that the preparation process maintained the basic NZF properties. Second, the data show that the magnetic induction of the sample scales linearly with the ferrite loading. This confirms that the basic ferrite properties for the composite samples were also maintained.

Figure 3 shows full hysteresis loop data on the average magnetic induction $\langle 4\pi M \rangle$ as a function of the applied magnetic field H from -5 to $+5$ kOe for L values of 4, 6, 16, 27, and 100 vol %. One sees that all of the samples show a clear saturation at some loading dependent $\langle 4\pi M \rangle_{\text{sat}}$ value for fields above 1–2 kOe. As noted above, these $\langle 4\pi M \rangle_{\text{sat}}$ values scale linearly with L .

The Fig. 3 data serve to make two further points. First, from the outward shift in the knee of the hysteresis curves, one can see that the saturation field increases with loading. The 4 and 6 vol % samples have saturation fields well below 500 Oe. For the 100 vol % sample, one has a saturation field $H_{\text{sat}} \approx 1.2$ – 1.4 kOe. This H_{sat} value for the pure ferrite is very close to one-third of the measured $\langle 4\pi M \rangle_{\text{sat}}$. This means

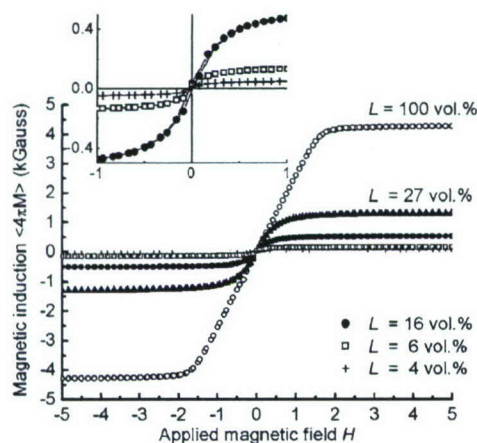


FIG. 3. Average magnetic induction $\langle 4\pi M \rangle$ as a function of the applied magnetic field H for the different ferrite loadings, as indicated. The inset shows an enlarged view for samples with loadings of $L=4$, 6, and 16 vol %.

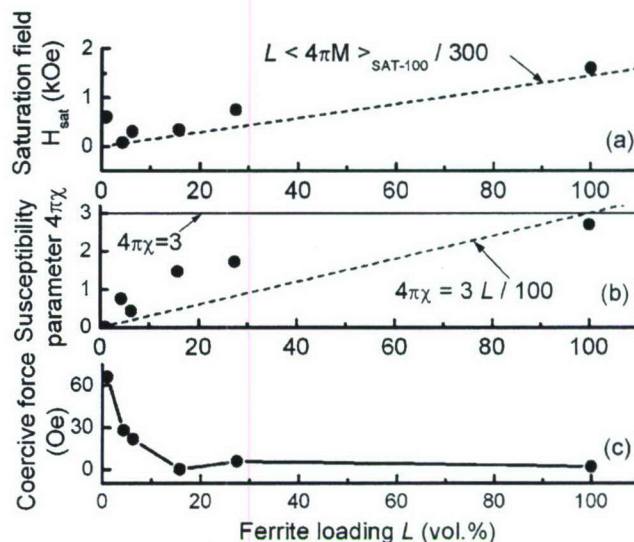


FIG. 4. Saturation field H_{sat} , initial susceptibility $4\pi\chi$, and coercive force H_C as functions of ferrite loading L . The solid circles in (a) show the saturation field data. The dashed line corresponds to $H_{\text{sat}} = L \langle 4\pi M \rangle_{\text{sat-100}} / 300$, where $\langle 4\pi M \rangle_{\text{sat-100}}$ is the $\langle 4\pi M \rangle_{\text{sat}}$ value for the 100 vol % sample. The solid circles in (b) show the susceptibility parameter data. The solid line corresponds to $4\pi\chi = 3$ and the dashed line corresponds to $4\pi\chi = 3L/100$. The solid circles in (c) show the coercive force data.

that the 100 vol % sample behaves as expected from simple demagnetizing field considerations. The lower H_{sat} values for the lower loadings indicate that it is the average mean field saturation induction of the sample as a whole, rather than the saturation induction of the individual NZF grains, that defines the saturation point. If the NZF grains defined the measured H_{sat} , all of the samples would saturate at $H \approx \langle 4\pi M \rangle_{\text{sat-100}} / 3$, where “sat-100” refers to the $\langle 4\pi M \rangle_{\text{sat}}$ for $L=100$ vol %. This is discussed in further detail below.

Second, consider the $\langle 4\pi M \rangle$ vs H response in the $H \rightarrow 0$ limit. The slope of this low field response corresponds to $4\pi\chi$, where χ is the initial susceptibility. The data show that as the loading is reduced, the $4\pi\chi$ values also decrease. An effective medium comprised of noninteracting magnetically soft spherical particles would saturate at a field equal to one-third of the saturation induction value. This means that for independent spherical ferrite particles of any kind, the $4\pi\chi$ should depend only on the loading and vary as $3L/100$. Further discussion will follow below.

Figure 4 shows results on H_{sat} , $4\pi\chi$, and the coercive force H_C as a function of L , based on the data in Fig. 3. Graph (a) shows H_{sat} values obtained from the extrapolated low field responses shown in Fig. 3 to the $\langle 4\pi M \rangle_{\text{sat}}$ points for each data set. These data are shown by the solid circles. The dashed line corresponds to a linear change in H_{sat} according to $H_{\text{sat}} = L \langle 4\pi M \rangle_{\text{sat-100}} / 300$, where $\langle 4\pi M \rangle_{\text{sat-100}}$ is the $\langle 4\pi M \rangle_{\text{sat}}$ value for the 100 vol % sample. Graph (b) shows the $4\pi\chi$ results. The data are shown by the solid circles. The solid line corresponds to the value of $4\pi\chi = 3$ expected for a spherical ferrite phase. The dashed line shows the linear $4\pi\chi = 3L/100$ response expected for independent ferrite spherical grains. Graph (c) shows the coercive force data. The solid line simply connects the data points.

Apart from the sample with the lowest ferrite loading,

the H_{sat} data in Fig. 4(a) show a nearly linear increase with L and an end point value at $L=100$ vol % that is close to $\langle 4\pi M \rangle_{\text{sat}}/3$. The linear response shown by the dashed line is what one would expect from a mean field model, that is, a sample with strongly coupled magnetic particles that acts like a uniformly magnetized material with an $\langle 4\pi M \rangle_{\text{sat}}$ equal to $\langle 4\pi M \rangle_{\text{sat-100}}/100$ and $H_{\text{sat}} = \langle 4\pi M \rangle_{\text{sat}}/3$. The fact that the data lie slightly above the dashed line is an indication that the coupling is not perfect and a mean field model is not strictly applicable. Fully noninteracting particles would give an L -independent H_{sat} equal to $\langle 4\pi M \rangle_{\text{sat-100}}/3$ for all samples.

The $4\pi\chi$ data in Fig. 4(b) show an increase with loading, but the points generally fall well above the linear response line. Interactions between the spherical particles would give an L -independent susceptibility value of 3. Completely independent ferrite inclusions, on the other hand, would give a linear dependence of susceptibility on L . The somewhat larger than linear $4\pi\chi$ values for intermediate L values indicate, therefore, that there may be some level of interaction between the ferrite particles.

The H_C data in Fig. 4(c) show a small coercive force at large loadings and a rapid increase when one drops below $L=16$ vol %. The small values at the large loadings are consistent with the properties of the original TT2-111 material and support the existence of essentially unmodified ferrite grains in the composites down to $L=16$ vol % or so. However, it is not clear why there is such a drastic increase in the coercive force as the loading is reduced below 16 vol %.

IV. FERROMAGNETIC RESONANCE RESPONSE

FMR and high field effective linewidth techniques were used to characterize the microwave losses. This section presents the FMR results. Section V gives the high field effective linewidth results. The FMR profiles were measured by a shorted waveguide reflection technique at an operating frequency f of 9.5 GHz. Measurements were made on nominal 1 mm diameter spheres for the TT2-111 and the 100 vol % materials and nominal 3 mm diameter spheres for the materials with lower loadings. The samples were mounted at the center of the waveguide cross section on a Rexolite® rod and positioned a half wavelength from an adjustable short. The additional loading introduced by the samples at the FMR loss point in field was so small that field modulation and lock-in detection methods were needed to observe the response. The raw data consisted of profiles of the uncalibrated field derivative of the FMR absorption versus field. Absorption profiles of loss versus field were obtained from direct integration of the raw data. These integrated data were then used to determine the resonance field peak position H_{FMR} and the half power linewidth ΔH_{FMR} .

The FMR derivative profiles for the TT2-111 and 100 samples were well resolved and close to the general response expected from dense nickel zinc ferrite materials. The data for the 27 and 16 vol % samples, however, showed that any appreciable drop in the ferrite loading below 100 vol % causes a large degradation in the FMR response. This con-

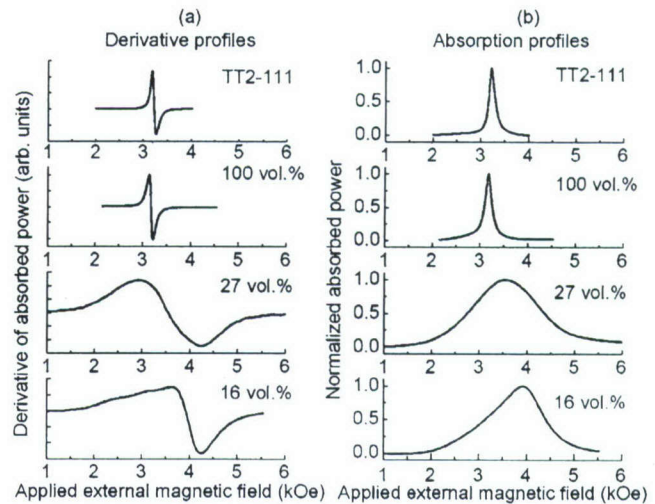


FIG. 5. Ferromagnetic resonance profiles at 9.5 GHz. The (a) graphs show the measured derivative of the absorbed power vs applied magnetic field profiles for the TT2-111, 100, 27, and 16 vol % samples, as indicated. The (b) graphs show the integrated profiles for the derivative profiles in (a).

clusion is carried over to the extreme for the samples with smaller loadings. These samples showed no recognizable FMR response.

Figure 5 shows the actual FMR data in two formats. The (a) graphs show the measured derivative of the absorbed power versus applied magnetic field profiles for the TT2-111 and $L=100$, 27, and 16 vol % samples, as indicated. The (b) graphs show the integrated profiles for the derivative profiles in (a). The absorption profiles in (b) have all been scaled to give a peak absorption value of unity. Both the raw data and the integrated profiles show that the FMR lines are narrow and symmetric for the TT2-111 and 100 vol % samples. These line shapes are near Lorentzian. On the other hand, for the 27 and the 16 vol % samples, the absorption profiles are broad and distorted, and nowhere near Lorentzian in shape. One can also see that the peaks for the 27 and the 16 vol % samples are also shifted up in field relative to the FMR positions for the two dense samples.

Table I summarizes the basic FMR parameters obtained from the measurements, namely, the FMR field H_{FMR} , the effective gyromagnetic ratio γ_{eff} expressed in frequency units as $|\gamma_{\text{eff}}|/2\pi$, the FMR half power linewidth ΔH_{FMR} , and the high field effective linewidth ΔH_{eff} . The samples are listed according to the vol % loading L values from the XRD data. The FMR field is taken at the peak loss point in the (b)

TABLE I. Summary of 9.5 GHz ferromagnetic resonance (FMR) and effective linewidth measurement results.

Vol % ferrite loading L	FMR field H_{FMR} (Oe)	Effective gyromagnetic ratio $ \gamma_{\text{eff}} /2\pi$	FMR linewidth ΔH_{FMR} (Oe)	High field effective linewidth ΔH_{eff} (Oe)
100 (TT2-111)	3223	2.95	157	6
100	3175	2.99	168	8
27	3549	2.68	1596	97
16	3924	2.42	1260	480
6	367

graphs in Fig. 5. For spherical samples, $|\gamma_{\text{eff}}|/2\pi$ is equal to f/H_{FMR} .¹⁶ For electron based atomic moment systems, γ_{eff} is negative. For spin only moments with a Landé g factor of 2, $|\gamma_{\text{eff}}|/2\pi$ is equal to 2.8 GHz/kOe. The linewidth ΔH_{FMR} is taken as the full width at half maximum of the profiles in (b). The ΔH_{eff} results are considered in the next section.

The table shows that the FMR fields for the TT2-111 and the 100 vol % are close to 3.2 kOe and the corresponding $|\gamma_{\text{eff}}|/2\pi$ values of about 3 GHz/kOe are slightly higher than the free electron value. These samples also show relatively narrow linewidths in the 150–170 Oe range. These represent typical FMR parameters for dense ferrite materials. This situation is not maintained for the samples with lower ferrite loadings. Here one finds higher FMR fields and much lower $|\gamma_{\text{eff}}|/2\pi$ values than one would expect for any reasonable ferrite. At the same time, one sees large departures from a Lorentzian line shape and very large increases in the linewidths by a factor of 10 or so. Such a behavior indicates irregularly shaped ferrite inclusions along with complicated interparticle dipolar interaction.

It is evident that a simple change in the ferrite loading has a drastic effect on the FMR response for these composite materials. The data show that any reduction in the ferrite loading below the 100 vol % level serves to degrade the FMR response rather severely. It is worthwhile to consider two possibilities, among many, for this degradation. First, it is likely that the imbedding process yields ferrite particles with irregular shapes, large strains, and impurities. All of these factors are known to produce large linewidths. Second, in the extreme view, one can consider the composite as a polycrystalline ferrite with a very large porosity. It is well known that even a small amount of porosity in a ferrite material can produce a large inhomogeneously broadened line. Typical porosity broadened half power linewidths for spinel ferrites at 10 GHz are in the 30–40 Oe per percent.

It may also be noteworthy that for the $L=16$ vol % sample, the FMR absorption profile is also highly distorted. The indication here is that for dilute loadings, the factors enumerated above result in more than a simple line broadening. Details of the origins of these distortions are not yet clear.

V. HIGH FIELD EFFECTIVE LINEWIDTH

The FMR results presented in the previous section show that any amount of ferroelectric loading causes a severe degradation of the linewidth. This section considers the microwave loss as measured at high field rather than at ferromagnetic resonance. In conventional ferrites, one can use high field measurements of the so-called effective linewidth to determine near intrinsic losses even when the FMR linewidth is broadened by microstructure effects or inhomogeneities of various types.¹⁷ This section presents the results of similar measurements on the present ferrite-ferroelectric composite materials.

The high field microwave response was evaluated for the composites for a field range of 5–11 kOe at 10 GHz, and high field effective linewidth determinations were made from these data. Reasonable results were obtained for the samples

with 6, 16, 27, and 100 vol % loadings. For the samples with lower L values, the high field losses were too large to obtain meaningful determinations of the effective linewidth. Section V A introduces the working equations for the high field microwave response and the effective linewidth analysis, and provides brief experimental details for the composite materials measurements. Section V B gives the experimental results.

A. Experimental procedure and data analysis

The effective linewidth technique is based on measurements of the change in the frequency f and quality factor Q with field for a high Q cylindrical microwave cavity with the magnetic sample in place. Typically, the measurement is made with applied fields well above the FMR field. For such high fields, the spin wave band is shifted well above the nominal cavity and signal frequency. This eliminates, in principle, any contribution to the magnetic losses due to any inhomogeneities that may be present in the sample.

Such measurements allow one to access the high field tail of the FMR response and determine the relaxation rate η for the driven mode that is applicable in the high field regime. Expressed in linewidth units, one can write an effective linewidth parameter $\Delta H_{\text{eff}} = 2\eta/|\gamma|$. This ΔH_{eff} simply expresses the relaxation rate in field units for convenient comparison with actual linewidth data. For simplicity, the conversion from a relaxation rate to ΔH_{eff} uses the free electron gyromagnetic ratio γ rather than the γ_{eff} introduced in Sec. IV. The difference is small. In the high field regime of loss, the intrinsic γ is also more applicable.

For a typical polycrystalline ferrite, one may have a 10 GHz FMR linewidth in the 100–200 Oe range, while the high field effective linewidth will be in the 10–20 Oe range. In the case of very dense ferrites, one finds that ΔH_{eff} approaches intrinsic single crystal linewidth values in the limit of very high fields. As the results below will show, the effective linewidth situation for ferrite-ferroelectric composite materials is more complicated.

Reference 18 provides a full description of the high field effective linewidth analysis procedure for materials in which one finds a constant ΔH_{eff} in the high field regime.¹⁸ This is the applicable situation here. The sample is placed in the center of a TE_{011} cavity with a high Q , typically in the 20 000 range. The cavity frequency f and quality factor Q are then measured as a function of the field H in the high field regime, and the data are analyzed to obtain a high field ΔH_{eff} parameter. The analysis procedure is summarized below. Details of the measurement procedure as it applies to the present composite samples are given at the end of the section.

The working cavity response equations may be written as

$$f = f_{\infty} - KX_F(H, f) \quad (1)$$

and

$$\frac{1}{Q} = \frac{1}{Q_{\infty}} + K\Delta H_{\text{eff}}X_Q(H, f). \quad (2)$$

In the above, f_∞ and Q_∞ denote the cavity frequency and quality factor, respectively, in the limit of very high fields. In this limit, the magnetic response is essentially frozen out. The K parameter takes the form

$$K = C \frac{V_m}{V_{\text{cav}}}, \quad (3)$$

where V_m denotes the active magnetic volume of the sample, C is a fixed parameter that depends on the cavity dimensions and cavity mode, and V_{cav} is the cavity volume. For the cavity used for this work, C/V_{cav} is equal to 0.109 cm^{-3} .

The $X_F(H, f)$ and $X_Q(H, f)$ denote field and frequency dependent dispersion and absorption parameters, respectively. In the case of an isotropic spherical magnetic sample, these parameters may be written as

$$X_F(H, f) = \frac{4\pi M_S H f}{H^2 - (f/|\gamma|)^2} \quad (4)$$

and

$$X_Q(H, f) = \frac{4\pi M_S [H^2 + (f/|\gamma|)^2]}{[H^2 - (f/|\gamma|)^2]^2}, \quad (5)$$

where $4\pi M_S$ is the saturation magnetic induction value for the magnetic sample. For composites, it is a reasonable choice to set $4\pi M_S$ equal to $\langle 4\pi M \rangle_{\text{sat-100}}$, since it is the uniform mode microwave response of the ferrite phase that defines the response equations listed above. Note that in the high field limit in which $H^2 \gg (f/|\gamma|)^2$ is satisfied, typically for fields above 5–6 kOe or so, the $X_F(H, f)$ scales essentially as $1/H$ and $X_Q(H, f)$ scales as $1/H^2$. The plots to be considered shortly for f vs $X_F(H, f)$ and $1/Q$ vs $X_Q(H, f)$ should be considered in this light.

From Eq. (1), one can see that the slope of the line obtained from a plot of the measured cavity frequency as a function of $X_F(H, f)$ will correspond to $-K$. From Eq. (2), one can also see that the slope of the plot of $1/Q$ as a function of $X_Q(H, f)$ will correspond to $K\Delta H_{\text{eff}}$. The ratio of the two slopes will then yield the high field effective linewidth ΔH_{eff} .

The data to be presented in the next section confirm that such linear f vs $X_F(H, f)$ and $1/Q$ vs $X_Q(H, f)$ responses are obtained for the series of composite samples of interest here. For ferrite-ferroelectric composites, however, it is also important to consider the way in which the K parameter scales with the sample mass and ferrite loading L . For the current samples, one may write the active magnetic volume as $V_m = V_s L/100$, where V_s is the density of the ferrite component. Based on this relation, one obtains a K parameter to sample volume ratio as

$$\frac{K}{V_s} = 0.00109L. \quad (6)$$

This simple connection provides a simple test of the effect of loading on the cavity frequency response. The volume to the measured samples ranged from 0.0722 to 0.2486 cm^3 .

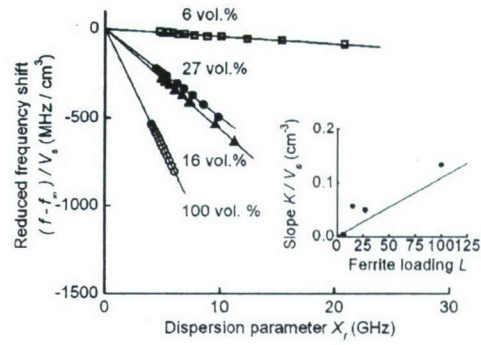


FIG. 6. Reduced cavity frequency shift $(f - f_\infty)/V_s$ as a function of the dispersion parameter X_F for the different ferrite loadings, as indicated. The solid lines show linear fits to the different data sets. The inset shows the response slope parameter K/V_s as a function of the ferrite loading L . The solid circles in the inset show the slopes of line fits in the main graph, and the line shows the calculated theoretical response based on microwave perturbation theory.

B. High field effective linewidth results

Figure 6 shows measurement results for the cavity frequency shift as a function of field. The data in the main graph are shown in an $(f - f_\infty)/V_s$ vs X_F format for the 6, 16, 27, and 100 vol % samples, as indicated. The solid lines show linear fits to the different data sets. The solid points in the inset show the slopes of line fits as a function of the loading L for the different samples, and the straight line shows the expected slope response from Eq. (6).

The X_F values were obtained from the raw f vs H data and Eq. (4). The $(f - f_\infty)/V_s$ format for the vertical axis display was used so that all the data for the samples with different loadings could be compared in a consistent manner. While the extrapolated f_∞ values vary from sample to sample, depending on the overall cavity loading, a display based on $(f - f_\infty)/V_s$ will extrapolate to a vertical axis value of zero in the $X_F = 0$ limit. From Eq. (6), one sees that the K parameter scales with the sample volume V_s . The slope of a given $(f - f_\infty)/V_s$ vs X_F plot, therefore, should scale with the loading L .

All of the data plots in Fig. 6 confirm the expectation from Eq. (1) that $(f - f_\infty)/V_s$ is a linear function of X_F with a negative slope. The general trend of the slopes from these plots to scale with the loading L , with the notable exception of $L = 16$ vol %, is also consistent with the expectation from Eqs. (1) and (6). The slope results in the inset make this trend quantitative and show that the response is reasonably close (except for the $L = 16$ vol % point) to the solid line result from perturbation theory. The fact that the fitted slope values from the data fall about 10 vol % above the solid line is consistent with sample loading effects measured by Truedson *et al.*¹⁸

It is not clear why the $(f - f_\infty)/V_s$ vs X_F response for the 16 vol % sample should be so anomalous. There is no inconsistency in the corresponding static magnetization versus field data that would point to such a large anomaly in the off-resonance microwave response.

Figure 7 shows corresponding results on the inverse cavity Q factor as a function of field. The data in the main graph are shown in a $(1/Q - 1/Q_\infty)/K$ vs X_Q format for the same

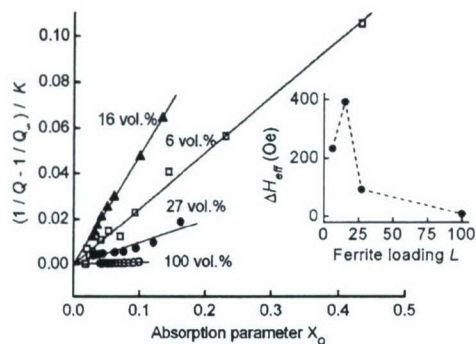


FIG. 7. Reduced sample loss parameter $(1/Q - 1/Q_\infty)/K$ as a function of the absorption parameter X_Q for the different loadings of the ferrite, as indicated. The inset shows the calculated effective linewidth ΔH_{eff} as a function of ferrite loading L .

samples as those used for the data in Fig. 6. The format is the same as for Fig. 6. The solid lines show linear fits to the different data sets. The solid points in the inset shows the slopes of line fits as a function of the loading L for the different samples.

The X_Q values were obtained from the raw f vs H data and Eq. (5). The $(1/Q - 1/Q_\infty)/K$ format for the vertical axis display was used so that the data for the samples with different loadings could be compared in a consistent manner. For a linear $(1/Q - 1/Q_\infty)/K$ vs X_Q response, moreover, one can see from Eq. (2) that the slope for a given data set corresponds directly to the high field effective linewidth ΔH_{eff} .

All of the data plots in Fig. 7 confirm the expectation from Eq. (2) that $(1/Q - 1/Q_\infty)/K$ is a linear function of X_Q with a positive slope. This means, as noted above, that one has a well defined high field effective linewidth that corresponds to the slope of the response for each data set. As the inset to Fig. 7 shows, with the exception of the data for $L = 16$ vol %, there is a general trend in these slopes, and hence ΔH_{eff} , to decrease as the loading is increased. The actual fits give relatively small effective linewidth values of 8 Oe at $L = 100$ vol %, 93 Oe at $L = 27$ vol %, and 392 Oe at $L = 16$ vol %, and 232 Oe at $L = 6$ vol %. As a point of reference, the TT2-111 material had $\Delta H_{\text{eff}} = 6$ Oe. It is important to note that the anomalously large slope and corresponding ΔH_{eff} value of 392 Oe for the $L = 16$ vol % sample is not a carryover from the anomaly noted for the $(f - f_\infty)/V_s$ vs X_F response discussed above. This anomaly is normalized out by the K divisor in the vertical axis display used for Fig. 7. This anomalously large ΔH_{eff} provides evidence in its own right that there is something problematic about this sample. These ΔH_{eff} values are the same as those listed in Table I.

There are several effects that are passed over in the $(1/Q - 1/Q_\infty)/K$ vs X_Q display format used for Fig. 7. This relates to the actual values of the high field Q that lead to the $1/Q_\infty$ offset in the first place. It was found that a decrease in loading to the 16 or 6 vol % level caused a significant drop in the Q_∞ values for the cavity. Typical Q_∞ values for the cavity with the TT2-111 sample, the 100 vol % composite, were in the 20 000–22 000 range. It is interesting to note that even a drop in loading to 27 vol % caused only a drop in Q_∞ value to about 20 000. These values amount to a very small degradation from the nominal empty cavity Q of 22 500 or

so. For the 16 and 6 vol % loading samples, however, the Q_∞ is degraded to about 7000 and 5000, respectively.

The fact that the K/V_s value for the $L = 6$ vol % sample, as shown in the Fig. 6 inset, is consistent with the corresponding values for the 27 and 100 vol % samples indicates that the drop in Q did not affect the cavity calibration. It is possible, however, that the factor of 4 ΔH_{eff} increase in going from $L = 27$ vol % to $L = 6$ vol % could be due to the same process that causes the factor of 4 drop in Q_∞ . It is possible that the large ferroelectric component introduces Ohmic losses that affect both Q_∞ and ΔH_{eff} . Truedson *et al.*¹⁸ have shown that Ohmic losses in a ferrite disk can give the appearance of a contribution to the high field ΔH_{eff} .

VI. DIELECTRIC PROPERTIES

Three specific dielectric properties as a function of loading were measured: the dielectric constant, the loss tangent ($\tan \delta$), and the electric field tunability. Measurements of the dielectric constant and dielectric loss tangent were made at 1 MHz and 10 GHz. The 1 MHz measurements were made with a Hewlett Packard (HP) impedance gain/phase analyzer.¹⁹ The 10 GHz measurements were obtained with a 10 GHz cavity resonator and a HP vector network analyzer. The tunability determinations were based on measurements at 1 MHz of a change in capacitance with applied voltage for the electroded disk samples discussed in Sec. II. For the present purposes, the tunability is taken as $T = \delta C/C$, where C is the nominal capacitance at zero voltage and δC is the measured change.

Table II and Figs. 8–10 summarize the results of the dielectric property measurements. The table gives numerical values on the relative dielectric constant ϵ_r , the loss tangent $\tan \delta$, and the electric field tunability T . The ϵ_r and $\tan \delta$ are taken at 1 MHz and 10 GHz, while the tunability values are taken at two values of the electric fields, 2 and 4 V/ μm . In general, one can see that the dielectric constant ϵ_r and tunability T tend to decrease as the ferrite loading is increased, but the change does not scale linearly with loading. The composite loss tangent data show low values at 1 MHz and

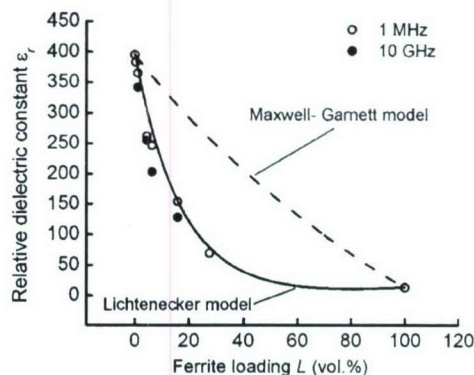


FIG. 8. Relative dielectric constant ϵ_r as a function of the ferrite loading L . The solid circles show the 10 GHz data. The open circles show the 1 MHz data. The dashed curve is a calculation based on the Maxwell-Garnett model and the solid curve is a calculation based on the Lichtenecker model for inclusions in a dielectric matrix.

TABLE II. Summary of dielectric property measurements.

Vol. % ferrite loading L	Relative dielectric constant at 1 MHz	Relative dielectric constant at 10 GHz	Dielectric loss tangent ($\tan \delta$) at 1 MHz	Dielectric loss tangent ($\tan \delta$) at 10 GHz	Tunability (%)	
					2 V/ μm	4 V/ μm
100	12.6	...	0.0390
27	69	...	0.0069	...	3.2%	6.8%
16	154	128	0.0025	0.0301	8.5%	16.0%
6	246	203	0.0019	0.0279	9.0%	19.0%
4	262	255	0.0018	0.0245	8.0%	19.0%
1	365	342	0.0009	0.0191	11.0%	24.0%
0.3	383	...	0.0006	...	12.0%	25.0%
0	395	412	0.0010	0.0235	17.0%	29.0%

high values at 10 GHz that then switch from low to high (1 MHz) and high to low (10 GHz) for the pure ferrite.

Figure 8 shows results for the relative dielectric constant ϵ_r as a function of ferrite loading. The open and solid circles show the data for 1 MHz and 10 GHz, respectively. The solid and dashed curves show computed ϵ_r vs L responses based on two commonly used dielectric response models for mixtures.²⁰ The solid curve is for the Lichtenecker model and the dashed curve is for the Maxwell-Garnett model.

There is a very rapid initial decrease in ϵ_r with L at the lower loading values and an apparent leveling off in the $L = 50$ –60 vol % range. It is clear from the theoretical curves that the Lichtenecker model fits the data nicely. This model is essentially a power law rule for inclusions in a dielectric matrix. Such a rule appears to account nicely for the initial rapid drop in ϵ_r with L . It is clear that the Maxwell-Garnett model based on spherical inclusions in a dielectric matrix does not fit the data.

Figure 9 shows results on $\tan \delta$ as a function of ferrite loading at 1 MHz and 10 GHz, as indicated. Data were obtained for L values up to 27 vol %. The inset shows the 1 MHz data for L values up to 6 vol % on an expanded scale. These data show a slow and gradual increase in $\tan \delta$ with L . The 10 GHz values are much larger, increase more rapidly, and show a bigger spread than the 1 MHz data. The results for 10 GHz are somewhat perplexing. Catalog values of $\tan \delta$ for commercial TT2-111 at 10 GHz are in the 0.0001 range.

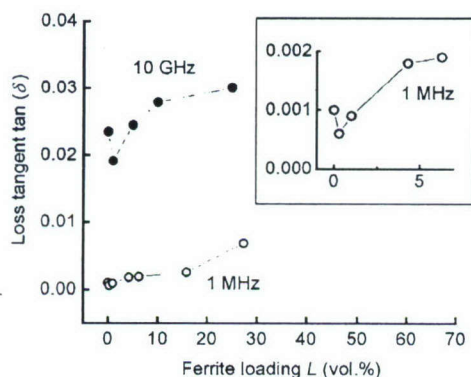


FIG. 9. Loss tangent $\tan \delta$ as a function of ferrite loading L . The solid circles are the data at 10 GHz, whereas the open circles are the data at 1 MHz. The inset shows the low L 1 MHz data on an expanded scale.

Figure 10 shows results for the normalized tunability parameter T as a function of L . The open and solid circles show the data for electric field values of 2 and 4 V/ μm , respectively. The data sets for the two fields appear to track each other and show that the electric tunability decreases, as the ferrite loading is increased. Except for the initial dip in T at low L , the trend of the response is nearly linear.

Overall, one can say that the effect of the ferrite loading on ϵ_r is consistent with well established mixing models and that the loading reduces the electric tunability of the composite. The ferrite loading has an adverse effect on the dielectric loss, especially at microwave frequencies. The large $\tan \delta$ values at 10 GHz represent a significant challenge. It is clear that significant advances in preparation methods will be needed in order to produce low dielectric loss composite materials for microwave applications.

VII. SUMMARY

The above sections have described preparation methods and measurement results on the magnetic and dielectric properties a ferrite-ferroelectric composite fabricated from a Paratek barium strontium titanate material and a Trans-Tech nickel zinc ferrite TT2-111 material. The ferrite loading levels were varied from the pure BSTO material ($L=0$) to pure TT2-111 ($L=100$ vol %). Initial susceptibility, saturation field, and coercive force data show trends consistent with the saturation induction results.

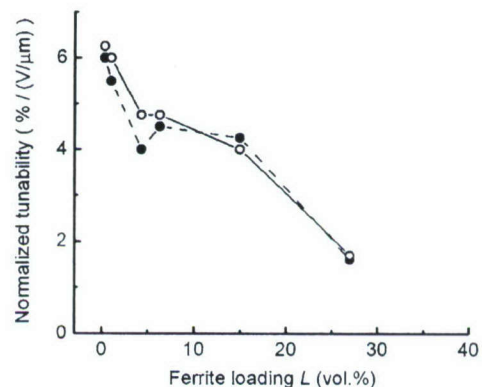


FIG. 10. Normalized tunability T as a function of ferrite loading L . The open and solid circles show the data for electric field values of 2 and 4 V/ μm , respectively.

The magnetic and electric responses at high frequency show similar effects. Any amount of BSTO added to the ferrite phase causes a severe degradation in the FMR profile and linewidth as well as the high field off-resonance effective linewidth. Similarly, any amount of ferrite added to the BSTO causes a rapid drop in the relative dielectric constant and electrical tunability. The $\tan \delta$ data indicate modest values in the 0.001–0.005 range at 1 MHz but much larger values in the 0.02–0.03 range at 10 GHz.

The XRD data and a comparison of magnetic properties for the $L=100$ vol % material and a commercial TT2-111 base line sample indicate that the processing recipe used for the composite materials did not cause any degradation in the NZF or the BSTO phase. The actual composites, on the other hand, all show a clear degradation in both the magnetic and the electric properties.

The static magnetic and dielectric constant results point to a model of unmodified spherical NZF inclusions in a non-magnetic matrix. The FMR and high field effective linewidth results show that the presence of interactions between the two phases, the shape of the NZF inclusions, and extreme dilution due to the large amount of ferroelectric material can affect the magnetic losses. The addition of even a small amount of the NZF phase causes a degradation in the dielectric loss. Further work is needed to develop fabrication processes that can preserve the desirable ferroelectric and ferrite properties of the composite while, at the same time, producing a multifunctional material with enhancements in both classes of properties.

ACKNOWLEDGMENTS

This work was initiated under a U.S. Army Research Office (USARO) short-term innovative research program, Grant No. DAAD19-99-1-0170, and followed to completion under U.S. Army Research Office, MURI Grant No. W911NF-04-1-0247, USARO-DARPA (Defense Advanced Research Projects Agency) Grant No. W911NF-06-1-0163, and Office of Naval Research (U.S.) Grant No. N00014-06-1-0889. The participants are indebted to Elwood Hoakenson and Trans-Tech, Inc., Adamstown, Maryland for a sample of

TT2-111 ferrite for static and microwave magnetic characterizations. Dr. William Wilber of CelWave Corporation, Marlboro, New Jersey, Dr. James Baker-Jarvis and Dr. Pavel Kabos of the National Institute of Standards and Technology, Boulder, Colorado, and Professor Gopalan Srinivasan of Oakland University, Rochester, Michigan are acknowledged for helpful discussions on ferrite-ferroelectric composite materials. Michael Varney is acknowledged for his assistance with the static magnetic measurements. Dr. Sandeep Kohli is acknowledged for his assistance with the x-ray diffraction measurements.

¹R. Valenzuela, *Magnetic Ceramics* (Cambridge University Press, Cambridge, 1994).

²L. C. Sengupta and S. Sengupta, *IEEE Trans. Ultrason. Ferroelectr. Freq. Control* **44**, 793 (1997).

³F. A. Miranda, G. Subramanyam, F. W. Van Keuls, R. R. Romanofsky, J. D. Warner, and C. H. Mueller, *IEEE Trans. Microwave Theory Tech.* **48**, 1181 (2000).

⁴X. Qi, J. Zhou, Z. Yue, Z. Gui, and L. Li, *J. Magn. Magn. Mater.* **269**, 352 (2004).

⁵D. J. Bergman, *Phys. Rep., Phys. Lett.* **43**, 377 (1978).

⁶D. J. Bergman, *Phys. Rev. B* **19**, 2359 (1979).

⁷D. J. Bergman, *Phys. Rev. B* **23**, 3058 (1981).

⁸D. J. Bergman and D. Stroud, *Solid State Phys.* **46**, 147 (1992).

⁹D. J. Bergman, O. Levy, and D. Stroud, *Phys. Rev. B* **49**, 129 (1994).

¹⁰D. M. Grannan, J. C. Garland, and D. B. Tanner, *Phys. Rev. Lett.* **46**, 375 (1981).

¹¹D. E. Aspnes, *Phys. Rev. Lett.* **48**, 1629 (1982).

¹²C. A. Grimes and D. M. Grimes, *J. Appl. Phys.* **69**, 6168 (1991).

¹³B. Abeles, H. L. Pinch, and J. I. Gittleman, *Phys. Rev. Lett.* **35**, 247 (1975).

¹⁴T. Kanai, S. Ohkoshi, A. Nakajima, T. Watanabe, and K. Hashimoto, *Adv. Mater. (Weinheim, Ger.)* **13**, 487 (2001).

¹⁵J. V. Mantese, A. L. Micheli, D. F. Dungan, R. G. Geyer, J. Baker-Jarvis, and J. Grosvenor, *J. Appl. Phys.* **79**, 1655 (1996).

¹⁶M. Sparks, *Ferromagnetic Relaxation Theory* (McGraw-Hill, New York, 1964).

¹⁷C. E. Patton, in *Magnetic Oxides*, edited by D. J. Craik (Wiley, London, 1975), pp. 575–645.

¹⁸J. R. Truedson, P. Kabos, K. D. McKinstry, and C. E. Patton, *J. Appl. Phys.* **76**, 432 (1994).

¹⁹R. G. Geyer, J. Krupka, L. Sengupta, and S. Sengupta, *Proceedings of the Tenth IEEE International Symposium on Applications of Ferroelectrics*, 1996 (unpublished), Catalog No. 96CH35948, p. 851.

²⁰A. Sivvola, *Electromagnetic Mixing Formulas and Applications* (The Institution of Engineers, London, UK, 1999).

Ferromagnetic resonance saturation and second order Suhl spin wave instability processes in thin Permalloy films

Heidi M. Olson,^{a)} Pavol Krivosik,^{b)} Kumar Srinivasan,^{c)} and Carl E. Patton
Department of Physics, Colorado State University, Fort Collins, Colorado 80523

(Received 9 February 2007; accepted 6 June 2007; published online 18 July 2007)

High power ferromagnetic resonance (FMR) loss versus static field H profiles and the corresponding spin wave instability threshold microwave field amplitude h_{crit} vs H butterfly curves were measured for in-plane magnetized thin Permalloy films of thicknesses 35, 57, 74, 104, and 123 nm at a nominal pumping frequency of 9.11 GHz. Cavity loading and calibration issues that proved to be problematic in past attempts to obtain accurate resonance saturation data over the full FMR profile in ferrites and metal films were resolved through a careful decoupling of the pump field and a full cavity response calibration. The FMR profiles show a drop in the loss peak, a shift in the peak to lower field, a broadening, and the development of a foldover-like asymmetry as the power is increased. The butterfly curves show a minimum h_{crit} at the low power FMR field and a smooth rounded increase on either side, except for a small kink on the low field side associated with the shift and asymmetry development. Apart from the kink, the second order Suhl spin wave instability theory, suitably modified for thin films, provided good fits to the butterfly curve data through the use of a single spin wave linewidth ΔH_k value for each data set. The ΔH_k values ranged from 16 to 35 Oe, with the implied critical mode in-plane wave vectors always directed parallel to the static field. These spin wave linewidths translate into Gilbert damping parameter α_k values in the 0.002–0.005 range, the same order as expected for intrinsic magnon-electron scattering losses in metal ferromagnets. These α_k values are about a factor of 2 smaller than those implied by the low power FMR linewidths. The FMR in-plane precession cone angles at threshold were on the order of 3° – 6° . © 2007 American Institute of Physics. [DOI: 10.1063/1.2756481]

I. INTRODUCTION

Dobin and Victora¹ have recently demonstrated a direct connection between the nonlinear dynamics in large angle magnetization switching in thin films and parametric Suhl spin wave instability processes.² The additional losses associated with these nonlinear processes can, in principle, have a dramatic effect on magnetization switching in recording applications. The extra losses, for example, can serve to reduce switching speeds in conventional heads and media applications. At the same time, the nonlinear interactions can also promote magnetization reversal. This has been recently demonstrated for a variety of current driven nanocontact and nanopillar spin torque devices.^{3,4}

One clear way to examine the basic nonlinear interactions that are relevant to large angle switching in thin films is to study the Suhl second order spin wave instability processes that occur at ferromagnetic resonance (FMR) for high microwave power levels. While high power FMR experiments do not extend to angles as large as those that occur in switching, they provide a measure of the precession angles at which nonlinear effects come into play. In Permalloy films, for example, the onset of Suhl spin wave instability (SWI) processes and resonance saturation effects generally occur at precession angles in the 3° – 6° range.

While there has been extensive work on Suhl processes in ferrites, high power FMR work on metal films is limited to a few studies in the 1960s. High power resonance saturation for in-plane magnetized Permalloy films was first observed by Comly *et al.*⁵ Follow-up work by Berteaud and Pascard^{6,7} revealed resonance saturation at high power as well as evidence for the so-called subsidiary absorption at lower fields associated with Suhl first order processes. All of these early data were somewhat limited in focus and there were no quantitative connections to the Suhl theory.

Recent work by An *et al.*⁸ extended measurements of subsidiary absorption to include full data on the Suhl SWI threshold microwave field amplitude versus static field for in-plane magnetized films. These authors also provided a full analysis of the data based on the Suhl first order theory, suitably modified for the thin film geometry. As a result of cavity loading and calibration issues, Ref. 8 did not include any quantitative work on resonance saturation or Suhl second order processes.

This work is concerned specifically with the quantitative study of the high power resonance saturation response for thin Permalloy films. The cavity loading and calibration issues from Ref. 8 have been resolved. The sections below give a full description of the experimental methods, present comprehensive data on resonance saturation, and provide a theoretical analysis of the relevant Suhl processes over the full FMR profile. The main results are (1) FMR profiles as a function of input power, (2) a determination of the SWI threshold microwave field amplitude (h_{crit}) as a function of

^{a)}Electronic mail: heidio@lamar.colostate.edu

^{b)}On leave from the Department of Electromagnetic Field Theory, Faculty of Electrical Engineering and Information Technology, Bratislava, Slovakia.

^{c)}Present address: Spintronics, Media and Interface Division, Data Storage Institute, Singapore.

TABLE I. Summary of low power 9.11 GHz ferromagnetic resonance (FMR) measurements and derived parameters.

Film thickness d (nm)	FMR field H_{FMR} (Oe)		Effective saturation induction $4\pi M_{s\text{-eff}}$ (G)	Gyromagnetic constant $ \gamma /2\pi$ (MHz/Oe)	IPSF half power FMR linewidth ΔH_{FMR} (Oe)	IPSF equivalent Gilbert damping parameter α_{FMR}
	In-plane static field (IPSF)	Perpendicular-to- plane static field (PPSF)				
35	806	13 878	10 820	2.976	44	0.0072
57	838	13 591	10 510	2.954	41	0.0066
74	782	14 275	11 210	2.974	37	0.0060
104	830	14 494	11 320	2.869	59	0.0093
123	850	13 560	10 460	2.938	56	0.0090

the static magnetic field (H) over the entire FMR profile, and (3) an analysis of the h_{crit} vs H data in terms of the second order Suhl theory. Such h_{crit} vs H profiles are termed butterfly curves. Item (3) yields the critical modes and spin wave damping parameters applicable to resonance saturation. These results represent the first comprehensive measurements and analyses of Suhl processes at FMR for metal films. They also represent the first work on spin wave instability over the full FMR profile and the measurement of full butterfly curves for resonance saturation in metal films.

Section II gives an overview of the thin film materials, the low power microwave characterizations, the FMR system, and the measurement procedures. Section III introduces the high and low power FMR responses and gives details on the decoupling of the cavity and general calibration issues. Section IV presents the experimental results on resonance saturation. This includes representative calibrated data on microwave loss as a function of the microwave field amplitude, Suhl threshold determinations, and butterfly curves. Section V (1) gives a brief review of the uniform mode and spin wave theory modified for thin films, (2) provides a conceptual introduction to second order Suhl instability theory for thin films, and (3) develops the working h_{crit} equations and operational procedures for the evaluation of butterfly curves. Section VI considers the theoretical butterfly curve fits to the data, along with a discussion of the spin wave linewidths, damping parameters, and maximum precession angles at FMR that come from the analysis. Section VII provides a summary and conclusion.

II. THIN FILM MATERIALS AND MEASUREMENT PROCEDURES

A. Thin film materials and characterization

Permalloy films with thicknesses (d) of 35–123 nm were thermally evaporated on glass substrates in a nominal vacuum of 10^{-6} Torr and in the presence of an in-plane static field. The films evidenced the usual field induced uniaxial anisotropy with effective anisotropy fields in the range of 5 Oe or so. This anisotropy plays no critical role in the response of interest at fields around 800 Oe. Two of the films, with d values of 35 and 104 nm, were deposited on substrates held at ambient room temperature. Three films, with thicknesses of 57, 74, and 123 nm, were deposited on heated substrates at about 300 °C. All films were 5 mm in diameter and had nominal compositions of 82 at. % Ni and 18 at. %

Fe. The films were all prepared by S. Konishi, Kyushu University, Fukuoka, Japan in the 1970s. In spite of the age of these films, the FMR profiles were all clean and reasonably narrow.

The basic film properties were determined by standard low power FMR measurements for both in-plane static field (IPSF) and perpendicular-to-plane static field (PPSF) configurations. Measurement details are given in the next section. Table I lists key results. The in-plane and out-of-plane FMR field values (H_{FMR}) were used to determine the effective saturation induction $4\pi M_{s\text{-eff}}$ and the gyromagnetic constant $|\gamma|/2\pi$ from the standard Kittel formula with the small uniaxial anisotropy ignored. The table lists the measured FMR fields for convenient transfer to the computed $4\pi M_{s\text{-eff}}$ and $|\gamma|/2\pi$ parameters shown. The listed $4\pi M_{s\text{-eff}}$ and $|\gamma|/2\pi$ values match reasonably well to literature values for the saturation induction and the gyromagnetic constant for Permalloy.

The last two columns show the measured half power FMR linewidths (ΔH_{FMR}) and the corresponding Gilbert damping parameters (α_{FMR}) for the measured films. These damping values were obtained from the standard connection derived from the Gilbert damped equation of motion, $\alpha_{\text{FMR}} = |\gamma| \Delta H_{\text{FMR}} / 2\omega_p$, where $\omega_p/2\pi$ corresponds to the cavity frequency of 9.11 GHz. The reasonably small linewidths and low α_{FMR} values are indicative of good quality low loss films. The base parameters in Table I will be important for the analyses in later sections. The quantities listed, as well as parameters and equations to follow, are in Gaussian cgs units. Measurement details follow in the next section. Experimental results will focus on the 104 nm film.

B. FMR system and measurement procedures

All measurements were made with an X-band pulsed microwave reflection cavity spectrometer system similar to that described in Ref. 9. The empty TE102 cavity had a nominal center frequency $f = \omega_p/2\pi$ of 9.11 GHz, a power reflection coefficient ρ_0 of -30 dB at cavity resonance, and a loaded quality factor Q_L of 2600. The cavity was undercoupled and had a nominal empty cavity calibration coefficient $C_e = h^2/P$ of 3.54 Oe²/W, where h is the amplitude of the microwave field for sample placement at the cavity end wall and P is the peak input power to the cavity. The setups were such that the linearly polarized microwave field was always in the plane of the film.

The high power capability was provided by a low duty cycle 8–18 GHz traveling wave tube amplifier with a peak power capability of 2 kW. All high power data were obtained in the IPSF configuration, with 4 μ s wide linearly polarized input pulses at a 40 Hz repetition rate, peak powers up to 1 kW, and with the film samples placed on the cavity end wall. The duty cycle was set low enough to avoid sample heating effects. All of these measurements were made with 12 in. diam magnet pole pieces, a 5 in. magnet gap, and a corresponding high homogeneity static field at the sample position. The field change from the sample position to the position of the Hall probe used for the field measurement, about 1 cm away, was less than 0.2 Oe.

Two types of microwave measurements were made: (I) uncalibrated FMR absorption profiles of cavity voltage reflection coefficient ρ versus static magnetic field H for a range of peak power P values and (II) uncalibrated (II-u) and calibrated (II-c) threshold curve profiles of ρ vs P for a range of H values over the full FMR profile. The term “uncalibrated” means that the data were obtained under cavity loading conditions for which the connection between P and h was not fixed. This is generally the case when the static and microwave fields are mutually perpendicular and the FMR coupling is strong. Through a reduction in the coupling angle θ between these fields, the coupling can be reduced to the point where one can define $C=h^2/P$ for the sample loaded cavity and transition to a “calibrated” measurement. As a rule of thumb, one can calibrate the microwave field-power response as long as (1) the change in the cavity Q_L over the resonance line is less than 20% and (2) one performs the calibration as a function of ρ .

The type I ρ vs H measurements were used for the low power FMR position and linewidth determinations for both the IPSF and the PPSF configurations. The microwave field coupling angle θ was held at 90° in all cases. Even though the use of this maximum coupling means that the ρ vs H profiles are uncalibrated, the half power linewidths extracted from the profiles are still accurate. This was confirmed from actual response simulations based on the loaded cavity response. The low power IPSF FMR position and linewidth measurements were made at $P=0.44$ W and the same pulse width and repetition rate as given above. The corresponding low power PPSF measurements were made with $P=0.44$ W and 10 μ s wide input pulses. For the PPSF measurements, fields in excess of 10 kOe were needed. It was necessary to place the samples on the sidewall of the cavity and fit the electromagnet with tapered pole pieces. The field change in this case from the Hall probe to the sample position was on the order of 0.75 Oe. The fields shown in Table I for both IPSF and PPSF FMRs, as well as the values given in the results below, show the corrected field values at the sample position, with an estimated accuracy of an oersted.

Types I and II measurements were both used for the IPSF configuration high power work. First, uncalibrated type I ρ vs H profiles as a function of power were used to survey the changes in the FMR absorption curve response with P . These results will be considered in Sec. III A. Second, type II-u (uncalibrated) ρ vs P threshold curve data for H values close to resonance and different coupling angles were used to

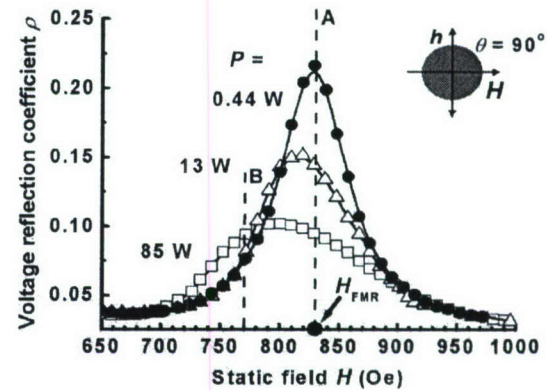


FIG. 1. Voltage reflection coefficient ρ vs the static external magnetic field H for the 104 nm thin film, the in-plane static field configuration, and a microwave frequency of 9.11 GHz. The symbols show data for different peak input power P values, as indicated. The dashed lines show cuts at 830 Oe, the ferromagnetic resonance field H_{FMR} line cut A, and B at a lower field value of 770 Oe. The H field and the linearly polarized microwave field h were in plane and mutually perpendicular at $\theta=90^\circ$, as shown in the inset.

determine the maximum coupling for a calibrated response. These coupling considerations and related calibration issues are given in Sec. III B. Finally, type II-c (calibrated) ρ vs P data were obtained for a full range of fields over the FMR profile for a small enough coupling angle, typically at $\theta \approx 60^\circ$, to ensure a calibrated connection between P and h . These data, in turn, were used to obtain the threshold h_{crit} values as a function of H , the so-called butterfly curves introduced in Sec. I. As already noted, all of these data were obtained with the film sample on the end wall of the cavity with the microwave and static fields both in plane.

Sections III and IV are intended to provide a step-by-step development of the overall high power analysis procedure. This starts (Sec. III A) with the general effect of high power on the ρ vs H FMR profiles. This is followed (Sec. III B) with an analysis of ρ vs P data for a fixed field cut at the FMR peak to establish maximum coupling limits for a calibrated response. Appendix A then gives technical details on the procedure to obtain the cavity calibration parameter $C=h^2/P$. This parameter has meaning only in the low coupling limit. Section IV then uses data on ρ vs h to determine threshold field values (Sec. IV A) and develop butterfly curves of h_{crit} vs H (Sec. IV B).

III. QUALITATIVE FMR RESPONSE PROFILES AND MICROWAVE FIELD CALIBRATION

A. FMR response as a function of power

Figure 1 shows example uncalibrated FMR response profiles for the 104 nm film. The graph shows data on the cavity reflection coefficient ρ versus static field H for peak input power levels to the cavity (P) of 0.44, 13, and 85 W, as indicated. The static and microwave fields were in plane and mutually perpendicular at $\theta=90^\circ$, as shown in the diagram inset. The vertical dashed line at the FMR field, labeled A, and the off resonance line, labeled B, correspond to H values of 830 and 770 Oe, respectively. These lines show ρ vs P cuts at fixed H that will be useful for the discussion in Sec. IV. It is important to emphasize that these FMR curves are

obtained at full coupling ($\theta=90^\circ$) and there is no one-to-one correspondence between P and the microwave field amplitude h over a given profile. In other words, constant P does not mean fixed h .

As noted, the low power FMR peak in Fig. 1 is at 830 Oe and the half power linewidth is about 59 Oe. The qualitative changes in the profiles as P is increased provide an indication of the overall nonlinear response. The profile for $P=13$ W is broader, lower in amplitude, and slightly asymmetric, relative to the low power profile. The asymmetry amounts to a shift of the profile to lower fields and a development of a low field shoulder. This trend continues to an even greater extent for the $P=85$ W profile.

The drop in amplitude and broadening of the FMR peak with increasing power is the basic resonance saturation (RS) response associated with second order Suhl SWI processes. It is important to keep in mind that such processes occur for power levels well below those for which saturation effects are expected from classical theory. It is also important to note that the change in ρ with increasing power at a fixed field is not a continuous effect. Calibrated data on ρ vs h , to be considered shortly, will show that the change in reflection coefficient occurs more or less abruptly at some threshold h value. It is this change that defines the threshold microwave field amplitude h_{crit} .

The shift to low field and the development of the low field shoulder with increasing power is the manifestation of a foldover effect for metal films. The asymmetry development also leads to a kink in the butterfly curve, h_{crit} vs H profile, at a field somewhat below the minimum H point. The foldover shifts the high field response to a lower field and the nonlinear broadening increases the high field response to higher fields. The combination of these produces high field responses that appear to be independent of power with no measurable threshold. Preliminary work suggests that the foldover is due to two magnon scattering interactions.¹¹ Further work on two magnon effects in RS processes will be published separately.

B. Cavity calibration

As noted, accurate cavity calibration is critical to precise h_{crit} determinations. Before calibrations can be made, however, it is necessary to determine the maximum allowable FMR coupling for perturbation theory to be applicable. Once this limit is set, the coupling can be reduced to acceptable levels and the actual calibration coefficient C as a function of ρ can be obtained.

The upper limit on the FMR coupling for a valid calibrated response was determined from data on ρ vs P for different coupling angles (θ) between the microwave field and the static magnetic field. These data were obtained for a static field at the low power FMR peak. For comparison purposes the ρ data were converted to a reduced loss parameter L_R according to

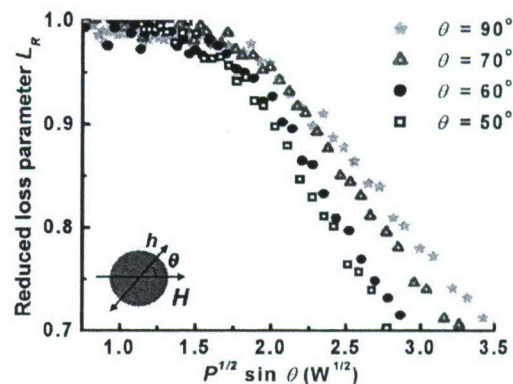


FIG. 2. Reduced loss parameter L_R vs the effective pumping factor $\sqrt{P} \sin \theta$ for the 104 nm thin film, where P is the peak input power to the cavity and θ is the coupling angle between the static field H and the microwave field h , as shown in the inset. Both fields are in plane. The data are for $H=830$ Oe and a pumping frequency of 9.11 GHz.

$$L_R = \frac{(\rho_P - \rho_{\text{ref}})(1 - \rho_0)}{(\rho_0 - \rho_{\text{ref}})(1 - \rho_P)} \quad (1)$$

Here, ρ_P is the measured ρ value for the input peak power P value of interest and ρ_0 is the ρ value in the low power limit, with both obtained at the FMR field, while ρ_{ref} is the reference ρ value with the static field set far from the FMR field.

The introduction of a reduced loss parameter L_R for the data comparison for different coupling angles deserves brief comment. Recall that at or close to FMR, the voltage reflection coefficient ρ is comprised of two parts, the empty cavity part ρ_0 and the component related to the FMR loss. As demonstrated in Fig. 1, the component related to FMR decreases as the power is increased. A decrease in coupling has a similar effect. As a result, one cannot use ρ as a basis of comparison for different coupling angles.

The standard microwave perturbation theory analysis for a weakly coupled cavity indicates that L_R should correspond to the ratio of the high and low power negative imaginary components of the microwave susceptibility. In other words, in the small coupling limit for which perturbation theory is valid, plots of L_R versus the effective pumping field should all show the same nonlinear response. Recall that the microwave field amplitude h at the sample position scales with the square root of P and that only the component of \mathbf{h} that is transverse to the static field drives the FMR response. For a given angle θ between \mathbf{H} and \mathbf{h} , the effective pumping field amplitude will scale with $\sqrt{P} \sin \theta$. A determination of the maximum allowable coupling angle in this step of the calibration procedure may be obtained from plots of L_R vs $\sqrt{P} \sin \theta$.

Figure 2 shows representative data on L_R vs $\sqrt{P} \sin \theta$ for the 104 nm film and a range of coupling angles that demonstrate the loading effects described above. These specific data are for $H=830$ Oe, at the FMR line cut A in Fig. 1. Data are shown for θ values of 90° , 70° , 60° , and 50° , as indicated, and input powers from 0 to 49 W. For the two largest θ values, 70° and 90° , excessive cavity loading gives a L_R vs $\sqrt{P} \sin \theta$ response that depends on the coupling and shows a larger distortion for higher powers. For the two smaller θ values, 50° and 60° , the L_R vs $\sqrt{P} \sin \theta$ response profiles are

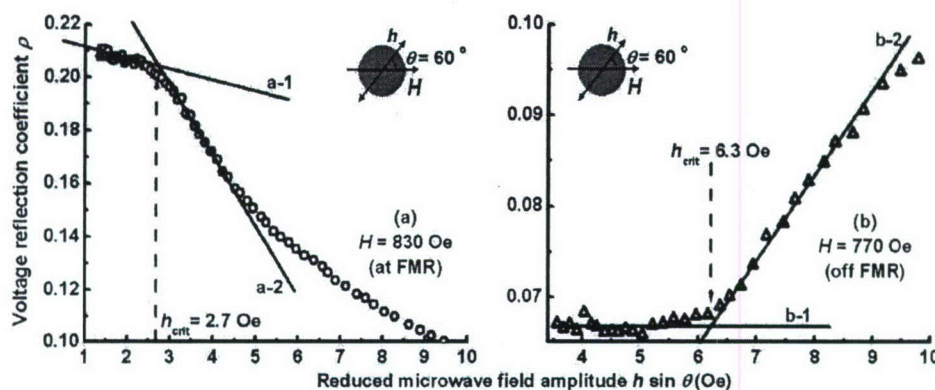


FIG. 3. Voltage reflection coefficient ρ vs the reduced microwave field amplitude $h \sin \theta$ for the 104 nm thin film at 9.11 GHz. The insets show the coupling geometry, with the in-plane static field H and the in-plane linearly polarized microwave field h at $\theta = 60^\circ$ for both sets of data. Graph (a) shows a representative threshold response for $H = 830$ Oe, at the low power ferromagnetic resonance (FMR) peak position. Graph (b) shows the corresponding response for $H = 770$ Oe, on the low field side of the low power FMR profile. The straight lines are guides to the eyes. The intersections marked by the vertical dashed lines give estimations of the spin wave instability threshold microwave field amplitude h_{crit} for the two different cases illustrated here.

identical within the error of the data. This is an indication that coupling angles at or below 60° or so are sufficient to put the cavity response in the regime where (1) perturbation theory is applicable and (2) a proper calibration between P and h is possible. Calibrated data on L_R vs $h \sin \theta$ in this regime give Suhl saturation response profiles that are independent of the coupling angle and give an accurate and reliable determination of the h_{crit} threshold at a given static field. It is also important to note that the change in the cavity Q_L over the full range of the data in Fig. 2 for the two *smallest* θ values is less than 20%. This is the order of change in coupling that sets an upper limit on the applicability of perturbation theory and a valid microwave field calibration.

Turn now to the determination of the calibration coefficient $C = h^2/P$ that connects the measured power P to the microwave field amplitude h . The traditional approach is to bias the cavity at a field far from ferromagnetic resonance and use the standard recipe from Ref. 11 for a determination of the various cavity parameters. This approach is inadequate for resonance saturation measurements. The changes in the cavity frequency, the Q_L parameters, and the calibration change substantially as one sweeps the static field across the full FMR profile. These changes make it impossible to obtain accurate h_{crit} values based on a single high field cavity reference measurement.

In the process to establish a workable calibration procedure, it was discovered that even though C changes as one moves across the FMR profile, this sought after calibration parameter is a unique function of the cavity reflection coefficient ρ . This is found to apply to all of the data for different samples, different coupling angles, and different static fields. The details of the procedure to determine the universal $C(\rho)$ calibration function are given in Appendix A. This calibration recipe represents a major improvement over previous work. With the exception of Ref. 9, most past FMR saturation measurements have been made for maximum coupling, that is, with perpendicular static and microwave fields. From Fig. 2, one can see that a large coupling can lead to a distortion in the threshold curve. This can result in an overestimation of the onset h value by as much as 10%. The calibration performed for this work, given in Fig. 5 (Appendix A),

shows that the nominal off resonance C value of $3.54 \text{ Oe}^2/\text{W}$ is 50% higher than the value at FMR. If this value is used for the h vs P calibration, the apparent microwave field values are about 25% too high. The combination of these considerations gives field calibration errors at FMR for the old off resonance approach in excess of 35%.

IV. HIGH POWER FERROMAGNETIC RESONANCE RESPONSE

As already noted, the change in the FMR response as the input microwave power level is increased is a threshold effect and not a gradual change. The threshold microwave field amplitude, previously defined as h_{crit} , is the subject of this section. Section IV A is concerned with the calibrated ρ vs $h \sin \theta$ responses obtained from the ρ vs P measurements at fixed static field, the change in these responses as one moves across the FMR profile, and the extraction of h_{crit} values from these data. Section IV B focuses on the butterfly curve profiles of h_{crit} vs H .

A. High power threshold response

Recall the two vertical A and B line cuts through the uncalibrated FMR profiles in Fig. 1. The A cut, at the low power FMR peak position, shows that the reflection coefficient decreases as the power is increased. The B cut, positioned well off the FMR peak, shows that ρ increases with an increase of power. Properly calibrated data based on the procedures given in Sec. III yield quantitative ρ vs $h \sin \theta$ plots that show the threshold effect.

Graphs (a) and (b) in Fig. 3 show calibrated ρ vs $h \sin \theta$ responses that correspond to the A and B field cuts at 830 and 770 Oe from Fig. 1. The insets show the H - h - θ coupling configurations. Recall that only the transverse component of h relative to the static field direction is effective in driving the response. The data are for the same 104 nm film and $\theta = 60^\circ$, as before. The straight lines provide guides to the eyes for the estimation of h_{crit} values from the data.

Both graphs demonstrate the threshold nature of the non-linear response. For the FMR situation in (a), line a-1 shows that ρ is large and a weakly decreasing function of $h \sin \theta$ for low power and small h , while line a-2 shows a more rapid decrease at high power and large h . The intersection of the two lines defines the threshold h_{crit} . Off FMR, as in (b), the situation is different. Now, ρ is relatively small and essentially constant below threshold and then shows a rapid increase above threshold. In parallel with graph (a), lines b-1 and b-2 show the low and high power trends and the intersection that marks the h_{crit} . Note also that the threshold response is not particularly sharp in either case.

Figure 3 shows three things. First, both data sets show a threshold effect. The corresponding h_{crit} values can be taken to define a SWI threshold. The physical basis for the instability was established by Suhl in 1957.² The idea is that the driven uniform mode couples energy into parametrically pumped half frequency spin waves at a power dependent rate G_k . At the point in power at which G_k exceeds the relaxation rate of the spin waves, taken as η_k , the occupation numbers of the spin waves increase above thermal levels and one sees an abrupt change in the loss. A more detailed statement of the Suhl theory will be given in Sec. V.

Second, one sees quantitatively different threshold responses on and off resonance. At the low power FMR field position, as in (a), the change in the rate of decrease in ρ with increasing $h \approx h_{\text{crit}}$ is due to an initial lockup in the FMR amplitude and a decrease in the effective microwave susceptibility. Off resonance, as in (b), the loss starts out small because the static field position is on the tail of the FMR response. As h exceeds h_{crit} , the parametric generation of spin waves leads to additional loss and ρ increases.

The third point to note is that the threshold transitions are fairly gradual and do not show the sharp threshold effects of the sort expected from the original nonlinear Suhl theory or in defect-free single crystal ferrites, for example. Suhl has also shown, however,¹² that two magnon scattering interactions can lead to this type of rounded response. As noted above, Krivosik¹⁰ has extended the two magnon analysis of Suhl in the context of metallic thin films. Reference 10 shows that such processes can give a rounded rather than a sharp transition at threshold as well as the asymmetry in the high power FMR profile of the sort shown in Fig. 1.

B. Resonance saturation butterfly curves

Figure 4 shows a representative resonance saturation butterfly curve for the 104 nm thin film. The threshold fields were obtained from data similar to those in Fig. 3. At the high H limit of the data shown, the threshold responses were extremely weak or nonexistent. This is connected with the power independent high field FMR tail responses in Fig. 1. No reliable h_{crit} determinations were possible for static fields above about 880 Oe or so. The vertical line at $H_X = 810$ Oe marks the threshold crossover point in field between the two types of responses shown in Fig. 3. The solid circle indicates the FMR field point from Table I. The solid curve shows a fit to the data based on the modified Suhl theory to be considered in Secs. V and VI.

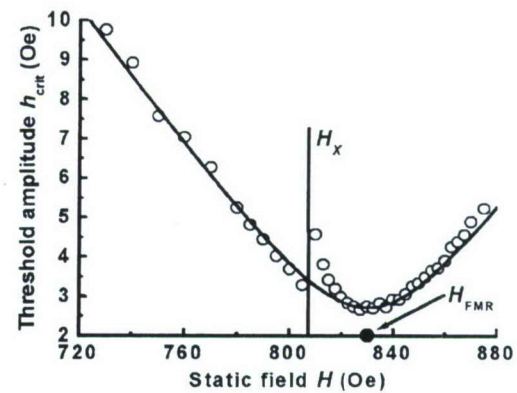


FIG. 4. Resonance saturation butterfly curve of the spin wave instability threshold microwave field amplitude h_{crit} vs static magnetic field H for the 104 nm thin film. The pumping frequency was 9.11 GHz. The coupling geometry is the same as in Fig. 3. The solid circle denotes the FMR field position. The vertical line at H_X marks the jump in the h_{crit} data. The solid curve shows a fit of the thin film second order spin wave instability theory to the data.

The data in Fig. 4 show two main features. First, the overall h_{crit} vs H profile shows a minimum threshold at the FMR field and a symmetric increase in the threshold as one moves to lower or higher fields. Second, there is a departure from the overall smooth symmetric profile for fields close to the H_X crossover point and a distinct jump in the h_{crit} vs H response at H_X .

The overall shape of the butterfly curve profile is tied closely to the low power FMR response. At the FMR peak where the FMR precession angle is large, the coupling to parametric spin waves is strong, and h_{crit} is at a minimum. As the static field is shifted above or below FMR, the precession angle decreases, the coupling also decreases, and a higher microwave field is needed to reach the instability threshold. Qualitatively, this means that the h_{crit} vs H profile is an inverted rendition of the low power FMR absorption profile. This connection is only qualitative because the actual coupling depends on the uniform mode response in a complicated way. The analytical formulas for the response are summarized below and in the Appendix. The good theoretical fit to the data shows that the rigorous analysis gives quantitative agreement.

As noted above, $H = H_X$ marks the crossover point in field between the two types of responses shown in Fig. 3. The deviation in the h_{crit} data from the smooth solid curve and the jump are related to the foldover effect in Fig. 1. Consider the situation for fields below H_X . In this regime, the shift of the broadened FMR profile to lower fields as the power is increased will correspond to a decrease in h_{crit} . For $H < H_X$, a higher ρ at a given field point in Fig. 1, compared to what one would have without a shift, corresponds to a lower threshold. The data in Fig. 4 do show a small drop in the threshold relative to the solid curve. Conversely, the higher ρ for $H_X < H < H_{\text{FMR}}$ causes an increase in threshold. For this field range, the data in Fig. 4 show a relatively large effect. The drop in h_{crit} for $H < H_X$ and the increase for $H > H_X$ then give the jump shown in the data.

The results given above for the 104 nm thin film are typical of the results for the other samples. Good theoretical

fits were obtained and all samples showed the same distortions and jump around the H_X point as just discussed.

V. SECOND ORDER SUHL SPIN WAVE INSTABILITY THEORY SUMMARIZED

Reference 8 outlines a simplified version of the Suhl spin wave instability theory for RS and subsidiary absorption (SA) processes in thin films but gives the working equations for the first order SA processes only. This section reviews the foundations of the theory, gives working equations that lead to the instability threshold microwave field amplitude h_{crit} and the corresponding critical modes for second order RS processes, and outlines an operational procedure for the analysis of RS butterfly curve data.

A. Uniform mode and spin wave basics

The starting point for the analysis is the magnetic torque equation of motion for the dynamic magnetization $\mathbf{m}(\mathbf{r}, t)$,

$$\frac{d\mathbf{m}(\mathbf{r}, t)}{dt} = -|\gamma|\mathbf{M}(\mathbf{r}, t) \times \mathbf{H}_{\text{eff}}(\mathbf{r}, t). \quad (2)$$

Here, $\mathbf{M}(\mathbf{r}, t)$ represents the total magnetization and $\mathbf{H}_{\text{eff}}(\mathbf{r}, t)$ is the total effective field. The magnetization is further expanded as

$$\mathbf{M}(\mathbf{r}, t) = M_s \hat{\mathbf{z}} + \mathbf{m}_0(t) + \sum_{\mathbf{k} \neq 0} \mathbf{m}_{\mathbf{k}}(t) e^{-i(\mathbf{k} \cdot \mathbf{r} - \omega_{\mathbf{k}} t)}, \quad (3)$$

where the M_s is the saturation magnetization, $\mathbf{m}_0(t)$ is the uniform mode part of the steady state dynamic magnetization response, and the $\mathbf{m}_{\mathbf{k}}(t) e^{-i(\mathbf{k} \cdot \mathbf{r} - \omega_{\mathbf{k}} t)}$ terms denote quasi-plane-wave spin wave excitations with an in-plane wave vector \mathbf{k} and frequency $\omega_{\mathbf{k}}$. The total field, $\mathbf{H}_{\text{eff}}(\mathbf{r}, t)$, is comprised of the external static magnetic field $\mathbf{H} = H \hat{\mathbf{z}}$, a uniform, transverse, in-plane, and linearly polarized microwave pumping field $\mathbf{h}_0(t) = h \cos(\omega_p t) \hat{\mathbf{x}}$, and the applicable uniform demagnetizing field, spatially varying dipole field, and effective exchange field.

For the thin film problem at hand, the $\hat{\mathbf{z}}$ -directed static field is taken to be sufficient to saturate the film. The microwave field drives the uniform mode $\mathbf{m}_0(t)$ response. All of the $\mathbf{m}_{\mathbf{k}}(t)$ spin wave amplitude factors are taken to be at thermal levels as long as one is below the Suhl instability threshold. The theory gives expressions for the threshold microwave field amplitude h_c at which some particular $\mathbf{m}_{\mathbf{k}}(t)$ shows exponential growth. The \mathbf{k} mode with the lowest threshold h_{crit} value is taken as the critical mode corresponding to some \mathbf{k}_{crit} . In principle, the corresponding threshold microwave field amplitude h_{crit} then corresponds to the SWI threshold.

The uniform mode response plays a key role. The standard linearized torque equation analysis in the small signal and low damping limit, with a uniform drive and damping included, yields specific expressions for $\mathbf{m}_0(t)$. The peak response is at the well known Kittel FMR frequency, $\omega_0(H) = |\gamma| \sqrt{H(H + 4\pi M_s)}$. The condition $\omega_0(H) = \omega_p$ then defines the FMR field H_{FMR} . This is the field point indicated in Figs.

1 and 4. The critical low power experimental parameters are this FMR field and the half power linewidth ΔH_{FMR} , as introduced in Sec. II.

It is the $\mathbf{m}_0(t)$ response that drives the second order spin wave instability in the Suhl theory. The formulation is usually done in terms of a reduced transverse $\hat{\mathbf{x}}\text{-}\hat{\mathbf{y}}$ linear response function, written here as $a_0(t) = [m_{0x}(t) + im_{0y}(t)]/M_s$. From Eq. (2) with damping included, the working equation for $a_0(t)$ may be written as

$$a_0(t) = \frac{|\gamma|h}{2} (q_L e^{+i\omega_p t} + q_A e^{-i\omega_p t}), \quad (4)$$

where the q_L and q_A amplitudes denote the Larmor and the anti-Larmor contributions to the response and are

$$q_L = \frac{\omega_H + \omega_M + \omega_p}{\omega_0^2 - \omega_p^2 + i2\omega_p \eta_0} \quad (5)$$

and

$$q_A = \frac{\omega_H + \omega_M - \omega_p}{\omega_0^2 - \omega_p^2 - i2\omega_p \eta_0}. \quad (6)$$

The frequency parameters ω_H and ω_M , defined as $|\gamma|H$ and $|\gamma|4\pi M_s$, respectively, express H and $4\pi M_s$ in frequency units. The relaxation rate parameter η_0 is given by

$$\eta_0 = \frac{|\gamma|\Delta H_{\text{FMR}}}{2} \varepsilon, \quad (7)$$

where $|\gamma|\Delta H_{\text{FMR}}/2$ expresses the half power FMR linewidth as a decay or relaxation rate in frequency units. The multiplier ε is equal to $|\gamma|(2H_{\text{FMR}} + 4\pi M_s)/2\omega_p$ and represents an ellipticity correction.¹³ For Permalloy films at 10 GHz, this factor is about 2. The above formulas apply to isotropic in-plane magnetized films.

Turn now to the spin wave components denoted by the $\mathbf{m}_{\mathbf{k}}(t)$ terms in Eq. (3). If one includes only linear spin wave terms in the torque equation analysis with no damping and works in the small signal limit with $|\mathbf{m}_{\mathbf{k}}| \ll M_s$, one can obtain the spin wave dispersion relation written here as

$$\omega_{\mathbf{k}}(\mathbf{k}) = |\gamma| \{ [H + Dk^2 + 4\pi M_s(1 - N_k) \sin^2 \theta_k] (H + Dk^2 + 4\pi M_s N_k) \}^{1/2}. \quad (8)$$

The D parameter denotes an effective exchange stiffness field,¹³ $4\pi M_s N_k$ represents an effective dynamic dipole-dipole field, and θ_k is the angle between the in-plane \mathbf{k} vector and the $\hat{\mathbf{z}}$ -directed static field. For Permalloy, D may be taken as 2.1×10^{-9} Oe cm²/rad².¹⁴ Keep in mind that the wave vector \mathbf{k} is constrained to the $\hat{\mathbf{x}}\text{-}\hat{\mathbf{y}}$ film plane. Following Harte,¹⁵ the N_k function may be written as

$$N_k = (1 - e^{-kd})/kd. \quad (9)$$

Recall that d denotes the film thickness. The above relations apply (1) in the magnetostatic limit with wave numbers much larger than the corresponding pure electromagnetic wave k value at $\omega_k = \omega_p$ and (2) under the assumption that $kd \ll 1$ is valid and $\mathbf{m}_{\mathbf{k}}(t)$ is uniform across the film thickness.

Reference 8 gives a detailed discussion of the spin wave dispersion relation in Eq. (8) and the role of the correspond-

ing spin wave band in SA processes. The main difference for RS processes is twofold. First, the relevant spin wave modes are at $\omega_k = \omega_p$ rather than at $\omega_k = \omega_p/2$. Second, the range of fields is limited to those close to the FMR field and the frequency shift of the spin wave band is *much smaller* than that for SA processes. For all practical purposes, one can shift all of the spin wave band diagrams in Fig. 4 of Ref. 8 so that the $k=0$ convergence point is at 9.11 GHz, and draw a horizontal line across the band through this point to define the range of allowed spin wave modes for resonance saturation.

B. Resonance saturation second order processes

The Suhl spin wave instability theory has been recast in various forms by Schloemann,¹⁶ Schloemann *et al.*,¹⁷ Patton,^{18,19} Chen and Patton,²⁰ and Nazarov *et al.*,²¹ among others. In brief, the magnetic torque equation of motion without damping can be taken and the (1) linear terms in $\mathbf{m}_k(t)$ and (2) higher order terms that include products of $\mathbf{m}_k(t)$ and uniform mode amplitudes as well as direct pumping field terms can be considered. As with the uniform mode, it is also convenient to convert the transverse $\hat{x}\text{-}\hat{y}$ part of $\mathbf{m}_k(t)$ into a reduced scalar complex amplitude $a_k(t) = [m_{k,x}(t) + im_{k,y}(t)]/M_s$. Spin wave damping is added at the end of the analysis through the replacement $\omega_k \rightarrow \omega_k + i\eta_k$. The η_k corresponds to the spin wave relaxation rate for the given mode at \mathbf{k} and ω_k . In parallel with the $\eta_0 = \varepsilon|\gamma|\Delta H_{\text{FMR}}/2$ connection, it is useful to cast η_k in terms of a spin wave linewidth parameter $\Delta H_k = 2\eta_k/|\gamma|$ that expresses the spin wave relaxation rate in linewidth units. Note that no ellipticity factor has been incorporated into this connection, so that ΔH_k is not a true linewidth but, rather, serves one simple function to cast η_k into linewidth units.

The final result for second order Suhl processes is a solution for the $a_k(t)$ that takes the form

$$a_k(t) = a_{k0} e^{\beta_k^{(2)} t}, \quad (10)$$

where $\beta_k^{(2)}$ is an exponential growth or decay parameter given by

$$\beta_k^{(2)} = \sqrt{|G_k^{(2)}|^2 - (\omega_k - \omega_p)^2} - \eta_k. \quad (11)$$

In general, $G_k^{(2)}$ is one of several functions that prescribe the coupling between the uniform mode and a given spin wave mode at \mathbf{k} and ω_k . The $G_k^{(2)}$ scales with the square of the uniform mode amplitude and, hence, with h^2 . The fact that the coupling scales with the square of the uniform mode amplitude is the origin of the "second order" label for this particular Suhl process. Details of the analysis may be found in the above cited references.

The form of $\beta_k^{(2)}$ shows the instability effect even without a detailed knowledge of the $G_k^{(2)}$ function. For a sufficiently small h , $G_k^{(2)}$ will be small, $\beta_k^{(2)}$ will be negative, the $a_k(t)$ will always show a decay, there will be no spin wave instability, and the spin wave modes will continue to reside at thermal levels. As h is increased, however, $G_k^{(2)}$ will grow. At the point where $\beta_k^{(2)}$ becomes positive for some mode or set of available (\mathbf{k}, ω_k) modes, there will be a threshold for

the exponential growth in the $a_k(t)$ for these modes. In the experiment, one will see an effect for the particular set of (\mathbf{k}, ω_k) modes with the *lowest threshold*. From Eq. (11), one can see, at the outset, that modes with $\omega_k = \omega_p$ will have a lower $G_k^{(2)}$ than other modes. Subject to this condition, the threshold condition for the unstable growth of parametric spin waves at $\omega_k = \omega_p$ reduces to the relatively simple form $G_k^{(2)} = \eta_k = |\gamma|\Delta H_k/2$.

Apart from the quadratic dependence on h , $G_k^{(2)}$ is in general not a simple function. In order to obtain an h_{crit} determination from the threshold condition, it is useful to separate out the h^2 part of the $G_k^{(2)}$ function according to

$$G_k^{(2)}(k, \theta_k) = \frac{(|\gamma|h)^2}{8\omega_p} W_k^{(2)}(H, k, \theta_k). \quad (12)$$

The new dimensionless $W_k^{(2)}(H, k, \theta_k)$ function includes the remaining dependences on the static field H , the spin wave propagation parameters k and θ_k , and all of the other parameters enumerated above. An explicit recipe for $W_k^{(2)} \times (H, k, \theta_k)$, as obtained directly from the Suhl theory adapted for thin films, is given in Appendix B. The algebra follows from the citations listed above and only the final results in compact form are given in Appendix B.

From the above form, one can see that the theoretical threshold $h_c^{(2)}$ for a general \mathbf{k} mode will be given as $h_c^{(2)} = 2[(\omega_p/|\gamma|)\Delta H_k/W_k^{(2)}(H, k, \theta_k)]^{1/2}$. At a given H , the available k and θ_k values will be defined by the $\omega_k(\mathbf{k})$ dispersion relation of Eq. (8), again subject to the $\omega_k = \omega_p$ constraint. The minimum threshold $h_{\text{crit}}^{(2)}$ that corresponds to the measured h_{crit} is then obtained as the minimum value of $h_c^{(2)}$ among all of the available modes at $\omega_k = \omega_p$.

$$h_{\text{crit}}^{(2)} = 2 \min \left[\sqrt{\frac{\omega_p \Delta H_k}{|\gamma| W_k^{(2)}(H, \theta_k)}} \right]_{\omega_k = \omega_p} \quad (13)$$

The separate k and θ_k parameters have now been replaced by a single θ_k variable. This is because the dispersion constraint, $\omega_k(k, \theta_k) = \omega_p$, allows one to write θ_k as a function of k .

For the present purposes, the spin wave linewidth parameter ΔH_k will be treated as a constant. In general, the spin wave relaxation rate η_k and the corresponding ΔH_k parameter can be a function of the spin wave frequency and wave vector \mathbf{k} . From the butterfly curve fits to be considered shortly, it will become clear that it is not necessary to consider such dependences explicitly in order to match the thin film Suhl theory to the present data. In contrast, this is usually not the case for first order processes.^{8,13} Further comments on this point are given in the next section.

The numerical minimization procedure to obtain a theoretical $h_{\text{crit}}^{(2)}$ for a given H is discussed at length in Ref. 21 and elsewhere. One starts with a fine mesh of the available θ_k values defined by the $\omega_k(k, \theta_k) = \omega_p$ constraint, evaluates the resulting $h_c^{(2)}$ at each point, and selects the minimum value of $h_{\text{crit}}^{(2)}$. At the same time, the values of θ_k and k at this minimum threshold point define the critical mode propagation angle $\theta_{k\text{-crit}}$ and wave number k_{crit} . One then repeats the process for the field range of interest and constructs a theoretical butterfly curve of $h_{\text{crit}}^{(2)}$ vs H as well as predicted field profiles

TABLE II. Summary of parameters for the fits of the Suhl theory to the resonance saturation butterfly curve data for all samples.

Film thickness n (nm)	Static field at the butterfly curve minimum H_{BC}^{min} (Oe)	In-plane static field (IPSF) FMR half power linewidth ΔH_{FMR} (Oe) (from Table I)	Spin wave linewidth (relaxation rate η_k in linewidth units) $\Delta H_k = 2\eta_k/ \gamma $ (Oe)	Equivalent FMR Gilbert damping parameter α_{FMR}	Spin wave Gilbert damping parameter α_k	In-plane precession angle θ_{FMR}^{crit} (deg)
35	808	44	35	0.0072	0.0046	5.5
57	841	41	17	0.0066	0.0026	3.7
74	787	37	16	0.0060	0.0025	3.5
104	830	59	32	0.0093	0.0050	4.9
123	852	56	30	0.0090	0.0048	4.9

for θ_{k-crit} and k_{crit} . This entire process may be repeated with ΔH_k as a control parameter to obtain a best fit to a given experimental h_{crit} vs H profile. One can use such a fit to make an empirical determination of ΔH_k .

VI. BUTTERFLY CURVE FITS AND IMPLICATIONS

Figure 4, as discussed in Sec. IV B, gives representative butterfly curve data for the 104 nm film. The solid curve shows a fit to the data based on the theory summarized in Sec. V. The fit is based on the film parameters listed in Table I, the D value from Sec. V A, and a constant spin wave relaxation η_k value of 2.8×10^8 1/s. Recall that the conversion $\Delta H_k = 2\eta_k/|\gamma|$ is used to cast η_k in convenient linewidth units. The conversion gives $\Delta H_k = 32$ Oe. For reference, the corresponding Gilbert damping parameter, $\alpha_k = (\eta_k/\omega_k)/(\partial\omega_k/\partial|\gamma|H)$, is about 0.005.

The computed $h_{crit}(H)$ response shown in Fig. 4 is accompanied by critical mode k_{crit} and θ_{k-crit} vs H profiles. For the full range of static fields shown the critical mode propagation angles were at $\theta_{k-crit} = 0^\circ$. Interestingly, $\theta_{k-crit} = 0^\circ$ also comes out of the original Suhl SWI theory for bulk isotropic ferrites biased at the FMR field.² The corresponding k_{crit} values are in the small range 9.1×10^5 – 9.6×10^5 rad/cm, with the highest value at the low field limit of the data and the lowest value at the high field limit. Recall that the critical mode ω_k is equal to ω_p for second order processes, so that the $\theta_{k-crit} = 0^\circ$ determination in combination with Eq. (8) completely specifies $k_{crit}(H)$.

From Fig. 4, one can see that the thin film second order Suhl spin wave instability theory, with the spin wave relaxation rate or linewidth taken to be constant, gives a good match to the data. These RS butterfly curve data and the corresponding fits are only the second such results of record. The first such results, by Cox *et al.*,⁹ were for in-plane magnetized single crystal Zn–Y-type hexagonal ferrite disks with planar anisotropy. For these samples, the Suhl theory with a constant η_k gave only a poor qualitative fit to the data. Good semiquantitative fits required the introduction of a substantial k -dependent component to the spin wave relaxation rate.

The ability to achieve a good theoretical fit to the experimental butterfly curve for a *single* η_k value in the case of metallic ferromagnetic films is likely due to the simple fact that the critical mode wave vector remains essentially constant over the full FMR profile. As noted above, the k_{crit} values are all limited to a very small range, 9.1×10^5 – 9.6

$\times 10^5$ rad/cm, while the critical mode remains at $\theta_{k-crit} = 0^\circ$. The resultant shape of the theoretical butterfly curve is then determined only by the uniform mode susceptibility and the corresponding field dependent coupling factor $W_k^{(2)}(H, k, \theta_k)$ defined above and given in detail in the Appendix. In contrast, the changes in the critical mode k_{crit} and θ_{k-crit} values over the wide range of fields associated with the SA butterfly curve in An *et al.*⁸ are substantial and the resultant fits to the SA butterfly curves were k dependent. Figure 6 in Ref. 8 shows, in particular, that the k_{crit} and θ_{k-crit} values range from about 1.5×10^5 to 3.0×10^5 rad/cm and from 0° to 17° , respectively.

Table II summarizes the results from similar fits for the full ensemble of films. Again, the fits are based on the film parameters listed in Table I and the D value from Sec. V A. The critical modes for all the fits were at $\theta_{k-crit} = 0^\circ$ and the corresponding narrow range of k_{crit} values defined by the $\omega_k = \omega_p$ constraint and the change in field. The fits for the 35 and 123 nm thick films were similar to that shown in Fig. 4 for $d = 104$ nm. The data for the other two samples showed good fits for fields down to about 60 Oe or so below the butterfly curve minimum but poor fits for lower fields. For some reason, the measured h_{crit} values in this lower field range for these samples show a more rapid increase than the smooth data trend and corresponding theoretical response in Fig. 4.

The table gives results for all five samples. It lists the measured static fields at the butterfly curve minimum (H_{BC}^{min}), the FMR linewidths and α_{FMR} values from Table I, the spin wave linewidths (ΔH_k) and the Gilbert damping parameters (α_k) from the butterfly curve fits, and the in-plane FMR precession angles (θ_{FMR}^{crit}) at threshold. The Gilbert damping parameter associated with ferromagnetic resonance, α_{FMR} , is generally taken as the standard measure of the FMR loss. As such, the corresponding α_k parameter for spin waves can provide a useful basis for comparison here. The FMR precession angle at threshold is also a useful measure of the instability response. The initial effect as the microwave power exceeds the Suhl threshold is a lockup in the uniform mode precession cone at θ_{FMR}^{crit} as energy is pumped into spin waves. This angle, therefore, is an important parameter in spin wave instability processes.

Apart from the expected match up between the H_{BC}^{min} values and the IPSF H_{FMR} values in Table I, there are three main points to be made from the results in Table II. First, one can see that the spin wave Gilbert damping parameter α_k values

from the butterfly curve fits are lower, sometimes by a factor of 2 or more, than the corresponding FMR Gilbert damping parameter α_{FMR} values. Note that the α_{FMR} values in Tables I and II are based solely on the measured linewidths and the $\Delta H_{\text{FMR}} = 2\alpha_{\text{FMR}}\omega_p/|\gamma|$ connection. These α_{FMR} values likely contain the effects of inhomogeneity and two magnon effects as well as the intrinsic magnon-electron scattering losses normally ascribed to the α parameter.^{22,23} On the other hand, the generally lower α_k values are the result of the fact that the Suhl SWI derives from the renormalized mode with the lowest threshold. Renormalization can reduce, and in some cases eliminate, the broadening effects due to inhomogeneities, for example. The generally lower α_k values listed in the second to last column of Table II are in the 0.002–0.005 range nominally associated with intrinsic magnon-electron processes.^{24–26}

Second, it is also important to note that two magnon scattering effects are expected to affect the extrapolated h_{crit} values of the sort shown in Fig. 3 to some degree. It was already noted in connection with Fig. 3 that the change from the expected abrupt transition at threshold to a rounded response is a two magnon effect. This introduces a certain level of ambiguity in any determination of a specific h_{crit} value. Any corresponding effect on h_{crit} will also modify the fitted α_k . For a complete threshold analysis that includes two magnon effects, it is necessary to include not only the nonlinear interactions between the uniform mode and spin wave modes but also the interactions between the parametric spin waves. These additional terms complicate the theory greatly. Zakharov and Lvov²⁷ and Cherepanov,²⁸ among others, have calculated the increase in threshold due to two magnon effects for first order Suhl SWI processes. But calculations have not been done for second order processes. Apart from a recent conference presentation,¹⁰ however, there has been no detailed analysis of two magnon effects on second order RS instability processes. Such work is in progress.

The third and final point concerns the FMR precession angle just at the Suhl threshold, the lock-up angle $\theta_{\text{FMR}}^{\text{crit}}$. The last column in Table II shows the calculated in-plane FMR precession angle just at threshold. One can see that this angle is generally in the range of a few degrees. As one moves above threshold, the lockup gradually relaxes, but there is a sizable increase in loss, well above the levels indicated by all of the ΔH_k and α_k parameters discussed above.²⁹ Large angle precession dynamics is an important element in many magnetic sensor and information storage applications, among others. Reference 1 describes one way to adapt Suhl theory to large angle switching dynamics. The present lock-up angle determinations provide a measure of the inherent limitations in a simple damped equation of motion analysis of large angle switching processes and the switching angle limits for the validity of such analyses.

VII. SUMMARY AND CONCLUSION

Resonance saturation FMR profiles have been measured as a function of microwave power and spin wave instability threshold h_{crit} measurements have been made over the full FMR absorption line for a series of Permalloy films at

9.11 GHz and room temperature. Careful attention to cavity loading and calibration issues has yielded the first comprehensive data on Suhl spin wave instability processes at FMR and over the full FMR profile for thin metal films. For each film, a theoretical analysis of the threshold data, based on the Suhl theory, suitably modified for thin films, yielded good fits to the butterfly curve data on h_{crit} versus in-plane static field H based on a single field independent value of the spin wave linewidth. These linewidths and the corresponding Gilbert damping parameter values are consistent with those expected for intrinsic magnon-electron relaxation. The implicit critical modes are consistent with the original Suhl theory and the FMR precession angles at threshold are quite small, on the order of few degrees.

These conclusions also raise several questions for future study. First, the evolution in the shapes of the FMR profiles with power and the apparent connections between these shapes and two magnon effects reported by Krivosik need further study. The second question, also related to two magnon effects, relates to the lack of a sharp threshold response and the rounded onset curves in Fig. 3. Finally, there are important questions about the response well above threshold and the connections between large angle switching processes, resonance saturation effects in FMR, and spin wave instability processes. The present results show that SWI processes result in a relatively small FMR precession lock-up angle. How are these processes connected to those that operate in large angle dynamics?

ACKNOWLEDGMENTS

This work was supported in part by the Information Storage Industry Consortium EHDR program, the Office of Naval Research, Grant No. N00014-06-1-0889, and the U.S. Army Research Office, Grant No. W911NF-04-1-0247. The late Professor S. Konishi of Kyushu University, Fukuoka, Japan provided the Permalloy films used in this work. Dr. Ralf Meckenstock, of the University of Duisburg-Essen, Germany, is acknowledged for helpful information on low linewidth films and intrinsic Gilbert damping values.

APPENDIX A

This appendix provides technical details on the determination of the calibration coefficient $C = h^2/P$. First, a point-by-point calibration of the cavity was done over the entire FMR profile, typically in 5–10 Oe steps, depending on the linewidth. Details on the determination of C in terms of the basic cavity parameters may be found in Refs. 11 and 30. These calibration data were then used to determine the C vs H response. As mentioned in Sec. III B, these C values, for a given cavity, are actually a *universal function* of the cavity reflection coefficient ρ . This means that one can use a universal $C(\rho)$ response function for all of the data for different samples, different coupling angles, and different static fields. This is also consistent with the $C = A(1-\rho)^2$ result from perturbation theory, where A is a known function of the cavity mode, cavity volume, and frequency.¹¹

Figure 5 shows representative data for the 104 nm thin film at 9.11 GHz. The coupling angle was at $\theta = 60^\circ$, with

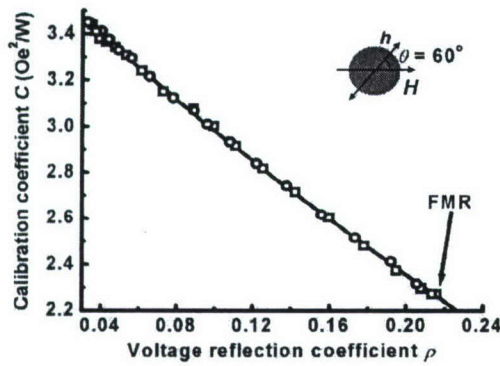


FIG. 5. Calibration coefficient C vs voltage reflection coefficient ρ for the 104 nm thin film at 9.11 GHz. The inset shows the coupling geometry, with the in-plane static field H and the in-plane linearly polarized microwave field h at a coupling angle θ of 60° , as indicated. The pumping frequency was 9.11 GHz. The data are for a cw microwave input power at about 10 dBm. The open square data points are for fields from 700 to 830 Oe and the open circle data points are for H values from 825 to 960 Oe. The arrow indicates the open square data point associated with the FMR peak. The solid line shows the theoretical response based on $C=A(1-\rho)^2$ with A set to $3.68 \text{ Oe}^2/\text{W}$.

both fields in plane as in the inset. The field ranged from 700 to 960 Oe. Recall that the low power FMR peak is at $H=830$ Oe. The cavity voltage reflection coefficient ρ ranged from about 0.22 at the FMR point to 0.03 at the high and low field end limits given above. The Q_L change over the range of the data was less than 20% and in line with the criteria established in Sec. III B. The data in Fig. 5 are shown in a C vs ρ format. For the undercoupled cavity, ρ is a maximum at the indicated FMR point. As one moves away from the FMR peak, either to lower or higher fields, ρ decreases. The open circles and squares correspond to fields above and below the FMR point, respectively. The solid line shows a best fit to the data, based on $C=A(1-\rho)^2$, with A taken as a single fitting parameter. The fit shown is for $A=3.68 \text{ Oe}^2/\text{W}$. The χ^2 parameter for the fit was 0.000 13.

Figure 5 demonstrates two major points. First, the fact that the above resonance and the below resonance data fall on the same C vs ρ response curve provides proof that the universal $C(\rho)$ response function assumption is valid. Second, the fact that the data match the $C=A(1-\rho)^2$ relation provides further support for the thesis that perturbation theory is indeed applicable. The A value for the $C=A(1-\rho)^2$ fit is nominally the same as obtained from perturbation theory. For the nominal Q_L from the cavity calibrations and the cavity frequency, along with the volume and mode parameters for the cavity, one obtains a theoretical A value of $3.54 \text{ Oe}^2/\text{W}$.

Based on these results, one can see that a universal $C(\rho)$ function obtained either empirically or directly from perturbation theory is adequate for the cavity response calibration. The above procedure was repeated for all samples. In all cases, the same $C(\rho)$ calibration function was obtained.

APPENDIX B

This appendix gives working equations for the second order spin wave instability coupling coefficient $W_k^{(2)}$ needed for the h_{crit} analysis in Sec. V. This $W_k^{(2)}$ is written as

$$W_k^{(2)} = W_1 + W_2 + W_3 + W_4 + W_5. \quad (\text{B1})$$

The W_1 , W_2 , W_3 , W_4 , and W_5 functions are given by

$$W_1 = q_L^2 [r(A_k + \omega_p) - B_k v], \quad (\text{B2})$$

$$W_2 = q_A^* [r(A_k - \omega_p) - B_k v], \quad (\text{B3})$$

$$W_3 = q_A^* q_L [s(A_k + \omega_p) + s(A_k - \omega_p) - B_k u], \quad (\text{B4})$$

$$W_4 = \frac{1}{2} q_L (A_k + \omega_p - B_k), \quad (\text{B5})$$

and

$$W_5 = \frac{1}{2} q_A^* (A_k - \omega_p - B_k). \quad (\text{B6})$$

The A_k and B_k functions are given by

$$A_k = \omega_H + |\gamma| Dk^2 + \frac{1}{2} \omega_M [(1 - N_k) \sin^2 \theta_k + N_k] \quad (\text{B7})$$

and

$$B_k = \frac{1}{2} \omega_M [(1 - N_k) \sin^2 \theta_k - N_k]. \quad (\text{B8})$$

The r , v , s , and u functions are given by

$$r = \frac{1}{4} \omega_M [(1 - N_k) 2 \cos^2 \theta_k - 1] + \frac{1}{2} |\gamma| Dk^2, \quad (\text{B9})$$

$$v = \frac{1}{4} \omega_M, \quad (\text{B10})$$

$$s = -\frac{1}{4} \omega_M [(1 - N_k) \sin^2 \theta_k - (1 + N_k)], \quad (\text{B11})$$

and

$$u = \frac{1}{2} \omega_M [(1 - N_k) (3 \cos^2 \theta_k - 1) - (1 + N_k)]. \quad (\text{B12})$$

The q_L and q_A parameters correspond to the Larmor and anti-Larmor uniform mode response functions given in Sec. V. Also as defined in Sec. V, the ω_M and ω_H express $4\pi M_s$ and H in frequency units and are equal to $|\gamma| 4\pi M_s$ and $|\gamma| H$, respectively.

¹A. Yu. Dobin and R. H. Victora, J. Appl. Phys. **95**, 7139 (2004).

²H. Suhl, J. Phys. Chem. Solids **1**, 209 (1957).

³A. N. Slavin and P. Kabos, IEEE Trans. Magn. **41**, 1264 (2005).

⁴M. A. Hoefer, M. J. Ablowitz, B. Ilan, M. R. Pufall, and T. J. Silva, Phys. Rev. Lett. **95**, 267206 (2005).

⁵J. B. Comly, T. Penney, and R. V. Jones, J. Appl. Phys. **34**, 1145 (1963).

⁶A. Berteaud and H. Pascard, J. Appl. Phys. **36**, 970 (1965).

⁷A. Berteaud and H. Pascard, J. Appl. Phys. **37**, 2035 (1966).

⁸S. Y. An, P. Krivosik, M. A. Kramer, H. M. Olson, A. V. Nazarov, and C. E. Patton, J. Appl. Phys. **96**, 1572 (2004).

⁹R. G. Cox, C. E. Patton, M. A. Wittenauer, P. Kabos, and L. Chen, J. Appl. Phys. **89**, 4454 (2001).

¹⁰P. Krivosik, Technical Digests, IEEE International Magnetism Conference, San Diego, CA, 8–12 May 2006 (unpublished), Raytheon Tech. Report No. R-48.

¹¹J. J. Green and T. Kohane, SCP Solid State Tech **7**, 49 (1964).

¹²H. Suhl, J. Appl. Phys. **30**, 1961 (1959).

- ¹³C. E. Patton, in *Magnetic Oxides*, edited by D. J. Craik (Wiley, London, 1975), pp. 575–645.
- ¹⁴M. Nisenoff and R. W. Terhune, J. Appl. Phys. **36**, 732 (1965).
- ¹⁵K. J. Harte, J. Appl. Phys. **39**, 1503 (1968).
- ¹⁶E. Schloemann, Technical Abstract No. R-48, 1959 (unpublished).
- ¹⁷E. Schloemann, R. I. Joseph, and I. Bady, J. Appl. Phys. **34**, 672 (1963).
- ¹⁸C. E. Patton, Phys. Status Solidi B **92**, 211 (1979).
- ¹⁹C. E. Patton, J. Appl. Phys. **40**, 2837 (1969).
- ²⁰M. Chen and C. E. Patton, in *Nonlinear Phenomena and Chaos in Magnetic Materials*, edited by P. E. Wigen (World Scientific, Singapore, 1994), Chap. 3.
- ²¹A. V. Nazarov, C. E. Patton, R. G. Cox, L. Chen, and P. Kabos, J. Magn. Mater. **248**, 164 (2002).
- ²²S. S. Kalarickal, D. Menard, J. Das, C. E. Patton, X. Zhang, L. C. Sengupta, and S. Sengupta, J. Appl. Phys. **100**, 084905 (2006).
- ²³V. Kambersky and C. E. Patton, Phys. Rev. B **11**, 2668 (1975).
- ²⁴R. Meckenstock, D. Spoddig, Z. Frait, V. Kambersky, and J. Pelzl, J. Magn. Mater. **272**, 1203 (2004).
- ²⁵Z. Frait and D. Fraitová, J. Magn. Mater. **15**, 1081 (1980).
- ²⁶R. Meckenstock, O. von Geisau, J. Pelzl, and J. A. Wolf, J. Appl. Phys. **77**, 6439 (1995).
- ²⁷V. Zakharov and V. S. Lvov, Sov. Phys. Solid State **14**, 2513 (1973).
- ²⁸V. B. Cherepanov, Phys. Rev. B **45**, 12397 (1992).
- ²⁹T. Gerrits, P. Krivosik, M. L. Schneider, C. E. Patton, and T. J. Silva, Phys. Rev. Lett. **98**, 207602 (2007).
- ³⁰C. E. Patton and J. J. Green, Rev. Sci. Instrum. **42**, 193 (1971).

The low field microwave effective linewidth in polycrystalline ferrites

Nan Mo,^{a)} Jerome J. Green, Pavol Krivosik,^{b)} and Carl E. Patton
Department of Physics, Colorado State University, Fort Collins, Colorado 80523

(Received 25 July 2006; accepted 4 November 2006; published online 25 January 2007)

High precision measurements on the low and high field effective linewidth ΔH_{eff} at 10 GHz have been made on ultradense (UD) and conventionally sintered (CS) polycrystalline yttrium iron garnet (YIG) materials. The high field data confirm previous results on the role of two magnon scattering to low wave number (k) electromagnetic Larmor branch spin waves that lie below the light line. The low field data reveal two important contributions to the effective linewidth. For a field regime from the low k edge of the usual dipole exchange spin wave band down to the point in field ($H=H_X$) where above-the-light-line electromagnetic branch Larmor (EML-HI) spin waves appear, ΔH_{eff} is connected with scattering to relatively high k dipole exchange Larmor (DEL) spin waves. The coupling to these modes comes from grain boundaries in the YIG materials. A grain boundary scattering theory gives reasonable agreement with the data. While the high field effective linewidth due to pseudo in-manifold scattering is larger for the CS samples compared to that for the UD samples, the high k DEL scattering is larger for the UD samples compared to that for the CS samples. This is due to the dominant role of the grain boundaries in the low field ΔH_{eff} . For fields below H_X , additional scattering appears for the EML-HI modes. The abrupt appearance of an additional ΔH_{eff} component for $H < H_X$ provides direct experimental evidence for the presence of such modes in the spin wave dispersion. Part of the loss contribution for $H < H_X$ may be due to subthreshold nonlinear effects. © 2007 American Institute of Physics. [DOI: 10.1063/1.2426379]

I. INTRODUCTION

In the last decade, an increasing need for low loss polycrystalline ferrite materials for high frequency applications has provided an impetus for renewed work on the fundamental understanding of microwave loss and relaxation, damping processes, and precessional dynamics in such systems. Ferromagnetic resonance (FMR) and the FMR linewidth have long been the mainstay for such work.

In the late 1960s and 1970s, however, there was a gradual realization that the off resonance losses, expressed in terms of an effective linewidth, could be substantially lower than those defined through a single FMR linewidth parameter. Just as the usual field swept FMR linewidth ΔH is an expression of the uniform mode relaxation rate η_0 at resonance, given by $\Delta H = 2\eta_0/|\gamma|$ for spherical samples, for example, the effective linewidth ΔH_{eff} expresses the relaxation rate $\eta(H)$ for a general static external magnetic field H in field units according to $\Delta H_{\text{eff}} = 2\eta(H)/|\gamma|$. This ΔH_{eff} parameter has proven to be a convenient basis for the comparison of off resonance losses with FMR losses as well as off resonance losses for different materials, microstructures, etc. In the above, γ denotes the electron gyromagnetic ratio of the material of interest. All equations here and below are in Gaussian units.

These H -dependent losses can be extremely important because the now well-accepted two magnon scattering contributions to the microwave losses in many magnetic systems

can be field and frequency dependent. Microwave measurements at high or low field, very far from the FMR field for a given drive frequency, correspond to a density of states (DOS) situation for degenerate magnon modes that is very different from the situation at ferromagnetic resonance. There are also many microwave magnetic devices that operate at fields that are very far from the FMR field. The corresponding losses can be quite different from those inferred from a single FMR linewidth parameter.

The basic effective linewidth results from the 1960s and 1970s have stood unchallenged until recent work by Mo *et al.*¹ The old work confirmed four expected effects. (1) The effective linewidth is field dependent. (2) It is large and shows considerable structure in the manifold region, where there are a large number of low wave number spin waves that are degenerate with the driven FMR mode. (3) At very high fields, it is generally much lower than the FMR linewidth and the in-manifold ΔH_{eff} . (4) At H values well below FMR field but still sufficient to achieve a saturated sample, ΔH_{eff} is typically a little higher than the average high field values.

The old data, however, also showed two key contradictions. First, the average high field effective (HFE) linewidth, denoted as $\Delta H_{\text{eff}}^{(\text{HF})}$, was always higher than the corresponding FMR linewidths in single crystals.² This is problematic because at high field, the spin wave band is shifted to frequencies that are much higher than the drive frequency, and there should be no two magnon scattering contribution whatsoever to the linewidth. This means that $\Delta H_{\text{eff}}^{(\text{HF})}$ should be identical to the intrinsic single crystal linewidth.³ Second, $\Delta H_{\text{eff}}^{(\text{HF})}$ was also found to have a strong microstructure dependence.^{2,4,5} There are substantial increases in $\Delta H_{\text{eff}}^{(\text{HF})}$

^{a)}Electronic mail: monan@lamar.colostate.edu

^{b)}On leave from the Department of Electromagnetic Field Theory, Faculty of Electrical Engineering and Information Technology, Slovak University of Technology, Bratislava, Slovakia.

with both increasing porosity and decreasing grain size. Both responses are inconsistent with the idea of a high field “intrinsic” loss parameter in the absence of two magnon scattering.

The work in Ref. 1 has resolved many of these contradictions. The authors were able to perform meticulous high accuracy measurements of $\Delta H_{\text{eff}}^{(\text{HF})}$ vs H in both conventionally sintered (CS) and ultrahigh density (UD) hot isostatic pressed (hipped) samples of polycrystalline yttrium iron garnet (YIG) spheres. The data showed that $\Delta H_{\text{eff}}^{(\text{HF})}$ is, in fact, not constant at high field, but instead decreases steadily as the field is increased. Remarkably, $\Delta H_{\text{eff}}^{(\text{HF})}$ approaches single crystal YIG linewidth values in the high field limit. Equally remarkable, Ref. 1 also established a correlation between the $\Delta H_{\text{eff}}^{(\text{HF})}(H)$ response and the field dependent density of states for low wave number electromagnetic spin wave (EMSW) modes. Two magnon scattering from the driven FMR mode to these extremely long wavelength EMSW modes had not been considered previously.

The above HFE linewidth results also lead to further realizations about the low field effective (LFE) linewidth response. The focus in Ref. 1 was on the EMSW modes that are slightly below the $\omega = ck_0/\sqrt{\epsilon_r}$ light line dispersion, where ω is angular frequency, c is the light speed in vacuum, k_0 is the wave number (k) for pure electromagnetic waves, and ϵ_r is the relative dielectric constant. It is these low k and low ω below-the-light-line EMSW modes that give rise to the HFE linewidth response discussed in Ref. 1. The important point for the present work is that there are also low k and high ω EMSW modes that lie above the light line. Based on the high field effective linewidth results in Ref. 1, it is expected that both sets of EMSW modes, as well as the usual high k dipole exchange spin wave modes, can have a significant effect on the low field effective linewidth.

This paper reports on recent measurements of the LFE linewidth, $\Delta H_{\text{eff}}^{(\text{LFE})}(H)$, and makes connections with the various classes of spin wave modes enumerated above. As with the connections in Ref. 1 between the HFE linewidth and the below-the-light-line EMSW modes, this connection is possible only because of (1) the extended capabilities for high accuracy effective linewidth measurements and (2) the refined understanding of the role of the EMSW and the dipole exchange branch spin waves in two magnon scattering.

Section II considers materials and the microwave measurement methods. Section III presents the experimental results. Section IV provides theoretical connections. Section IV A gives a brief overview of the spin wave band considerations relevant to the effective linewidth problem and Sec. IV B gives qualitative connections with the data from Sec. III. Sections IV C and IV D provide working equations for a theory of grain boundary scattering (GBS) and give quantitative connections with the low field effective linewidth data. Section V gives a summary and conclusion.

II. FERRITE MATERIALS AND MEASUREMENT METHODS

The samples and the details of the cavity measurement technique for the determination of effective linewidth are

described in Ref. 1. This section provides a brief recap of the samples, the effective linewidth measurement, and analysis methods, and adds additional information that is needed to deal with the low field case.

The samples consist of nominal 2 mm diameter spheres fabricated from ultradense polycrystalline YIG and conventionally sintered Trans Tech G113 YIG starting materials. The UD sample is 99.9% dense or greater, relative to the theoretical YIG density. The CS sample is greater than 99% dense. High density gives low loss. The porosity contributions to the linewidth that often dominate the losses in many ferrites become small and even negligible.⁶ Hence, many of the fine points related to intrinsic and two magnon scattering losses can be readily investigated. Another important consideration for the LFE linewidth will relate to grain size. The hiped UD sample has a nominal grain size of about 8 μm , while the CS G113 YIG samples have a grain size on the order of 20 μm .

The cavity is the same as in Ref. 1, a TE_{011} cylindrical cavity with a nominal center frequency of 10 GHz and nominal quality Q factor of 22 000. Based on the metrological ABA method given in Ref. 1, the cavity center frequency ω and quality factor Q were measured as a function of static external field H from a high field limit value of 7 kOe down to a low field limit of 1 kOe. As in Ref. 1, fields in the bulk manifold region of degenerate moderate k spin waves from 3 to 4.5 kOe were excluded. The high losses in the manifold region generally cause a severe degradation in the Q of the cavity and precision Q measurements are not possible. The low field limit of 1 kOe is set by the onset of sample demagnetization effects. The high field limit of 7 kOe was adequate to obtain the high field limit cavity frequency and Q values needed for the analysis.

For effective linewidth measurements in the low field regime, it is necessary to go beyond the approximate treatment for the high field ΔH_{eff} analysis in Ref. 1. At low field, one cannot assume *a priori* that the condition $\Delta H_{\text{eff}} \ll H$ is valid. In addition, one cannot take the operational gyromagnetic ratio parameter that appears in the susceptibility expressions equal to the intrinsic gyromagnetic ratio. The equations below summarize the approach that gives exact expressions for ΔH_{eff} that are generally valid at any field, out of as well as in manifold.

One starts with the standard small signal microwave response of a spherical ferrite sample defined through the complex external susceptibility tensor χ_e . In the experiment, the cavity is used to measure the diagonal component χ_e of this tensor. It is convenient to rewrite χ_e explicitly in terms of the real part χ'_e and the negative imaginary part χ''_e , or as $\chi_e = \chi'_e - i\chi''_e$. The power absorbed by a ferrite sample scales with χ''_e . The full width at half maximum of the χ''_e versus field profile corresponds to the usual FMR linewidth ΔH . As will be evident shortly, data for both χ'_e and χ''_e are needed to obtain the effective linewidth ΔH_{eff} as a function of field.

One may obtain relatively simple expressions for χ_e from a torque equation of motion analysis with microwave loss introduced through a complex frequency approach or other means. For uniformly magnetized nonconducting spherical samples with a uniform linearly polarized micro-

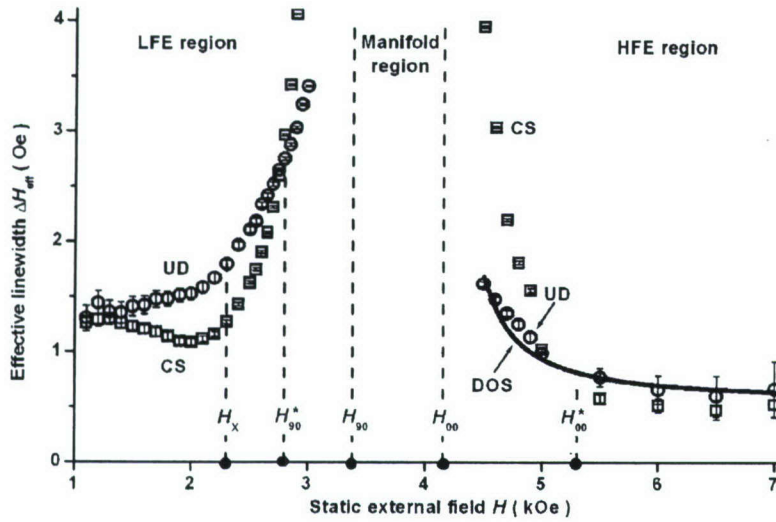


FIG. 1. Measured out-of-manifold effective linewidth ΔH_{eff} as a function of static external field H from 1 to 3 kOe and from 4.5 to 7 kOe for the nominal 2 mm diameter ultradense (UD) hiped and conventionally sintered (CS) YIG spheres at a nominal signal drive frequency of 10 GHz. The open circles and the open squares show the UD and the CS data, respectively. The error bars are shown for all data points. The vertical dashed lines indicate five important field reference points related to the spin wave band at $H_x = 2.3$ kOe, $H_{90} = 2.8$ kOe, $H_{90}^* = 3.38$ kOe, $H_{00} = 4.15$ kOe, and $H_{00}^* = 5.3$ kOe. The low field effective (LFE) linewidth, manifold, and high field effective (HFE) linewidth regions are also labeled. The solid curve in the high field regime shows a best fit to the UD data based on $\Delta H_{\text{eff}} = A \cdot \text{DOS} + \Delta H_b$, where A is a constant scale factor, DOS denotes the density of states for the Larmor electromagnetic branch spin waves, and ΔH_b is a constant background linewidth parameter.

wave drive at frequency ω and a harmonic time dependence taken as $e^{+i\omega t}$, one may write the complex susceptibility as⁴

$$\chi_e = \chi_e' - i\chi_e'' = \frac{|\gamma| M_s (|\gamma| H + i\eta)}{(|\gamma| H + i\eta)^2 - \omega^2}, \quad (1)$$

where M_s denotes the magnetization of the sample and ω is the microwave drive frequency. The nominal saturation induction $4\pi M_s$ for YIG is 1750 G. The in phase χ_e' part of the response corresponds to dispersion. The out of phase χ_e'' part corresponds to loss.

In the past work, various ways have been used to extract $\Delta H_{\text{eff}}(H)$ from measurements of $\chi_e'(H)$ and $\chi_e''(H)$. A simple and direct method is used here. Based on Eq. (1) and the $\Delta H_{\text{eff}} = 2\eta/|\gamma|$ connection, the effective linewidth can be obtained as

$$\Delta H_{\text{eff}} = \frac{2M_s H \chi_e''}{2H[(\chi_e')^2 + (\chi_e'')^2] - M_s \chi_e'}. \quad (2)$$

It is noteworthy that the working equation for ΔH_{eff} given in Eq. (2) does not involve the gyromagnetic ratio γ . In the present approach, a numerical value of γ is needed only for the cavity calibration needed for the determination of χ_e' and χ_e'' at a given field H . Calibration is considered below. Apart from this operation, therefore, γ does not play a crucial role in the analysis.

Based on standard microwave cavity perturbation theory methods, χ_e' and χ_e'' are related to the various cavity parameters through the equations $4\pi\chi_e' = -K(\omega - \omega_\infty)/\omega$ and $4\pi\chi_e'' = K(1/Q - 1/Q_\infty)/2$.⁷ In the above, ω_∞ and Q_∞ correspond to the frequency and quality factor of the cavity, respectively, with the magnetic effects frozen out, so to speak. The K parameter is a cavity calibration factor that scales with the volume of the sample and depends on the nature of the electromagnetic mode in the cavity. These parameters are generally obtained from high field measurements with the sample in place and a high field extrapolation procedure. These calibration parameters are then taken to be applicable over the full out-of-manifold high and low field regimes. The above connections are valid as long as the sample loading of the cavity is relatively small and the changes in ω and Q , relative

to ω_∞ and Q_∞ , are not too large. Reference 1 contains complete details on the overall high field cavity calibration procedure. It is based on the fact that in the high field limit, χ_e' for the uniform mode is a function of H , M_s , ω , and γ only. No linewidth parameter is involved. The M_s value for YIG is known. One can see from the cavity response equations given above that the measured frequency ω should be a linear function of $4\pi\chi_e'(H, M_s, \omega, \gamma)$ with a slope of $-1/K$ and an intercept of ω_∞ . The operational procedure was to (1) measure ω vs H in the high field regime, (2) plot the frequency as a function of $4\pi\chi_e'(H, M_s, \omega, \gamma)$, and (3) determine the γ value that renders the best linear function. The slope of this fit then gives K . In Ref. 1, the nominal free electron value of γ was used. The fitted γ values from the present procedure were slightly off the free electron value and consistent with known values for YIG.

Prior to the application of the full susceptibility analysis to obtain $\Delta H_{\text{eff}}(H)$ from the ω and Q data, an additional correction was applied to the measured Q values to account for the small but possibly significant frequency dependence of the nonmagnetic part of the quality factor. In the working equations given above, it is assumed that the Q change with field comes only from the magnetic losses. However, the change in the cavity frequency due to the change in χ_e' with field can also affect the Q through the frequency dependence of the conductivity losses in the cavity walls. The nonmagnetic Q of a microwave cavity generally scales with the inverse of the electromagnetic skin depth of the metal that makes up the cavity, and this skin depth, in turn, scales with $1/\sqrt{\omega}$.⁸ If the frequency changes are small, this means that the frequency shift Q correction is given as $\delta Q = Q_\infty(\omega - \omega_\infty)/2\omega$ and the $4\pi\chi_e''Q$ connection changes to $4\pi\chi_e'' = K[1/(Q - \delta Q) - 1/Q_\infty]/2$. One uses δQ , as obtained directly from the data, to back correct from the measured Q and f at a given field to the value without the eddy current shift of the nonmagnetic Q from Q_∞ . For the present low loss samples, this correction, along with the changes in the ΔH_{eff} calculation procedure from that used in Ref. 1, amount to a change in the LFE linewidth by 10% or less.

III. EFFECTIVE LINEWIDTH EXPERIMENTAL RESULTS

Figure 1 shows representative measurement results on the nominal 10 GHz out-of-manifold effective linewidth at both low and high fields. The open circles and squares show the data for the UD and the CS YIG samples, as indicated. The graph shows HFE linewidth data for fields from about 4.5 to 7 kOe and LFE linewidth data for fields from about 1 to 3 kOe. No data are shown in the high loss manifold region delineated by the vertical dashed lines at $H = 3.3$ kOe (H_{90}) and $H = 4.15$ kOe (H_{00}), or below 1 kOe in the region where spherical samples start to demagnetize. The vertical dashed lines labeled H_{00}^* and H_{90}^* are the shifted H_{00} and H_{90} field points which are shifted due to local pore demagnetizing fields.⁵ The vertical dashed H_X reference line marks a transition field for EMSW dispersion properties. These field designations will be important for the discussion of Sec. IV. The solid curve overlaid to the data in the HFE region with the DOS label shows a fit to the UD data as described in the caption. These fit results will be considered shortly.

What do these data show? Consider the high field (HFE) region first. The high field data for both samples show a gradual decrease in effective linewidth as the field is increased. For fields above the H_{00}^* point, both sets of data also closely follow to the scaled DOS curve. For fields below the H_{00}^* point, however, the HFE linewidth data points for the CS sample break from the UD data and the computed DOS curve. This break is related to pore-demagnetizing field and pseudo-in-manifold two magnon scattering effects.⁹ Such pseudo-in-manifold two magnon scattering will also be a consideration for the LFE linewidth results.

For the low field effective linewidth results, there are two general observations and several important details. The first general observation is that the LFE linewidths in Fig. 1 are generally larger than the HFE linewidth values. The second is that the relative UD and CS ΔH_{eff} values are now reversed, as compared to the high field response. The LFE linewidths for the UD sample are generally larger than those for the CS sample.

With regard to the details, the most obvious point is in the change in the ΔH_{eff} vs H responses for both samples close to the H_X point. Above $H = H_X$ but below $H = H_{90}^*$, both linewidths increase rapidly with field but the change for the CS sample is more rapid than that for the UD sample. The CS linewidths start out smaller but increase more rapidly than the UD as one moves from the H_X point to larger fields. There is also an apparent crossover of the data for the two samples at a field close to $H = H_{90}^*$. Finally, as one moves below $H = H_X$, the ΔH_{eff} for the UD sample continues to decrease, albeit with a weaker response, while the CS data show an increase.

IV. TWO MAGNON SCATTERING AND THE EFFECTIVE LINEWIDTH

A. Spin wave band considerations

In order to analyze and understand the data presented above, it is necessary to consider the multiband spin wave picture from Ref. 1 for high fields and extend this picture to

the low field regime as well. The spin wave bands that result from a full solution of Maxwell's equations and the linearized torque equation of magnetization motion for plane wave spin waves in an infinite insulating medium were presented in the seminal text *Microwave Ferrites and Ferrimagnetics* by Lax and Button.¹⁰ One may also write the analytical spin wave band response in the form of a governing equation,

$$H_i = 4\pi M_s \left[\frac{k^2(1 + \cos^2 \theta_k)}{2(k^2 - k_0^2)} - 1 \right] - Dk^2 \pm \sqrt{\frac{\omega_k^2}{\gamma^2} + \frac{(4\pi M_s)^2 k^4 \sin^4 \theta_k}{4(k^2 - k_0^2)^2}} = H - \frac{4\pi M_s}{3}. \quad (3)$$

In the above, H_i denotes the static internal field, θ_k denotes the spin wave polar propagation angle relative to the static field direction, ω_k is the spin wave frequency, and D is an exchange parameter. All other parameters are the same as given previously. Equation (3) applies to any material with a homogeneous internal field. The last term, $H - 4\pi M_s/3$, is included only to make a specific connection with the external field H for spherical samples. When one chooses the "+" in front of the square root term, one obtains the dispersion branches for modes with a Larmor (L) sense of precession. Choice of the "-" gives the anti-Larmor (A) precession branches. Recall that $k_0 = \sqrt{\epsilon_r} \omega/c$ denotes the wave number for pure electromagnetic waves. For YIG materials, one has $\epsilon_r \approx 10$ and $D \approx 5.2 \times 10^{-9}$ Oe cm².

One can view Eq. (3) in several ways. The traditional way is to consider the field H (or H_i) as fixed and examine the various $\omega_k(k)$ dispersion bands that are formed as θ_k is scanned from zero to $\pi/2$. One can then make a frequency cut at some selected driving frequency of interest, such as the signal frequency ω in the effective linewidth experiment, for example, and obtain a determination of those modes that are degenerate with the drive signal frequency ω . Alternatively, one can arrive at this same determination of degenerate modes by considering a fixed spin wave frequency at $\omega_k = \omega$ and then solving for the dispersion bands in k for $0 < \theta_k < \pi/2$ as a function of H . Both approaches will be used below.

Figures 2 and 3 show spin wave band diagrams that elucidate the manner in which these degenerate spin wave mode populations change with field. All diagrams were obtained for YIG parameters. The graphs in Fig. 2 show traditional plots of spin wave frequency ω_k vs k for two specific fields, as indicated. The dashed line horizontal frequency cuts at $\omega_k/2\pi = 10$ GHz indicate the nominal signal frequency for the current effective linewidth measurements. The single graph in Fig. 3 shows the corresponding plot of wave number k versus the external field H for a spherical sample with the frequency $\omega_k/2\pi$ set to 10 GHz. The field scale is the same as used for Fig. 1. The bands evident in these graphs are formed from dispersion branches that range from wave vectors that are parallel to the static field ($\theta_k = 0$) to wave vectors that are perpendicular to the field ($\theta_k = \pi/2$). The bands are labeled as EML-HI, EMA, EML-LO,

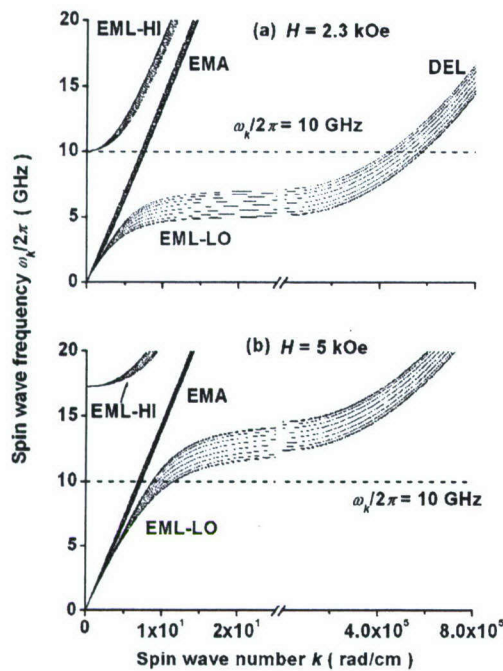


FIG. 2. Graphs (a) and (b) show full infinite medium spin wave band diagrams of the spin wave frequency $\omega_k/2\pi$ as a function of the positive real wave number k for YIG sphere parameters and external static fields of 2.3 and 5 kOe, respectively. The bands of contours correspond to propagation angles (θ_k), relative to the static field, from 0° to 90° . The curves group into three bands, the nearly straight line light line EMA band, the hybrid below-the-light-line EML-LO (low k) to DEL (high k) band, and the above-the-light-line EML-HI band. The graphs also show dashed reference lines at $\omega_k/2\pi = 10$ GHz.

and DEL in all the graphs. The EML-LO and DEL labels actually correspond to the same band for low and high k ranges, as indicated.

It is important to take note of the band label nomenclature in the figures. An important line of reference is the nar-

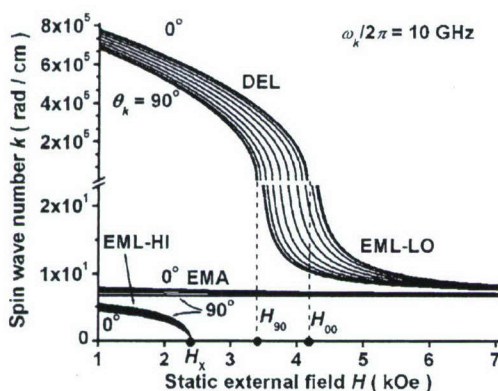


FIG. 3. Infinite medium spin wave band diagram of the positive real spin wave wave number k as a function of the static external field H for YIG sphere parameters and a spin wave frequency $\omega_k/2\pi = 10$ GHz. The bands of contours correspond to propagation angles (θ_k) of 0° to 90° , relative to the static field, as indicated. The curves group into three bands, the nearly flat EMA band, the hybrid DEL (high k and low field) to EML-LO (low k and high field) band, and the low k and low field ($H < H_x$) EML-HI band. The H_x , H_{90} , and H_{00} labels indicate, respectively, the fields at which the EML band limit frequency at $k=0$ sits at 10 GHz and the points in field at which the $\theta_k=90^\circ$ and $\theta_k=0^\circ$ low k limit frequencies for the DEL band sit at 10 GHz.

row straight EMA band in the Fig. 2 graphs and the corresponding nearly horizontal band in Fig. 3. These narrow bands correspond to the light line at $\omega_k = ck/\sqrt{\epsilon_r}$ in the non-magnetic limit. The EML-HI labels identify the above-the-light-line band just above this light line band in the Fig. 2 graphs. The EML-LO labels identify the below-the-light-line band in these graphs. At high k , the EML-HI band converges with the light line, while the EMA-LO band moves farther and farther away and finally evolves into the DEL band. The DEL band is so labeled to denote the dipole-exchange (DE) and Larmor (L) nature of the high k far-from-the-light-line response. The "L" in EML also denotes the precession response as Larmor. The "A" in EMA denotes the anti-Larmor precession associated with the light line band.

The notation here follows that used in Ref. 1, except for the additional "HI" and the "LO" designations that are now invoked to designate the above-the-light-line and the below-the-light-line EMSW bands in Fig. 2. In Ref. 1, only the EML-LO band (as now labeled) was important for the high field effective linewidth. For the low field effective linewidth, it is the EML-HI and DEL bands that play important roles. Note that the different bands flip positions relative to the EMA light line band in going from Fig. 2 to Fig. 3.

The advantage of the Fig. 2 format is that one can see the full spin wave band scheme in reference to the specific slice of modes that are degenerate with the 10 GHz drive frequency for given field values. The $H = H_x = 2.3$ kOe field point for (a) demonstrates the two magnon scattering connections that are relevant to the low field effective linewidth. This is also the particular value for which the EML-HI band converges to the $\omega_k/2\pi = 10$ GHz reference line at $k=0$. The $H = 5$ kOe value for (b) was chosen to show the position of the spin wave bands that are relevant to the high field effective linewidth.

The advantage of the Fig. 3 format is that one can see directly the manner in which the wave numbers for the modes that are degenerate with the 10 GHz drive frequency change with field. The labels H_x , H_{90} , and H_{00} along the field axis show, respectively, the point in field at which the above-the-light-line EMSW band limit frequency at $k=0$ sits at 10 GHz, and the points in field at which the $\theta_k=90^\circ$ and $\theta_k=0^\circ$ low k limit frequencies for the DEL band also sit at 10 GHz. From the dispersion bands in Fig. 3 and the H_x , H_{90} , and H_{00} labels, one can now see why these points in field are identified in Fig. 1.

B. Qualitative two magnon scattering connections

1. Recap of high field effective linewidth origins

As a starting point for the discussion of the low field data, spin waves, and two magnon scattering, it is useful to begin with a brief recap of the high field results from Ref. 1. Turn, therefore, to Fig. 2(b) and the high field regime in Fig. 3. From Fig. 2(b), one sees that for high fields, the main DEL band is shifted well above the $\omega_k/2\pi = 10$ GHz reference line. From Fig. 3, one sees that the available degenerate modes in the high field regime all belong to the EML-LO

band or to the EMA band. It is the EML-LO modes that dominate the effective linewidth in the high field regime.

There are three main points of note for the high field ΔH_{eff} data. First, the decrease in the HFE linewidth with increasing field for the UD and CS materials for the $H > H_{00}^*$ field regime in Fig. 1 is due to the decrease in the density of states for the modes in this EML-LO band. As one moves to higher and higher fields, the 10 GHz cut across the EML-LO band becomes smaller and smaller. The solid curve in Fig. 1 represents a best fit to a function of the form $\Delta H_{\text{eff}} = A \cdot \text{DOS} + \Delta H_b$, where A is a constant scale factor equal to 7540 Oe cm³ MHz, DOS denotes the density of states for the Larmor electromagnetic branch spin waves, and ΔH_b is a constant background linewidth parameter set to 0.35 Oe. The good matchup of the UD data with the solid curve for $H > H_{00}^*$ is convincing evidence that the EML-LO band two magnon scattering is responsible for the HFE linewidth field response. The numerical scale factor A will play a role in the theoretical analysis of the low field ΔH_{eff} results. This scattering to the extremely low k EML-LO band of modes is relatively weak and the effective linewidths are only slightly larger than the background linewidth of 0.35 Oe.

The second point is that the high field ΔH_{eff} extrapolates to near intrinsic linewidth values in the extreme high field limit. The fitted ΔH_b value of 0.35 Oe is close to established values of the 10 GHz linewidth in single crystal YIG.¹¹ These so-called intrinsic linewidths in this range for single crystal YIG are typically associated with various magnon phonon processes other than two magnon scattering. This also means that the anti-Larmor EMA band spin waves make essentially no contribution to the HFE linewidth. Because the EMA band is more or less flat as a function of field, as in Fig. 3, this implies that the EMA band is not important for the LFE linewidth as well.

The third important aspect of the high field response concerns the more rapid rise in the high field ΔH_{eff} for the CS sample as the field drops below H_{00}^* . This effect is due to differences in microstructure and, in particular, the effect of pores. The maximum spherical pore demagnetizing field in the direction opposite to the applied field, just at the top and bottom of the pore, is about $8\pi M_s/3$. This is precisely the separation of the H_{00}^* point from the H_{00} (no asterisk) point at the high field edge of the manifold region. As H drops below H_{00}^* , there are regions in the CS sample that correspond to a local in-manifold bias field and there is a corresponding increase in the effective linewidth. There is a counterpart pseudo-manifold effect at low field that involves H_{90} and H_{90}^* . This effect will be considered shortly.

2. Low field effective linewidth origins

Now consider the low field spin wave band picture in Fig. 2(a) and the low field degenerate mode picture in Fig. 3. The degenerate mode situation for the low field regime is quite different from that at high field. There are three specific changes of note: First, the previously degenerate EML-LO modes are all well below the $\omega_k/2\pi = 10$ GHz frequency cut, as in Fig. 2(a). From the Fig. 3 display, one sees that the

EML-LO modes that dominate the two magnon scattering contribution to the HFE linewidth are completely out of the picture for the LFE linewidth.

Second, the high k DEL modes that were previously found at frequencies well above the signal frequency now actually cross the 10 GHz cut, as in Fig. 2(a). From the Fig. 3 display, one sees that there are degenerate high k DEL modes over the entire low field regime. This means that one can have scattering to these high k DEL modes over the entire low field regime. However, these high k modes have very short wavelengths in the submicron range. For a significant contribution to ΔH_{eff} , the scattering to such modes will invoke considerations of grain boundaries and not simply the micron sized grains of the polycrystal. On the other hand, the large density of states that one finds at high k will promote strong scattering, even if the actual coupling is small. These points will be considered in more detail shortly.

Third, for the particular choice of field at $H = H_X$ for graph (a) of Fig. 2, one can see that the EML-HI band is touching the 10 GHz line just at $k=0$. If the field is dropped further, to some value below H_X , the EML-HI band will drop even more in frequency and the 10 GHz cut will then include modes for this band. Figure 3 shows this explicitly. The changes in the low field ΔH_{eff} versus field response at $H = H_X$ in Fig. 1 for both the UD and the CS samples may be attributed to the vanishing DOS component at 10 GHz for the EML-HI band for $H > H_X$ and the appearance of an EML-HI DOS component for $H < H_X$. Any change in the actual scattering, of course, will involve modes with low wave numbers and extremely large wavelengths. These are the same type of modes that are now known to play an important role in the high field effective linewidth, except that the EML-HI modes now replace the EML-LO modes and there is now the additional effect of a field cut-off effect for $H > H_X$.

Turn now to specific mode connections from Figs. 2(a) and 3 to the low field effective linewidth. First consider the two general points from Sec. III the larger ΔH_{eff} at low field, relative to high field, and the interchange in the relative values of the effective linewidths for the UD and CS samples. One can now see that the basis for a larger ΔH_{eff} in the low field regime, relative to high field, is that there are simply more degenerate modes. In the low field regime, one always has degenerate DEL band modes. The high k nature of these modes generally means a larger density of states.

The high k DEL mode scattering is also the key to the interchange of the relative ΔH_{eff} values, with those for the UD sample now greater than those for the CS samples. One can see from Fig. 3 that the degenerate DEL modes have k values in the 10^5 rad/cm range, with corresponding wavelengths well into the submicron range. As already noted, scattering to such short wavelength modes will be connected more closely with grain boundaries, rather than with grains and pores, and this will favor the relatively smaller grain UD sample. The smaller grain size for the UD sample means a larger net grain boundary area and more scattering, relative to the high k scattering for the CS sample. Simple geometric arguments give a grain boundary area that scales with the grain size a as $1/a$. This means that the UD sample, with

$a \approx 8 \mu\text{m}$, will have a little more than double the grain boundary area of the CS sample with $a \approx 20 \mu\text{m}$. It is reasonable, therefore, to see a higher ΔH_{eff} for the UD sample in the low field regime.

The details of the low field ΔH_{eff} vs H dependences demonstrated in Sec. III can also be placed into a clear spin wave perspective, based on the diagrams in Figs. 2 and 3. The role of the H_X field point is clear from both figures. The changes in the ΔH_{eff} vs H responses for both data sets at $H = H_X$ are clearly related to the onset of mode degeneracy for the EML-HI modes at this field. The more rapid rise in the ΔH_{eff} for the CS sample, relative to that for the UD sample, for $H > H_X$ must be related to the different interplay between the coupling and the density of states for these different microstructures.

The apparent crossover in the low field ΔH_{eff} at $H = H_{90}^*$ and the larger CS ΔH_{eff} as one moves into the low field pseudo-manifold region for $H > H_{90}^*$ are consistent with the similar effect in the high field regime for $H < H_{90}^*$. Here, however, one must consider the maximum value of the pore demagnetizing field that is parallel to the static field. For a spherical pore, this maximum demagnetizing field occurs at the sides of the pore and is equal to $4\pi M_s/3$. The field point at $H = H_{90}^*$ is shifted down from H_{90} by this amount. A close examination of the low field data in Fig. 1 shows, moreover, that the UD and the CS data points appear to cross at precisely this point in field. The rise in ΔH_{eff} for both samples as the field is increased is already quite rapid in this local region, and it is difficult to tell if there is an actual increase in the slope of the response as one would expect from an onset of pseudo-in-manifold scattering for $H > H_{90}^*$.

Finally, there are the quite different ΔH_{eff} responses for $H < H_X$. This is the region where the EML-HI modes come into play. Given the fact that the EML-LO modes give rise to the same ΔH_{eff} vs H responses for $H > H_{90}^*$ in the high field regime, while the EML-HI modes give rise to different responses for the UD and the CS samples in the low field regime with $H < H_X$, one can surmise that some different aspects of the low k scattering must be coming into play. It may be noteworthy that the two linewidths are roughly equal for an external field slightly above 1 kOe. This is about the point at which the spherical YIG samples will start to demagnetize. Demagnetization will tend to average out polarization effects.

C. Grain boundary scattering and quantitative connections with low field effective linewidth

This section considers a theory of GBS and connections with the present data. The full theory will be published separately. As already noted, the relevant k values are in the 10^5 rad/cm range and one needs submicron inhomogeneities to provide a source for the two magnon coupling. The grains in the UD and CS YIG materials are in the $5\text{--}20 \mu\text{m}$ range. The main candidate for high k scattering, therefore, is in grain boundaries and related defects.

Formally, one may write the two magnon relaxation rate η_{TM} as an integral over the available \mathbf{k} states at $\omega_k = \omega$ that takes into account the density of states and the coupling to

the modes. One then obtains the effective linewidth as $\Delta H_{\text{eff}} = 2\eta_{\text{TM}}/|\gamma|$. The η_{TM} integral can be written in the form

$$\eta_{\text{TM}} = \frac{\omega_M^2}{4\pi^2} \int d\mathbf{k} C(\mathbf{k}) \Lambda(\omega, \mathbf{k}) \delta(\omega_k - \omega). \quad (4)$$

The ω_M parameter is equal to $|\gamma|4\pi M_s$. The $\delta(\omega_k - \omega)$ function serves to constrain the considered spin wave modes to those for the particular ω_k band of interest and those particular modes that are degenerate with the signal frequency. The delta function integral alone corresponds to the density of states. The coupling factor $C(\mathbf{k})$ determines the strength of the coupling between the uniform mode and the spin waves due to the grain boundaries. The mode polarization factor $\Lambda(\omega, \mathbf{k})$ takes the ellipticity of the spin wave modes into account. The paragraphs below outline the essential physics of the low field scattering, provide recipes for actual evaluations, and present fits to the data based on the theory.

Consider first the basic variation in the DOS for the degenerate modes as a function of field. Density of states is a basic concept in solid state physics. The starting assumption is that the allowed plane wave modes are uniformly distributed in \mathbf{k} space. It is then a matter of geometry and the details of the given dispersion connections to obtain the number of modes $dn(\omega_k)$ per unit volume for a given slice of frequency space from ω_k to $\omega_k + d\omega_k$. The relation $dn(\omega_k) = g(\omega_k)d\omega_k$ then serves as a definition of a DOS function $g(\omega_k)$. For the multiband spin wave situation at hand, $g(\omega_k)$ becomes the field dependent $g(\omega_k, H)$ DOS function for the total density of states for all of the modes degenerate with a given ω_k . This is because the k solutions in Eq. (3) also depend on H . For a given band of interest, one obtains a working equation of the form,

$$g(\omega, H) = \frac{1}{2\pi^2} \int_0^{\pi/2} k^2(\omega, \theta_k, H) \frac{\partial k(\omega, \theta_k, H)}{\partial \omega} \sin \theta_k d\theta_k. \quad (5)$$

The density of states weighting function is embodied in the integral of Eq. (4) through the $\delta(\omega_k - \omega)$ constraint. The density of states plays an important role in two magnon scattering.

Note that the integral in Eq. (5) is over the spin wave propagation angle θ_k only. This corresponds to a vertical line cut in Fig. 3 at a fixed field across the available modes. For the two magnon scattering problem, one solves Eq. (3) for the positive real $k(\omega_k, \theta_k, H)$ roots for the DEL, EML-LO, and EML-HI bands, obtains the derivative functions needed for Eq. (5), and then evaluates the integrals for $\omega_k = \omega$. These evaluations are done numerically to obtain $g(\omega, H)$ as a function of H . The dispersion relation in Eq. (3) connects k to θ_k , and one can reduce the k -space integral to the form given above. For specific ω and H values, $g(\omega, H)$ can be easily evaluated by numerical methods for any known dispersion connection.

Figure 4 shows calculated density of states curves for $g(\omega, H)$ as a function of the static external field H at $\omega/2\pi = 10 \text{ GHz}$ for the DEL, DEL-LO, and EML-HI bands, as indicated. The curves were obtained for YIG parameters. Curves for the EMA band are excluded. The DOS curves in

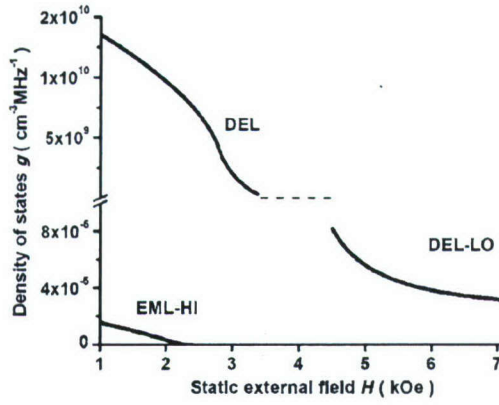


FIG. 4. Integrated 10 GHz density of degenerate states g as a function of static external field H for the DEL, EML-HI, and EML-LO spin wave bands, as indicated. The curves were obtained for YIG parameters and sphere shaped samples.

Fig. 4 quantify many of the basic features mentioned in the previous sections. For the low field DEL band of primary interest here, the $g(\omega, H)$ values are rather large, on the order of $10^{10} - 10^{11} \text{ cm}^{-3} \text{ MHz}^{-1}$. These large values are due to the large wave numbers for the dipole exchange spin waves, on the order of 10^5 rad/cm , and the corresponding large volume of k space. The density of states remains relatively high as one moves to the bulk manifold region and the horizontal dashed transition line from DEL to EML-LO modes in Fig. 3. This is because high k as well as low k spin waves are available. For the EML-LO band that is present only at high field, the wave numbers are small and $g(\omega, H)$ is also small, typically on the order of $10^{-5} \text{ cm}^{-3} \text{ MHz}^{-1}$. This matches the situation considered in Ref. 1. The EML-HI band only comes in for fields below $H = H_X$. The density of states for these modes is even smaller, mainly due to the extremely low values of k for this above-the-light-line spin wave band.

Turn now to the coupling and polarization functions in Eq. (4). The GBS theory is based on a simple model of partial pinning at the grain boundaries and the assumption of random grains with an average grain size a . Fourier transforms, correlations, and statistical averaging are used to obtain a $C(\mathbf{k})$ coupling factor that may be written as

$$C(\mathbf{k}) = C(k) = \frac{6\pi k^2 \ell_{gb}^2 a^3}{(1 + k^2 a^2)^2}, \quad (6)$$

where ℓ_{gb} is an effective grain boundary thickness parameter. Much of the formal analysis follows from the approach of Schlömann for the isotropic anisotropy scattering.^{12,13} That is, there is no dependence on the direction of \mathbf{k} .

The ℓ_{gb} parameter derives from a surface or interface anisotropy energy density at the grain boundary and is essentially the ratio of this energy density to the magnetostatic self-energy $2\pi M_s^2$.¹⁴ This interaction serves to provide a partial pinning of dynamic magnetization at the grain boundary. As shown below, if the measured LFE linewidths are taken to originate from a GBS process, one obtains ℓ_{gb} values in the nanometer range.¹⁵ These are reasonable values for grain boundaries in dense ferrite materials. The corresponding surface anisotropy energies are on the 0.1 erg/cm^2 range. This is also reasonable for a surface or interface anisotropy. As

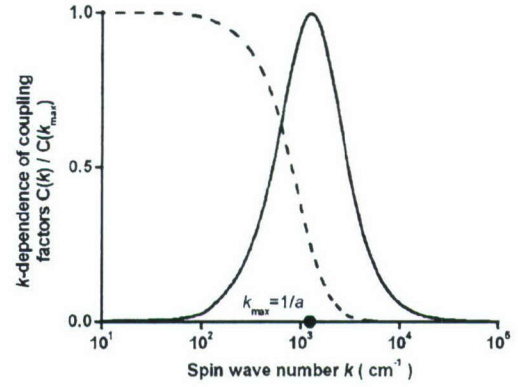


FIG. 5. The solid curve shows the scaled grain boundary scattering coupling factor $C(k)/C(k_{\max})$ as a function of wave number k , where $k_{\max} = 1/a$ marks the peak position. Here, a is the average grain size. The dashed curve shows the scaled coupling factor for isotropic grain scattering due to anisotropy. The curves are for $a = 8 \mu\text{m}$.

one might expect, the fact that ℓ_{gb} is fairly small means that the coupling factor is also small. The sizable effective linewidths due to low field grain boundary scattering derive from the high density of states for the DEL modes in the low field regime. Note that this type of GBS model is not valid for porous materials. Scattering based on an interface anisotropy is not valid when there are voids between the grains.

Figure 5 shows a normalized plot of $C(k)/C_{\max}(k)$ from Eq. (6) as a function of k . The grain size a was set at $8 \mu\text{m}$, the nominal grain size for the UD YIG material. Note that the horizontal k scale is logarithmic. The coupling factor is a maximum at $k_{\max} = 1/a$ and it exhibits a rather broad and nonsymmetric-peak-type response. On a linear k scale, the half maximum points in k occur at $0.414/a$ and $2.414/a$, for a half width of $2/a$. The dashed curve in Fig. 5 shows the coupling factor that one would expect for grain scattering. The grain scattering coupling is essentially constant for $k < k_{\max}$ and falls to zero fairly rapidly for $k > k_{\max}$. One can see that grain boundary scattering is much different from grain scattering.

As noted, the remaining $\Lambda(\omega, \mathbf{k})$ factor in Eq. (4) is related to the change in the spin wave ellipticity as one ranges over the allowed θ_k values for the band. The $\Lambda(\omega, \mathbf{k})$ function may be written as

$$\Lambda(\omega, \mathbf{k}) = \frac{1}{2\omega} \left[|\gamma| H_i + |\gamma| D k^2 + \omega + \frac{\omega_M \sin^2 \theta_k}{2} \right]. \quad (7)$$

At $\omega/2\pi = 10 \text{ GHz}$ and $H = 2 \text{ kOe}$ for sphere shaped YIG samples, $\Lambda(\omega, \mathbf{k})$ will range from about 0.68 at $\theta_k = 0$ to 0.82 at $\theta_k = 90^\circ$. The change with field from $H = 1 \text{ kOe}$ to $H = 2 \text{ kOe}$ amounts to about 20%. This causes a small ellipticity contribution to the field dependence of η_{TM} in Eq. (4).

Figure 6 shows results on the computed GBS contribution to the low field effective linewidth as a function of field based on the prescription given above. The solid circle data points show the low field ΔH_{eff} data for the UD YIG sample from Fig. 3. The graph extends from the low field 1 kOe limit used for Fig. 3 up to the edge of the manifold region at H_{90} . The calculations include only the GBS scattering for the DEL band of modes. The effective grain boundary thickness

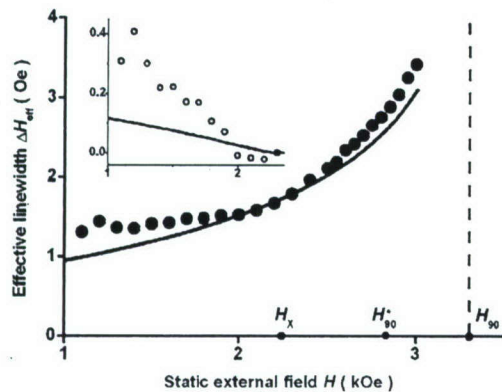


FIG. 6. Effective linewidth ΔH_{eff} vs static external field H for a spherical yttrium iron garnet (YIG) sample. In the main graph, the solid circles show the data from Fig. 1 for the ultradense (UD) YIG sample and the solid curve shows the computed linewidth due to grain boundary scattering. The dashed vertical line indicates the low field edge of the low wave number DEL spin wave manifold. The H_X and the H_{90} field points are the same as in Fig. 1. The open circles in the inset show the difference values for the data in the main graph for $H < H_X$, relative to the solid line. The solid curve shows the expected contribution to the LFE linewidth from EML-HI scattering, based on the scaling from the high field results.

parameter ℓ_{gb} was set at 9.5 nm and the average grain size a was set at the nominal value of 8 μm for the UD sample. This particular choice for ℓ_{gb} was made by fine tuning the calculated curve to give the match to the data as shown. As noted above, an ℓ_{gb} value of 10 nm or so is reasonable for dense polycrystalline ferrites. The $|\gamma|$ and $4\pi M_s$ values were the same as given above for YIG. The curve includes no provision for an offset residual linewidth.

The open circle points in the inset graph in Fig. 6 show the difference between the measured linewidth results for $H < H_X$ and the GBS theoretical values. The solid curve in the inset is based on the DOS for the EML-HI band of modes and the numerical scaling factor A obtained from the fit of the EML-LO DOS response to the HFE data. The curve shows only the expected two magnon scattering linewidth for the EML-HI modes based on this scaling. No other contributions are included.

One can see from the main graph in Fig. 6 that the GBS mechanism gives a reasonable semiquantitative match to the LFE linewidth data over the applicable high k scattering region in the field region between H_X and H_{90} . The term “semiquantitative” is used because it was not possible to obtain a good fit when a background level linewidth was added to the GBS response. This indicates that further refinements of the GBS model are needed to include a grain size distribution and possibly other factors. In spite of these problems, the matchup in the overall linewidth values for $H_X < H < H_{90}$ and the reasonable values of the GBS model parameters support the thesis of two magnon scattering from the driven uniform mode to DEL band spin waves as the origin of this low field response.

D. The LFE linewidth below $H = H_X$ and EML-HI scattering

As already noted in the previous sections, the upward deviation of the data from the theoretical curve for $H < H_X$

can be attributed to the appearance of additional low k scattering to the EML-HI modes at low field. The data in Fig. 6 show that the amount of deviation in the measured ΔH_{eff} from the GBS curve increases from near zero to more than several tenths of an oersted as H drops below H_X . At first glance, one might take this full deviation as a measure of the change in the density of states for the EML-HI modes with field and solid evidence for a significant two magnon EML-HI scattering effect.

The results in the inset of Fig. 6, however, indicate that this may not be the whole story. The solid curve shown in the inset shows the expected amount of low field effective linewidth from scattering to the EML-HI modes based on the scale parameter A obtained from the high field fit shown in Fig. 1. One can see that the predicted increase in the two magnon EML-HI scattering based effective linewidth falls well short of the observed increase. As a caveat, one also has to realize that all of these linewidth values are extremely small, on the order of or smaller than even the expected intrinsic linewidths.

One possible explanation for this discrepancy is that a different DOS scaling parameter for the low field EML-HI scattering is needed, relative to the high field EML-LO A value. At the few tenths of an oersted level, the differences in the ellipticity for these low field and high field spin wave branches, among other things, could be substantial and require a different scaling.

There are other options as well. It was more than four decades ago that Hartwig *et al.*¹⁶ noted a peculiar subthreshold effect for parallel pumping in YIG single crystal spheres. These authors observed a rapid increase in the longitudinal microwave permeability loss component just as the applied field drops below the H_X point. Follow-up theory by Joseph and Schlömann¹⁷ gave reasonable support to the presence of a subthreshold longitudinal susceptibility loss component that comes into play due to the in-manifold low k spin waves at one-half the pump frequency, just as the field drops below H_X . If there is indeed such a subthreshold longitudinal loss component, there could also be a subthreshold transverse loss component. Further work on the LFE linewidth for large single crystal YIG spheres is needed to address these issues.

V. SUMMARY

The above sections have described a refined method for precision measurement of the out-of-manifold effective linewidth in bulk ferrite materials. Specific measurements are reported for two materials, ultradense polycrystalline yttrium iron garnet produced by hot isostatic pressing and conventional sintered YIG with a moderate porosity. The data and corresponding analysis give insight into the origins of microwave loss in ferrites at low as well as high fields. In parallel with the high field results in Ref. 1, the low field effective linewidth is shown to be due to scattering to electromagnetic spin waves and pseudo-in-manifold spin waves.

The LFE linewidth, however, is attributed to two extra sources of scattering. From the low field edge of the low k spin wave band down to a cut-off field H_X point for the appearance of low wave number EML-HI modes, the effec-

tive linewidth is consistent with a grain boundary scattering model that couples the uniform mode to very high k DEL spin waves. Fits based on a theory of grain boundary scattering show semiquantitative agreement with the data. Problems for a complete quantitative agreement remain in that the match to the data is not possible if one includes any reasonable level of background intrinsic loss in the model.

For fields below H_X , the data show clear evidence for an additional low k two magnon scattering contribution from the EML-HI modes. However, a computed EML-HI two magnon scattering response, with a calibration based on the high field results, falls somewhat short of the measured values. Possible problems here include calibration issues and the possibility of an additional subthreshold nonlinear loss effect.

ACKNOWLEDGMENTS

This work was supported in part by the United States Office of Naval Research, Grant No. N00014-06-1-0889, and the U.S. Army Research Office, Grant No. W911NF-04-1-0247. The ultradense hipped YIG materials were prepared by G. M. Argentina and Dr. H. J. Van Hook. The conventionally sintered G113 YIG materials were provided by Trans Tech,

Inc., Adamstown, Maryland. Kevin R. Smith and Dr. Steven N. Stitzer are gratefully acknowledged for careful reviews of the paper.

- ¹N. Mo, Y. Song, and C. E. Patton, J. Appl. Phys. **97**, 093901 (2005).
- ²C. E. Patton, J. Appl. Phys. **41**, 1355 (1970).
- ³T. Kohane and E. Schlömann, J. Appl. Phys. **39**, 720 (1968).
- ⁴C. E. Patton, Phys. Rev. **179**, 352 (1969).
- ⁵Q. H. F. Vreken, J. Appl. Phys. **40**, 1849 (1969).
- ⁶A. V. Nazarov, D. Ménard, J. J. Green, and C. E. Patton, J. Appl. Phys. **95**, 7227 (2003).
- ⁷J. J. Green and T. Kohane, Semicond. Prod. Solid State Technol. **7**, 46 (1964).
- ⁸J. D. Jackson, *Classical Electrodynamics* (Wiley, New York, 1998).
- ⁹U. Hoeppe, International Conference on Ferrites ICF9, San Francisco, August 2004 (unpublished).
- ¹⁰B. Lax and K. J. Button, *Microwave Ferrites and Ferrimagnetics* (McGraw-Hill, New York, 1962).
- ¹¹M. Sparks, *Ferromagnetic-Relaxation Theory* (McGraw-Hill, New York, 1964).
- ¹²E. Schlömann, IEEE Trans. Magn. **1**, 75 (1970).
- ¹³E. Schlömann, Phys. Rev. **182**, 632 (1969).
- ¹⁴R. F. Soohoo, *Theory and Applications of Ferrites* (Prentice-Hall, New Jersey, 1960).
- ¹⁵J. T. Yu, R. A. Turk, and P. E. Wigen, Phys. Rev. B **11**, 420 (1975).
- ¹⁶C. P. Hartwig, J. J. Green, R. I. Joseph, and E. Schlömann, J. Appl. Phys. **36**, 1265 (1965).
- ¹⁷R. I. Joseph and E. Schlömann, J. Appl. Phys. **38**, 1915 (1967).

Experimental Observation of Fermi-Pasta-Ulam Recurrence in a Nonlinear Feedback Ring System

Mingzhong Wu and Carl E. Patton

Department of Physics, Colorado State University, Fort Collins, Colorado 80523, USA

(Received 3 October 2006; published 22 January 2007)

Fermi-Pasta-Ulam recurrence through soliton dynamics has been realized. The experiment used a magnetic film strip-based active feedback ring. At some ring gain level, a wide spin wave pulse is self-generated in the ring. As the pulse circulates, it separates into two envelope solitons with different speeds. When the fast soliton catches up and collides with the slow soliton, the initial wide pulse is perfectly reconstructed. The repetition of this process leads to periodic recurrences of the initial pulse.

DOI: 10.1103/PhysRevLett.98.047202

PACS numbers: 75.30.Ds, 05.45.Yv, 76.50.+g

The unexpected recurrence of a nonlinear system back to an initial state was first discovered by Fermi, Pasta, and Ulam (FPU) in 1955 through the simulation of a one-dimensional lattice [1]. This FPU recurrence paradox was initially characterized by Fermi as a “little discovery.” This discovery, in fact, marked a true sea change in modern science [2]. On the one hand, it ushered in the age of computational science through the introduction of computer simulation for the first time. At the same time, it marked the birth of nonlinear science. It led to both the discovery of solitons and the widespread awareness of deterministic chaos.

The FPU recurrence paradox remained a complete mystery until Zabusky and Kruskal (ZK) discovered solitons in 1965 [3]. In an attempt to solve the FPU paradox, Zabusky and Kruskal reduced the FPU problem to the Korteweg-de Vries (KdV) equation based on a so-called continuum approximation and numerically discovered solitons. In terms of soliton dynamics, they explained that with time, a large-amplitude periodic wave described by the KdV equation can break up into a family of solitons with different speeds. When the fast solitons catch up and collide with the slow solitons, there is a reconstruction of the initial periodic wave.

The ZK 1965 work did even more than provide the first solution to the FPU paradox and mark the birth of soliton science. It also showed, at least theoretically, that one can actually realize FPU recurrence through the excitation of a large-amplitude periodic wave in a soliton-supporting nonlinear system. Attempts to realize such a FPU recurrence experimentally have been made for periodic waves in electrical networks [4], plasmas [5], and magnetic films [6]. Here, the breakup of the initial pulses into solitons and the subsequent overtake and collision of these solitons were observed. Bona fide recurrence, however, was not observed. First, the recurrence to the initial state was not exact because of energy decay. In addition, the energy decay also precluded the realization of more than a single recurrence. It is to be emphasized that the main reason for these failures lies in the dissipation present in the systems.

This Letter reports on the realization of an exact and periodic FPU type of recurrence. This has been achieved through the novel use of feedback to circumvent the dissipation problem. Specifically, one starts with a nonlinear pulse in a soliton-supporting one-dimensional medium. One then feeds the amplified output signal back to the input to produce a soliton-supporting “conservative” nonlinear ring system. Here, the conservative does not mean that the ring system is free of dissipation. Rather, it means that the wave dissipation is compensated by the active feedback. A circulating pulse in such a ring is topologically equivalent to a periodic wave train in a one-dimensional conservative system as studied in the ZK work [3]. As such, the nonlinear pulse experiment in such a ring is expected to show a true dissipation free recurrence response.

The experiment used a magnetic film strip-based active feedback ring. The magnetic film strip served as a nonlinear dispersive medium for the propagation of spin waves [7,8]. The propagation geometry was chosen to give an attractive or self-focusing nonlinearity that supports the formation of bright spin wave envelope solitons [9]. The active feedback allowed for the self-generation of a wide spin wave pulse. As the pulse circulates in the ring, it separates into two envelope solitons with different speeds. After many circulations, the fast soliton catches up and collides with the slow soliton and the initial wide pulse is perfectly reconstructed. The repetition of this soliton process leads to periodic recurrences of the initial pulse. Remarkably, the splitting of the initial pulse into separate solitons and the recombination of these solitons to reform the initial pulse over and over again is in nearly perfect agreement with the ZK prediction.

Figure 1 shows the experimental setup. The magnetic yttrium iron garnet (YIG) film strip is magnetized to saturation by a static magnetic field parallel to the length of the strip. This configuration allows for the propagation of backward volume spin waves [7–9] and the formation of bright spin wave envelope solitons [9]. Two microstrip transducers are placed over the YIG strip for the excitation

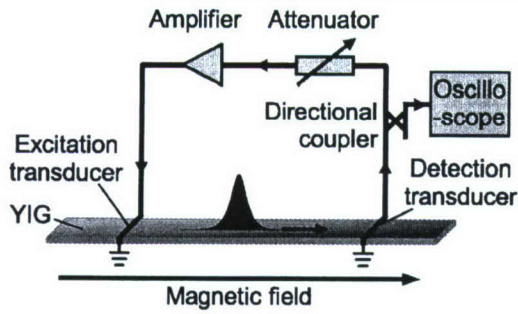


FIG. 1. Diagram of YIG strip-based active feedback ring system.

and detection of spin waves. The detection transducer is connected to the excitation transducer through a linear broadband microwave amplifier to form an active feedback ring. The ring gain is controlled through an adjustable microwave attenuator. The ring signal is sampled through a directional coupler and is analyzed with a broadband microwave oscilloscope. For the data shown below, the YIG film strip was 10.8 mm thick, 2 mm wide, and 37 mm long. The magnetic field was held at 970 Oe. The microstrip transducers were 50 mm wide and 2 mm long. The separation between the transducers was set to be 5.7 mm.

The feedback ring system can have a number of resonance eigenmodes that exhibit low decay rates. For a magnetic film feedback ring, the eigenmode frequencies are determined by the phase condition $k(\omega)l + \phi_0 = 2\pi n$ where k is the spin wave wave number, ω is the spin wave frequency, l is the transducer separation, ϕ_0 is the phase shift introduced by the feedback circuit, and n is an integer. The eigenmode frequencies and their spacing can be adjusted through a change in the $k(\omega)$ dispersion function and/or the transducer separation l . The dispersion function, in turn, can be controlled through the film parameters and the magnetic field [7]. At a low ring gain G , all of these eigenmodes experience an overall net loss and there is no spontaneous signal in the ring. If the ring gain is increased to a certain threshold level, here taken as $G = 0$, the eigenmode with the lowest decay rate will start to self-generate and one will obtain a continuous wave response at this eigenmode frequency. A further increase in the ring gain results in the generation of additional modes through a four-wave process. In the time domain, this corresponds to the formation of a spin wave pulse that circulates in the ring. The circulation period is given by the sum of the spin wave propagation time l/v_g in the film, where v_g is the group velocity, and the signal propagation time t_0 in the feedback circuit. Typically, the time l/v_g is on the order of 100 ns, while the time t_0 amounts to a few nanoseconds at most [10,11].

The power of the circulating spin wave pulse increases with the ring gain. At some threshold power for which the nonlinearity is strong enough for the nonlinearity-induced pulse narrowing to balance the dispersion-induced pulse

broadening, the pulse evolves into an envelope soliton [12,13]. With a further increase in the ring gain, the pulse power becomes too high to maintain a single soliton state and the pulse breaks up into two solitons with different speeds. The slow overtake and subsequent collision of these two solitons produce the FPU recurrence that is demonstrated below.

Figure 2 shows output signals for three different ring gain levels. Graphs (a), (b), and (c) show power versus time profiles measured at $G = 0.2, 0.3$, and 0.6 dB, respectively. For easy comparison, the three signal traces are shown with the same power and time scales. Graph (d) shows expanded displays of the two pulses at 60 ns and 2920 ns from (c). Graph (e) shows the carrier waves for the two pulses in (d). The curve shows a sine function fit to the data.

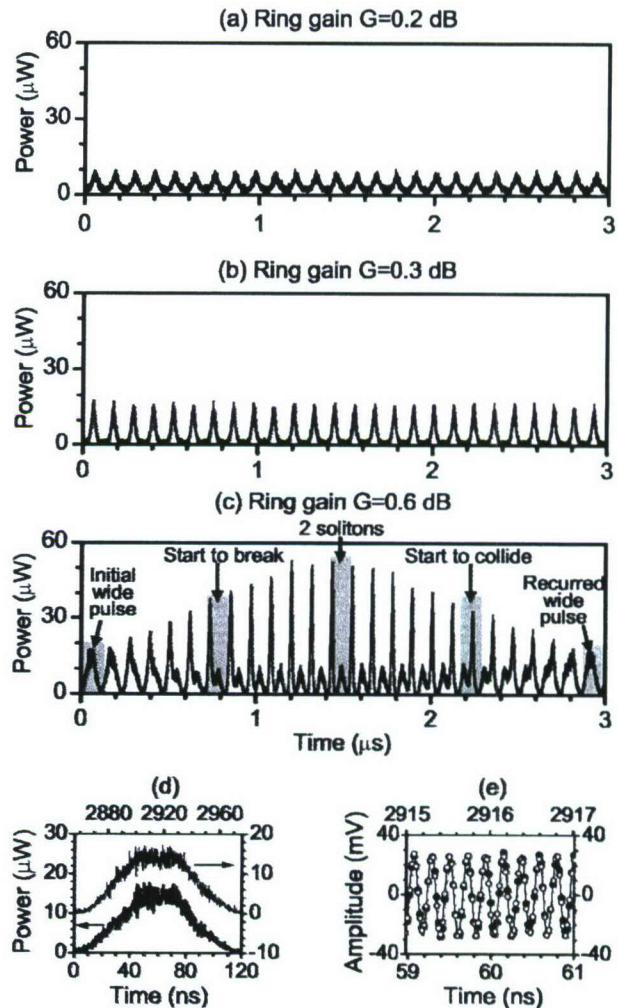


FIG. 2. Graphs (a), (b), and (c) show the power versus time profiles measured at ring gains of $G = 0.2$ dB, 0.3 dB, and 0.6 dB, respectively. Graph (d) shows the two pulses at 60 and 2920 ns from (c) on expanded scales. Graph (e) shows the carrier waves for the two pulses in (d). The curve shows a sine function fit.

The data in Fig. 2 demonstrate the realization of the FPU recurrence. In (a), one has a uniform pulse train that corresponds to a stable circulation of a single spin wave pulse in the ring. With an increase in the ring gain to 0.3 dB, as in (b), the amplitude of the pulse increases while the width of the pulse decreases. Indeed, the half-power width decreases from about 33 ns for $G = 0.2$ dB to about 24 ns for $G = 0.3$ dB. Such a self-narrowing effect results from attractive nonlinearity, and the circulating pulse now corresponds to a spin wave envelope soliton. The soliton nature of this pulse is confirmed by the hyperbolic secant shape [12,13] and a constant phase profile [14].

With a further increase in the ring gain to 0.6 dB, the pulse loses its soliton nature and evolves into a wide pulse. This corresponds to the leftmost pulse in (c). Its amplitude is about the same as for the soliton in (b). Its width of about 60 ns, however, is significantly larger than the width of the soliton in (b). This wide pulse is not stable [15,16], and it gradually breaks up into two solitons after several round trips. This breakup is evident from the left half of the trace in (c). Note that the leading soliton is taller than the initial wide pulse, while the trailing soliton is shorter. Here too, the soliton nature of these pulses is evident from their hyperbolic secant shapes and constant phase profiles, as well as additional soliton signatures considered below. One critical point is that these solitons have amplitude-dependent speeds; the tall soliton travels faster than the short soliton. Because of this property, the tall soliton catches up and collides with the short soliton after several round trips. This is evident from the right part of the trace in (c). This process leads, in turn, to a perfect recurrence through a matchup of the left and right most pulses in (c). This perfect matchup is made even clearer from the superimposed responses in (d). The carriers also match. This is evident in (e) where both carrier waves are nicely fitted by one and the same sine function.

These results provide a perfect demonstration of FPU recurrence. One key for such a realization lies in the amplitude-dependent speed property of the solitons, just as predicted by Zabusky and Kruskal [3]. It is this amplitude-dependent speed that makes the slow overtake possible. A second key element of the process is the active nature of the ring. Without the amplified feedback, pulse decay would dominate the response, and the recurred pulse, if any, would have a much lower amplitude. It is this ring feature that makes the perfect recurrence possible.

Since solitons can survive collisions with other solitons [3,12], one would naturally expect that the repetition of the soliton collision process described above and the periodic recurrences to the initial pulse could occur for a very long time. Figure 3 shows that such an extended recurrence can actually be realized. Graph (a) shows the ring signal over a relatively long period of 10 μ s. The experimental conditions are the same as for the data in Fig. 2(c). Graphs (b) and (c) show plots of the corresponding tall and short soliton peak times versus the number of round trips, respectively. The circles, triangles, and squares show the data

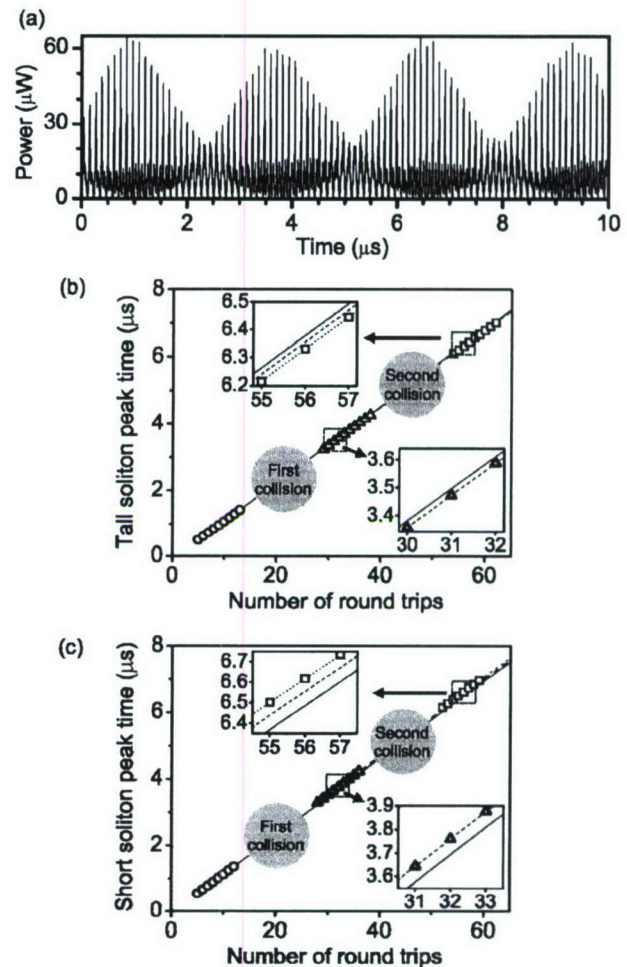


FIG. 3. Graph (a) shows the ring signal measured at a ring gain of 0.6 dB. Graphs (b) and (c) show the tall and short soliton peak times versus the number of round trips, respectively. The circles, triangles, and squares are for the solitons before the first collision, after the first collision, and after the second collision, respectively. The solid, dash, and dot lines show linear fits to the circle, triangle, and square data, respectively. The insets show selected segments of the data and the fits on expanded scales, as indicated.

for the solitons before the first collision, after the first collision, and after the second collision, respectively. The solid, dashed, and dotted lines are linear fits to the circle, triangle, and square data, respectively. The insets show selected segments of the data and the fits on expanded scales, as indicated.

The data in Fig. 3(a) show the perfect periodic nature of the recurrence. Because response is periodic, the definition of the initial state is somewhat arbitrary. No matter which initial state is chosen, however, one always sees multiple recurrences to the initial state. As an example, if one takes the pulse at 0 ns as an initial state, one observes three full recurrence periods. Such an extended periodic response is the signature of FPU recurrence. As above, the key to this realization lies in the active feedback. It is believed that the recurrences to the initial pulse are exact. Any small differences between the initial and the recurred pulses may be

attributed to the fact that the collisions do not always occur at the exact same positions, while the signals are always recorded at one and the same position.

Figure 3 also shows a number of basic soliton features. First, graph (a) demonstrates the ability of the solitons to survive collisions. It is this collision-survival property that allows for the repetitive collisions and the multiple recurrences observed in the first place. Second, graphs (b) and (c) show that the collisions also produce phase shifts in the peak time versus round trip number trajectories for a given soliton. For the tall soliton in (b), a collision causes the peak time to advance. For the short soliton in (c), in contrast, a collision causes a delay. Without these phase shifts, the recurrence period would be longer than that shown in (a). One can also see that the trajectories in (b) and (c) are perfectly straight. This demonstrates another key feature of solitons, namely, that they travel with a constant speed. In addition, one can see that all of the fitting lines in the insets are parallel to each other. This means that the solitons always recover their original speeds after collision.

The above results demonstrate an exact and periodic FPU recurrence. The results also provide direct experimental evidence for the ZK FPU recurrence interpretation in terms of soliton dynamics. Recall that the ZK interpretation was specifically for the class of nonlinear systems described by the KdV equation [3]. The YIG film based nonlinear ring here, however, does not constitute a KdV system. In this sense, the results also provide direct evidence for the universality of the ZK interpretation for a general nonlinear system. It is important to note that the present recurrence is realized through the overtaking collision of two solitons, while the recurrence dynamics in the ZK model involves as many as eight solitons. In other words, the present recurrence represents a simple but revealing case of the ZK interpretation. The experimental realization of the more aesthetic FPU recurrence that takes place through multiple collisions between a large number of solitons remains as a fascinating and challenging subject in nonlinear science.

In line with the above, the present results demonstrate that one can realize FPU recurrence in any practical soliton-supporting systems as long as the dissipation is compensated. This practical realization of FPU recurrence may well lead to novel methods for secure communications, among other application. One could, for example, (i) code information into the solitons, (ii) use a nonlinear ring system [11,17,18] to combine these solitons into a single pulse, (iii) transfer the combined pulse in a linear communication channel, and then (iv) use a secondary but identical nonlinear ring system to provide for the breakup of the pulse into solitons. One could code an information signal into the number and/or order of solitons. One could also use the soliton modulation schemes proposed by Suzuki *et al.* [19,20].

It is useful to note that the ZK interpretation is not the only solution to the FPU recurrence paradox [21,22]. The

FPU paradox could also be interpreted, for example, in terms of modulational instability (MI) [22,23]. Indeed, MI-associated recurrence has also been experimentally observed in deep water [24] and optical fibers [25].

This work was supported in part by the U.S. Army Research Office, No. W911NF-04-1-0247, and the Office of Naval Research (U.S.A.), No. N00014-06-1-0889. Professors B. A. Kalinikos of the St. Petersburg Electrotechnical University and L. D. Carr of the Colorado School of Mines are acknowledged for helpful comments.

-
- [1] E. Fermi, J. Pasta, and S. Ulam, *Studies of Nonlinear Problems* (Los Alamos Scientific Laboratory Report No. LA-1940, Los Alamos, New Mexico, 1955).
 - [2] D. K. Campbell, P. Rosenau, and G. M. Zaslavsky, *Chaos* **15**, 015101 (2005).
 - [3] N. J. Zabusky and M. D. Kruskal, *Phys. Rev. Lett.* **15**, 240 (1965).
 - [4] R. Hirota and K. Suzuki, *J. Phys. Soc. Jpn.* **28**, 1366 (1970).
 - [5] H. Ikezi, *Phys. Fluids* **16**, 1668 (1973).
 - [6] M. M. Scott, B. A. Kalinikos, and C. E. Patton, *J. Appl. Phys.* **94**, 5877 (2003).
 - [7] D. D. Stancil, *Theory of Magnetostatic Waves* (Springer-Verlag, New York, 1993).
 - [8] P. Kabos and V. S. Stalmachov, *Magnetostatic Waves and Their Applications* (Chapman & Hall, London, 1994).
 - [9] M. Chen, M. A. Tsankov, J. M. Nash, and C. E. Patton, *Phys. Rev. B* **49**, 12 773 (1994).
 - [10] B. A. Kalinikos, M. M. Scott, and C. E. Patton, *Phys. Rev. Lett.* **84**, 4697 (2000).
 - [11] S. O. Demokritov *et al.*, *Nature (London)* **426**, 159 (2003).
 - [12] M. J. Ablowitz and H. Segur, *Solitons and the Inverse Scattering Transform* (SIAM, Philadelphia, 1985).
 - [13] M. Remoissenet, *Waves Called Solitons: Concepts and Experiments* (Springer-Verlag, Berlin, 1999).
 - [14] J. M. Nash, P. Kabos, R. Staudinger, and C. E. Patton, *J. Appl. Phys.* **83**, 2689 (1998).
 - [15] A. N. Slavin, *Phys. Rev. Lett.* **77**, 4644 (1996).
 - [16] M. Wu, M. A. Kraemer, M. M. Scott, C. E. Patton, and B. A. Kalinikos, *Phys. Rev. B* **70**, 054402 (2004).
 - [17] J. M. Soto-Crespo, M. Grapinet, Ph. Grelu, and N. N. Akhmediev, *Phys. Rev. E* **70**, 066612 (2004).
 - [18] D. S. Ricketts, X. Li, and D. Ham, *IEEE Trans. Microwave Theory Tech.* **54**, 373 (2006).
 - [19] K. Suzuki, R. Hirota, and K. Yoshikawa, *Int. J. Electron.* **34**, 777 (1973).
 - [20] K. Suzuki, R. Hirota, and K. Yoshikawa, *Jpn. J. Appl. Phys.* **12**, 361 (1973).
 - [21] J. Ford, *Phys. Rep.* **213**, 271 (1992).
 - [22] N. N. Akhmediev, *Nature (London)* **413**, 267 (2001).
 - [23] N. N. Akhmediev, D. R. Heatley, G. I. Stegeman, and E. M. Wright, *Phys. Rev. Lett.* **65**, 1423 (1990).
 - [24] B. M. Lake, H. C. Yuen, H. Rungaldier, and W. E. Ferguson, *J. Fluid Mech.* **83**, 49 (1977).
 - [25] G. V. Simaey, Ph. Emplit, and M. Haelterman, *Phys. Rev. Lett.* **87**, 033902 (2001).

Hamiltonian formalism for two magnon scattering microwave relaxation: Theory and applications

Pavol Krivosik,^{a)} Nan Mo, Sangita Kalarickal,^{b)} and Carl E. Patton
Department of Physics, Colorado State University, Fort Collins, Colorado 80523

(Received 28 December 2006; accepted 3 February 2007; published online 16 April 2007)

A two magnon scattering theory for microwave relaxation in magnetic systems is formulated in the framework of the Hamiltonian formalism. The paper provides general expressions for inhomogeneity coupling coefficients in the case of localized inhomogeneities. An approximate solution for the relaxation rate of the ferromagnetic resonance uniform mode relaxation rate is presented. Two examples of the application of the theory are presented, one for bulk polycrystalline ferrites and one for polycrystalline metallic thin films. © 2007 American Institute of Physics.

[DOI: 10.1063/1.2717084]

I. INTRODUCTION

Processes that involve decay in the amplitude of magnetization oscillations, generally termed relaxation processes, are important for fundamental and practical reasons. These processes, for example, set a natural limit for switching times and magnetic recording data transfer rates.¹ There are two main pathways for magnetization relaxation: (i) energy transfer out of magnetic system to a thermal bath that consists of phonons or conduction electrons, for example, and (ii) energy redistribution within a magnetic system. The former is usually termed as intrinsic damping. The latter involves coupling between the various magnetization oscillation modes, often called spin waves in wave theory or magnons in quantum particle theory. These two terms are often used interchangeably.

In the lowest order magnon coupling process, where only two excitations are involved, one magnon is destroyed and another is created. Such a process is called two magnon scattering (TMS).² This process can be described in terms of a scattering of the spin waves due to bulk and/or surface inhomogeneities. In the case of static inhomogeneities, the scattering may be taken as elastic, so that the initial and final magnon states will have the same frequency ω . The state wave vectors, denoted by \mathbf{k} , however, will differ by amounts that correlate with the spatial variation of the inhomogeneities.

Two magnon scattering processes are often invoked to account for additions to the intrinsic ferromagnetic resonance (FMR) relaxation rate or resonance linewidth for bulk^{3,4} and thin film⁵ ferrites as well as metallic magnetic films and multilayers.⁶⁻⁸ The driven FMR mode is usually spatially uniform or near uniform and is taken to correspond to a $\mathbf{k} = 0$ spin wave excitation. A valid two magnon scattering relaxation channel for the uniform mode requires two things: (1) available nonzero \mathbf{k} modes that are at the same frequency as the driven FMR mode and (2) inhomogeneities with ap-

propriate sizes or size distributions to couple the FMR mode to these degenerate spin wave modes. The total FMR relaxation rate then reflects a decay of uniform mode magnons due to TMS as well as intrinsic processes.

In the case of weak inhomogeneities, the coupling between uniform and nonuniform modes can be treated as a small perturbation and the TMS contribution to the relaxation rate can be evaluated by Fermi's golden rule. This quantum mechanical approach has been adopted by several authors.⁹⁻¹¹ Reviews may be found in Refs. 2 and 12, for example. Alternative methods involve the evaluation of the inhomogeneity contribution to the microwave susceptibility^{13,14} or the magnetization time response,^{15,16} as well as the direct numerical diagonalization of the Hamiltonian with inhomogeneity coupling terms included.^{17,18} Higher order approaches include considerations of secondary scattering between nonuniform magnons¹⁹ and modifications in the density of degenerate states in the presence of inhomogeneities.²⁰

Two magnon scattering contributions to the uniform mode ferromagnetic resonance relaxation rate have been investigated theoretically and experimentally since the late 1950s. The very early works focused on TMS processes in bulk ferrites. The intense technological interest in ferrite based radar devices drives continuing work in this area to the present day. The main contributions to the TMS relaxation rate in ferrite systems come from (i) coupling due to the dipole fields associated with pores and surface voids^{9,10} and (ii) effective field fluctuations associated with the magnetocrystalline anisotropy of the randomly oriented grains in polycrystalline samples.²¹ The particular case of the thin ferrite disk geometry was considered, for example, by Sparks²² and most recently by Hurben and Patton,²³ among others.

There has also been a strong interest in TMS relaxation in metallic thin films. Wigen²⁴ was the first to incorporate the TMS theory into the analysis of linewidth data for obliquely magnetized Permalloy films. In this analysis, however, the density of degenerate states was evaluated from bulk spin wave dispersion relations rather than those applicable to thin films. It is known, however, that the dynamic dipole fields associated with film surfaces can modify the applicable dis-

^{a)}On leave from the Department of Electromagnetic Field Theory, Faculty of Electrical Engineering and Information Technology, Bratislava, Slovakia.

^{b)}Present address: Institute für Experimentalphysik, Freie Universität Berlin, Arnimallee 14, 14197 Berlin, Germany.

persion relations^{25,26} and density of states considerations in a significant way. Such effects can lead, for example, to profound dependences of the FMR linewidth on the film thickness.

A semiquantitative discussion of two magnon scattering contributions to the FMR linewidth in thin metallic films was first provided by Patton *et al.*⁶ for in-plane magnetized Permalloy films. The full theoretical analysis of two magnon scattering processes in thin metallic films started some decades later with the work of Arias and Mills.¹⁶ Their model involved scattering from regularly shaped surface defects due to both dipole fields and surface anisotropy, and it specifically addressed the situation for ultrathin films. The model predictions have been tested experimentally by Lindner *et al.*²⁷ and McMichael *et al.*,²⁸ for example. Recently, McMichael and Krivosik presented a detailed classical model of TMS relaxation for localized randomly distributed inhomogeneities.¹⁴ Nonlocal dipole scattering due to a random surface roughness has been treated by Dobin and Victora²⁹ and by Maranville *et al.*³⁰

This article follows closely the TMS analysis of McMichael and Krivosik¹⁴ for localized scattering. The theory presented here, however, is formulated within the framework of a Hamiltonian formalism. This approach is widely used in the theory of weakly dissipative systems, and it is particularly suitable for the study of nonlinear magnetic excitations.^{31,32} Recently, for example, there has been a large amount of Hamiltonian based theory on a wave front reversal in ferrite films.^{33,34} This phenomenon involves both two magnon scattering and nonlinear parametric processes, and this combination holds significant potential for new microwave signal processing devices. Hamiltonian approaches to TMS processes have also been used in the analysis of nonlinear magnetization dynamics in the vicinity of the ferromagnetic resonance^{35,36} and large angle switching.²⁹ In spite of the above activity, there exists no general and comprehensive statement of the formal Hamiltonian TMS theory and the corresponding Hamiltonian coefficients for basic magnetic systems. This work addresses this problem.

Section II presents the basic theoretical approach. It gives a review of the working equations for the dynamic magnetization response in a homogeneous sample, provides general expressions for the inhomogeneity coupling coefficients for localized inhomogeneities, and presents an approximate solution for a uniform mode free decay response. Section III provides an example calculation for anisotropy scattering in a polycrystalline sphere. In Sec. IV, a simplified theoretical approach is used for the analysis of the original data on Permalloy thin films from Ref. 6. Section V provides a summary and conclusions. Gaussian units are used throughout.

II. THE HAMILTONIAN FORMALISM

A. Dynamic magnetization response and equation of motion

This section provides an overview of the Hamiltonian method in the spin-wave theory. There are several methods for the theoretical analysis of spin wave excitations in ferro-

magnets. In the classical approach, spin waves are regarded as propagating deviations of the macroscopic magnetization \mathbf{M} from equilibrium. The dynamics of these deviations derives from the classical torque equation of motion,

$$\frac{d\mathbf{M}(\mathbf{r},t)}{dt} = -|\gamma|\mathbf{M}(\mathbf{r},t) \times \mathbf{H}_{\text{eff}}(\mathbf{r},t), \quad (1)$$

where γ is the electron gyromagnetic ratio and $\mathbf{H}_{\text{eff}}(\mathbf{r},t)$ is a net effective field that includes both external and internal field components. In order to facilitate the analysis of the spin wave dynamics and interactions in a compact way, Eq. (1) is commonly transformed into a set of equations of motion for scalar complex Fourier component spin-wave amplitudes. The Hamiltonian formalism provides a way to achieve such a transformation in four conceptually simple steps.

In the first step, one needs to write down the total magnetic energy \mathcal{H} in specific form. In general terms, \mathcal{H} may be written according to

$$\mathcal{H} = \int_V \mathcal{W} d^3r, \quad (2)$$

where \mathcal{W} is an energy density and the integral is over the sample volume V . Both \mathcal{H} and \mathcal{W} are real. The connection between this energy and the effective field in Eq. (1) is given by

$$\mathbf{H}_{\text{eff}}(\mathbf{r},t) = -\frac{1}{V} \frac{\delta \mathcal{H}}{\delta \mathbf{M}(\mathbf{r},t)}, \quad (3)$$

with the variational derivative defined in the standard way

$$\frac{\delta \mathcal{H}}{\delta \mathbf{M}} = V \left[\frac{\partial \mathcal{W}}{\partial \mathbf{M}} - \sum_{\alpha=x,y,z} \frac{d}{d\alpha} \frac{\partial \mathcal{W}}{\partial (d\mathbf{M}/d\alpha)} \right]. \quad (4)$$

In the second step, the magnetization components $M_{x,y,z}$ are expressed in terms of a pair of conjugate variables $a(\mathbf{r},t)$ and $a^*(\mathbf{r},t)$ according to

$$iM_x(\mathbf{r},t) + M_y(\mathbf{r},t) = M_s a(\mathbf{r},t) \sqrt{2 - a(\mathbf{r},t)a^*(\mathbf{r},t)} \quad (5)$$

and

$$M_z(\mathbf{r},t) = M_s [1 - a(\mathbf{r},t)a^*(\mathbf{r},t)]. \quad (6)$$

Here, M_s denotes the saturation magnetization of the material of interest. This transformation was first developed by Schlömann.^{31,37} It has been used by many authors for the study of spin wave dynamics and related problems.³⁸⁻⁴¹ One can see that in the small signal limit a has a simple physical interpretation, namely, $a \propto i\alpha_x + \alpha_y$, where $\alpha_{x,y}$ are the x - and y -direction cosines of the magnetization vector \mathbf{M} .

With the use of Eqs. (5) and (6), Eq. (1) may be transformed into a pair of coupled equations of motion for $a(\mathbf{r},t)$ and $a^*(\mathbf{r},t)$ in Hamiltonian form, according to

$$i \frac{da(\mathbf{r},t)}{dt} = \frac{\delta \mathcal{U}}{\delta a^*(\mathbf{r},t)} \quad (7)$$

and the corresponding complex conjugate expression, $-ida^*(\mathbf{r},t)/dt = \delta \mathcal{U} / \delta a(\mathbf{r},t)$. In the above, \mathcal{U} is the magnetic energy from Eq. (2), but now expressed in frequency units according to

$$\mathcal{U} = \frac{|\gamma|}{M_s V} \mathcal{H}. \quad (8)$$

As with \mathcal{H} , \mathcal{U} is always real.

In the third step, the spatial dependences of the conjugate variables $a(\mathbf{r}, t)$ and $a^*(\mathbf{r}, t)$ are expanded in a suitable basis system. In the usual case, linear normal modes for a given sample geometry are chosen as the basis functions. The appropriate choice in many situations is a plane wave Fourier series expansion according to

$$a(\mathbf{r}, t) = \sum_{\mathbf{k}} a_{\mathbf{k}}(t) e^{i\mathbf{k} \cdot \mathbf{r}} \quad (9)$$

along with the corresponding complex conjugate expression for $a^*(\mathbf{r}, t)$. Each $a_{\mathbf{k}}(t)$ and $a_{\mathbf{k}}^*(t)$ expansion coefficient represents the complex amplitude of a planar spin wave that propagates in a direction of the wave vector \mathbf{k} . The $\mathbf{k}=0$ mode corresponds to the uniform magnetization mode. Such a plane wave expansion has been established as a permissible approximation for bulk samples as long as the mode wavelength ($2\pi/|\mathbf{k}|$) is much smaller than the sample dimensions. Plane wave expansion has been also employed for laterally unbounded ultrathin films for which the condition $|\mathbf{k}|d \ll 1$ is satisfied, where d is the film thickness.⁴² In this ultrathin film limit, the dynamic magnetization amplitude can be taken to be uniform across the film thickness, and the normal modes are, in essence, propagating plane waves confined in the film cross section. The Fourier expansion is then over \mathbf{k} vectors constrained to the film plane.

The $a_{\mathbf{k}}$ variables are often rescaled as $\hat{a}_{\mathbf{k}} = \sqrt{M_s V / g \mu_B} a_{\mathbf{k}}$, where g is the Landé g factor and μ_B is the Bohr magneton.^{13,19} A given pair of these rescaled $\hat{a}_{\mathbf{k}}$ and $\hat{a}_{\mathbf{k}}^*$ then represent the classical analog to the usual magnon annihilation and creation operator pair in the second quantization formalism of quantum mechanics.⁴³ This analog originates from the fact that each excited spin wave reduces the z component of the total magnetic moment of the sample by a given amount, either by $M_s V a_{\mathbf{k}} a_{\mathbf{k}}^*$ or by $g \mu_B \hat{a}_{\mathbf{k}} \hat{a}_{\mathbf{k}}^*$.

The Fourier transform operation is canonical and the equations of motion for the $a_{\mathbf{k}}$ and $a_{\mathbf{k}}^*$ will therefore retain the Hamiltonian form of Eq. (7), but with the variational derivatives replaced by partial derivatives. This replacement relates to the fact that the $a_{\mathbf{k}}$ and $a_{\mathbf{k}}^*$ are amplitudes in discrete \mathbf{k} space.

There is one more crucial modification. Intrinsic dissipation due to interactions between the spin waves and the thermal bath is accommodated through the *ad hoc* addition of a relaxation rate $\eta_{\mathbf{k}}$ term to the coupled equations of motion for $a_{\mathbf{k}}$ and $a_{\mathbf{k}}^*$.^{31,32} This relaxation rate $\eta_{\mathbf{k}}$ parameter is real. In principle, such a term could also be obtained directly from additional Hamiltonian terms that represent spin wave coupling to the thermal bath.⁴⁴ The development will show that in the first order approximation, the two magnon relaxation rate term simply adds to the $\eta_{\mathbf{k}}$ just introduced. By implication, other two particle interaction terms will have the same effect, at least to lowest order. The $\eta_{\mathbf{k}}$, therefore, simply accounts for intrinsic thermal bath decay terms in a heuristic way.

Based on the above, the coupled equations of motion for the $a_{\mathbf{k}}$ and $a_{\mathbf{k}}^*$ may be written according to

$$i \left(\frac{d}{dt} + \eta_{\mathbf{k}} \right) a_{\mathbf{k}}(t) = \frac{\partial \mathcal{U}}{\partial a_{\mathbf{k}}^*(t)} \quad (10)$$

and

$$-i \left(\frac{d}{dt} + \eta_{\mathbf{k}} \right) a_{\mathbf{k}}^*(t) = \frac{\partial \mathcal{U}}{\partial a_{\mathbf{k}}(t)}. \quad (11)$$

In the fourth and final step, the energy \mathcal{U} is expanded in a power series in the $a_{\mathbf{k}}$ and $a_{\mathbf{k}}^*$, written as $\mathcal{U} = \mathcal{U}^{(0)} + \mathcal{U}^{(1)} + \mathcal{U}^{(2)} + \dots$. The superscripts indicate the degree in powers of the different $a_{\mathbf{k}}$, $a_{\mathbf{k}}^*$, $a_{\mathbf{k}} a_{\mathbf{k}'}$, $a_{\mathbf{k}} a_{\mathbf{k}'}^*$, etc., products. Although the initial Hamiltonian is usually easy to write down, this expansion in the $a_{\mathbf{k}}$ and $a_{\mathbf{k}}^*$ is often tedious to obtain. When completed, however, it allows for the evaluation of all of the different orders of spin wave interaction processes in an extremely simple manner. This operational simplicity will become clear in the sections to follow.

B. Normal modes and spin wave dispersion for a homogeneous sample

From the derivative form on the right sides of Eqs. (10) and (11), one can see that a truncation of the \mathcal{U} expansion beyond the quadratic terms in the $a_{\mathbf{k}}$ and $a_{\mathbf{k}}^*$ corresponds to a linearization of the equation of motion. The zeroth order term is immaterial for dynamics. The first order term in the \mathcal{U} expansion defines static equilibrium and may also include a pumping term from the external fields. The linearized normal modes of the magnetic system are fully defined, therefore, through the quadratic $\mathcal{U}^{(2)}$ part of the energy. For a spatially homogeneous sample, this part may be expressed as

$$\mathcal{U}_{\text{hom}}^{(2)} = \sum_{\mathbf{k}} \left\{ A_{\mathbf{k}} a_{\mathbf{k}}^*(t) a_{\mathbf{k}}(t) + \frac{1}{2} [B_{\mathbf{k}} a_{\mathbf{k}}^*(t) a_{-\mathbf{k}}^*(t) + \text{c.c.}] \right\}. \quad (12)$$

The expansion coefficients $A_{\mathbf{k}}$ and $B_{\mathbf{k}}$ take the form

$$A_{\mathbf{k}} = \frac{|\gamma|}{2} (H_{xx, \mathbf{k}} + H_{yy, \mathbf{k}}) \quad (13)$$

and

$$B_{\mathbf{k}} = \frac{|\gamma|}{2} (-H_{xx, \mathbf{k}} + H_{yy, \mathbf{k}} + 2iH_{xy, \mathbf{k}}), \quad (14)$$

where $H_{xx, \mathbf{k}}$, $H_{yy, \mathbf{k}}$, and $H_{xy, \mathbf{k}}$ are components of what will be termed the *homogeneous stiffness field tensor*. The specific form of these components will depend on the system of interest.^{45,46} An outline of the development of these terms is given in the Appendix. Two sets of specific expressions, one for bulk samples of ellipsoidal shape and one for in-plane magnetized thin films, are given in Secs. III and IV. Note that $H_{xx, \mathbf{k}}$, $H_{yy, \mathbf{k}}$, and $H_{xy, \mathbf{k}}$ are real. This means, in turn, that $A_{\mathbf{k}}$ is also real and the conditions $A_{\mathbf{k}} = A_{-\mathbf{k}}$ and $B_{\mathbf{k}} = B_{-\mathbf{k}}$ are valid.

With the form of $\mathcal{U}_{\text{hom}}^{(2)}$ as given in Eq. (12), Eqs. (10) and (11) will comprise coupled equations of motion for a given pair of $a_{\mathbf{k}}$ and $a_{\mathbf{k}}^*$ amplitudes or, equivalently, pairs of $a_{\mathbf{k}}$ and $a_{-\mathbf{k}}^*$ amplitudes. For some aspects of the analysis, the

$(a_{\mathbf{k}}, a_{-\mathbf{k}}^*)$ form proves convenient. The decoupling can be accomplished through a canonical transformation first developed by Holstein and Primakoff (HP).⁴⁷ For the present purposes, this transformation may be written as

$$a_{\mathbf{k}}(t) = u_{\mathbf{k}} c_{\mathbf{k}}(t) + v_{\mathbf{k}} c_{-\mathbf{k}}^*(t), \quad (15)$$

where the transformation coefficients are specified through

$$u_{\mathbf{k}} = \sqrt{\frac{A_{\mathbf{k}} + \omega_{\mathbf{k}}}{2\omega_{\mathbf{k}}}}, \quad (16)$$

$$v_{\mathbf{k}} = -\frac{B_{\mathbf{k}}}{|B_{\mathbf{k}}|} \sqrt{\frac{A_{\mathbf{k}} - \omega_{\mathbf{k}}}{2\omega_{\mathbf{k}}}}, \quad (17)$$

and

$$\omega_{\mathbf{k}} = \sqrt{A_{\mathbf{k}}^2 - |B_{\mathbf{k}}|^2} = |\gamma| \sqrt{H_{xx,\mathbf{k}} H_{yy,\mathbf{k}} - H_{xy,\mathbf{k}}^2}. \quad (18)$$

Equation (18) also gives the $\omega_{\mathbf{k}}(\mathbf{k})$ dispersion relation for the normal mode excitations associated with these amplitudes. From the properties of $A_{\mathbf{k}}$ and $B_{\mathbf{k}}$ it follows that (1) the $u_{\mathbf{k}}$ are real and (2) the conditions $u_{\mathbf{k}} = u_{-\mathbf{k}}$, $v_{\mathbf{k}} = v_{-\mathbf{k}}$, and $\omega_{\mathbf{k}} = \omega_{-\mathbf{k}}$ are satisfied.

The HP transformation casts Eq. (12) into a *diagonal form* as $\mathcal{U}_{\text{hom}}^{(2)} = \sum_{\mathbf{k}} \omega_{\mathbf{k}} c_{\mathbf{k}}^*(t) c_{\mathbf{k}}(t)$. The new pair of conjugate variables $c_{\mathbf{k}}(t)$ and $c_{\mathbf{k}}^*(t)$ correspond to the linear normal spin wave modes. Since the transformation from the $a_{\mathbf{k}}$ and $a_{\mathbf{k}}^*$ to the $c_{\mathbf{k}}$ and $c_{\mathbf{k}}^*$ is canonical, the equations of motion for the $c_{\mathbf{k}}$ and $c_{\mathbf{k}}^*$ follow the same form as for the $a_{\mathbf{k}}$ and $a_{\mathbf{k}}^*$. However, insofar as $\mathcal{U}_{\text{hom}}^{(2)}$ is diagonal in $c_{\mathbf{k}}$ and $c_{\mathbf{k}}^*$, the equations of motion are now uncoupled. One then has

$$i \left(\frac{d}{dt} + \eta_{\mathbf{k}} \right) c_{\mathbf{k}}(t) = \frac{\partial \mathcal{U}_{\text{hom}}^{(2)}}{\partial c_{\mathbf{k}}^*(t)} = \omega_{\mathbf{k}} c_{\mathbf{k}}(t), \quad (19)$$

along with the counterpart equation for $c_{\mathbf{k}}^*(t)$. For a homogeneous system, the dispersion $\omega_{\mathbf{k}}(\mathbf{k})$, together with the relaxation rate parameter $\eta_{\mathbf{k}}$, now provides all the information needed to describe the linear spin wave dynamics. The $c_{\mathbf{k}}(t)$ and $c_{\mathbf{k}}^*(t)$ correspond to plane waves with a well defined dispersion. One can also work backwards, as needed, to extract the physical dynamic magnetization response as a Fourier superposition of these normal modes, suitably transformed.

The working equations developed up to now constitute the lead into the main problem at hand, namely, the spin wave dynamics and the additional relaxation processes that are present in the presence of inhomogeneities. The next section considers the extension of the formalism established so far to this problem. The new ingredient is a spatial variation of the stiffness fields due to the inhomogeneities. This results in a new coupling between spin wave modes at the same frequency but with different wave vectors, or, in other words, two magnon scattering.

C. Inhomogeneity coupling and mode mixing

Spatial inhomogeneities introduce an additional contribution to the energy density that will be denoted as $\tilde{\mathcal{W}}$. In what follows, a tilde (\sim) will be used to denote any inhomogeneity related quantity. Spatial inhomogeneities may be classified according to the sources of the spatial fluctuating

effective field and separated into two categories, local and nonlocal. A polycrystalline ferrite or thin film with densely packed randomly oriented crystalline grains, for example, constitutes a system with local inhomogeneities. Samples with pores, pits, or surface irregularities that produce long range dipole fields, on the other hand, provide examples of nonlocal inhomogeneities. The formulation here will focus on local inhomogeneities. In the case of nonlocal scattering processes, one can cast the working equations in a similar form, albeit with a somewhat more complex analysis than that given below.²⁹

For the dense polycrystalline sample with local inhomogeneities, the important contributions to $\tilde{\mathcal{W}}$ generally derive from the magnetocrystalline anisotropy in randomly oriented grains and the \mathbf{r} -dependent variation in \mathbf{M} associated with the plane and spin waves. This second effect is critical. It is present even for a completely saturated sample with a uniform and \mathbf{r} -independent static magnetization, the situation considered below. In the simple case of uniaxial grains, one can write $\tilde{\mathcal{W}}(\mathbf{r}, \mathbf{M}) = -K_u(\mathbf{r})/M_s^2 [\mathbf{e}(\mathbf{r}) \cdot \mathbf{M}(\mathbf{r})]^2$, where $K_u(\mathbf{r})$ represents the spatially dependent uniaxial anisotropy energy density parameter and $\mathbf{e}(\mathbf{r})$ is a unit vector that defines the grain-to-grain \mathbf{r} -dependent uniaxial easy axis. Later in the analysis, the practical parameters of importance will be developed in terms of the components of an \mathbf{r} -dependent 2×2 effective field tensor $\tilde{\mathbf{h}}(\mathbf{r})$ and the corresponding Fourier components of these fields.

Turn now to the dynamics. For purposes of analysis, it is assumed that the sample remains magnetically saturated with a well defined static and \mathbf{r} -independent magnetization vector specified as $\mathbf{M}_0 = M_s \hat{\mathbf{z}}$. One also takes the dynamic magnetization, given by $\mathbf{m}(\mathbf{r}, t) = [\mathbf{M}(\mathbf{r}, t) - \mathbf{M}_0]$, to be small. In this limit, $\tilde{\mathcal{W}}(\mathbf{r}, \mathbf{M})$ may be expanded in a Taylor series about the magnetization equilibrium position. Taken out to second order terms only, $\tilde{\mathcal{W}}(\mathbf{r}, \mathbf{M})$ takes the form

$$\begin{aligned} \tilde{\mathcal{W}}(\mathbf{r}, \mathbf{M}) \approx & \tilde{\mathcal{W}}(\mathbf{r}, \mathbf{M}_0) + \nabla_{\mathbf{M}} \tilde{\mathcal{W}}(\mathbf{r}, \mathbf{M})|_{\mathbf{M}_0} \cdot \mathbf{m}(\mathbf{r}, t) \\ & + \frac{1}{2} \mathbf{m}^T(\mathbf{r}, t) \cdot \nabla_{\mathbf{M}} \nabla_{\mathbf{M}} \tilde{\mathcal{W}}(\mathbf{r}, \mathbf{M})|_{\mathbf{M}_0} \cdot \mathbf{m}(\mathbf{r}, t). \end{aligned} \quad (20)$$

One then proceeds to apply the same transformations developed in the previous sections to the dynamic magnetization, first in terms of the conjugate $a(\mathbf{r}, t)$ and $a^*(\mathbf{r}, t)$ variables, then in terms of the $a_{\mathbf{k}}$ and $a_{\mathbf{k}}^*$, and finally in terms of the previously diagonal $c_{\mathbf{k}}$ and $c_{\mathbf{k}}^*$.

Recall that the second order homogeneous sample Hamiltonian $\mathcal{U}_{\text{hom}}^{(2)}$, after transformation to the $c_{\mathbf{k}}$ and $c_{\mathbf{k}}^*$, is diagonal and leads to the spin wave dispersion and normal modes. The corresponding second order terms in the $c_{\mathbf{k}}$ and $c_{\mathbf{k}}^*$ for the transformed $\tilde{\mathcal{W}}(\mathbf{r}, \mathbf{M})$ will be nondiagonal. The additional coupling between the $c_{\mathbf{k}}$ and $c_{\mathbf{k}}^*$ modes in this case can be viewed as the basis of two magnon scattering.

The algebra is somewhat tedious but straightforward. Only a brief roadmap is provided here. The first transformation leads to a second order energy density component, written in frequency units, that takes the form

$$\frac{|\gamma|}{M_s} \tilde{\mathcal{W}}^{(2)} = \tilde{A}(\mathbf{r}) a(\mathbf{r}, t) a^*(\mathbf{r}, t) + \frac{1}{2} [\tilde{B}(\mathbf{r}) a^*(\mathbf{r}, t) a(\mathbf{r}, t) + \text{c.c.}], \quad (21)$$

with coefficients $\tilde{A}(\mathbf{r}) = |\gamma| [\tilde{h}_{xx}(\mathbf{r}) + \tilde{h}_{yy}(\mathbf{r})]/2$ and $\tilde{B}(\mathbf{r}) = |\gamma| [-\tilde{h}_{xx}(\mathbf{r}) + \tilde{h}_{yy}(\mathbf{r}) + 2i\tilde{h}_{xy}(\mathbf{r})]/2$. The $\tilde{h}_{xx}(\mathbf{r})$, $\tilde{h}_{yy}(\mathbf{r})$, and $\tilde{h}_{xy}(\mathbf{r})$ denote the spatially dependent components of the inhomogeneous stiffness field tensor $\tilde{\mathbf{h}}(\mathbf{r})$. Formally, these components are given as

$$\tilde{h}_{\alpha\alpha}(\mathbf{r}) = M_s \left. \frac{\partial^2 \tilde{\mathcal{W}}(\mathbf{r}, \mathbf{M})}{\partial M_\alpha^2} \right|_{\mathbf{M}_0} - \left. \frac{\partial \tilde{\mathcal{W}}(\mathbf{r}, \mathbf{M})}{\partial M_z} \right|_{\mathbf{M}_0}, \quad \alpha = x, y \quad (22)$$

and

$$\tilde{h}_{xy}(\mathbf{r}) = M_s \left. \frac{\partial^2 \tilde{\mathcal{W}}(\mathbf{r}, \mathbf{M})}{\partial M_x \partial M_y} \right|_{\mathbf{M}_0}. \quad (23)$$

Note that the functional forms for the new spatially dependent $\tilde{A}(\mathbf{r})$ and $\tilde{B}(\mathbf{r})$ functions in terms of the $\tilde{h}_{xx}(\mathbf{r})$, $\tilde{h}_{yy}(\mathbf{r})$, and $\tilde{h}_{xy}(\mathbf{r})$ parallel the original homogeneous sample $A_{\mathbf{k}}$ and $B_{\mathbf{k}}$ expressions in terms of the $H_{xx,\mathbf{k}}$, $H_{yy,\mathbf{k}}$, and $H_{xy,\mathbf{k}}$. This parallel form is not a coincidence. It is related directly to the quadratic form of the energy in both cases. This parallel structure also carries over to the equations that connect the Fourier transform parameters $\tilde{A}_{\mathbf{q}}$, $\tilde{B}_{\mathbf{q}}$, $\tilde{h}_{xx,\mathbf{q}}$, $\tilde{h}_{yy,\mathbf{q}}$, and $\tilde{h}_{xy,\mathbf{q}}$. The second transformation makes direct use of these Fourier transforms and yields a second order Hamiltonian,

$$\begin{aligned} \tilde{\mathcal{U}}^{(2)} &= \frac{|\gamma|}{M_s V} \int_V \tilde{\mathcal{W}}^{(2)} d^3 r \\ &= \frac{1}{2} \sum_{\mathbf{q}, \mathbf{k}, \mathbf{k}'} [\tilde{A}_{\mathbf{q}} a_{\mathbf{k}}^*(t) a_{\mathbf{k}'}(t) \Delta_{\mathbf{q}-\mathbf{k}+\mathbf{k}'} \\ &\quad + \tilde{B}_{\mathbf{q}}^* a_{\mathbf{k}}(t) a_{\mathbf{k}'}^*(t) \Delta_{-\mathbf{q}+\mathbf{k}+\mathbf{k}'}] + \text{c.c.} \end{aligned} \quad (24)$$

The Kronecker delta (Δ) functions express the overall conservation of wave vector that includes the pseudomomentum of the Fourier components of the inhomogeneity terms.

It is useful at this point to contrast these $\tilde{h}_{xx,\mathbf{q}}$, $\tilde{h}_{yy,\mathbf{q}}$, and $\tilde{h}_{xy,\mathbf{q}}$ Fourier transformed inhomogeneous stiffness field tensor components with the previously developed $H_{xx,\mathbf{k}}$, $H_{yy,\mathbf{k}}$, and $H_{xy,\mathbf{k}}$ homogeneous sample stiffness field tensor components. The summary of the development for $H_{xx,\mathbf{k}}$, $H_{yy,\mathbf{k}}$, and $H_{xy,\mathbf{k}}$ in the Appendix illustrates how these fields derive from internal effective fields taken as linear functionals of the vector magnetization. The \mathbf{k} dependences for these Fourier component fields therefore reflect the nature of the mutual interactions between the magnetic moments or the interaction with external field. In contrast, the $\tilde{h}_{xx,\mathbf{q}}$, $\tilde{h}_{yy,\mathbf{q}}$, and $\tilde{h}_{xy,\mathbf{q}}$ stiffness fields derive from the inhomogeneous energy density $\tilde{\mathcal{W}}(\mathbf{r}, \mathbf{M})$, and their wave vector dependences reflect primarily the spatial variation in the material inhomogeneities.

Apart from the details, however, these Fourier component field terms will be large when $|\mathbf{q}|$ is on the order of an inverse grain size. The sizes of these terms will be on the order of the anisotropy field parameter $2K_u/M_s$. At the same time, the $\Delta_{\pm\mathbf{q} \mp \mathbf{k} + \mathbf{k}'}$ factors in the terms in $\tilde{\mathcal{U}}^{(2)}$ will tend to couple specific \mathbf{k} and \mathbf{k}' modes that satisfy the condition $|\mathbf{k} - \mathbf{k}'| \approx |\mathbf{q}|$. This coupling is the source of the two magnon scattering.

In terms of the $c_{\mathbf{k}}$ and $c_{\mathbf{k}}^*$, the total second order Hamiltonian $\mathcal{U}^{(2)}$ takes the form

$$\begin{aligned} \mathcal{U}^{(2)} &= \mathcal{U}_{\text{hom}}^{(2)} + \tilde{\mathcal{U}}^{(2)} \\ &= \sum_{\mathbf{k}} \omega_{\mathbf{k}} c_{\mathbf{k}}^*(t) c_{\mathbf{k}}(t) + \frac{1}{2} \sum_{\mathbf{k}, \mathbf{k}'} [\tilde{G}_{\mathbf{k}, \mathbf{k}'} c_{\mathbf{k}}^*(t) c_{\mathbf{k}'}(t) \\ &\quad + \tilde{F}_{\mathbf{k}, \mathbf{k}'} c_{\mathbf{k}}^*(t) c_{\mathbf{k}'}^*(t) + \text{c.c.}]. \end{aligned} \quad (25)$$

The coefficients of the new $c_{\mathbf{k}}^* c_{\mathbf{k}'}$ and $c_{\mathbf{k}}^* c_{\mathbf{k}'}^*$ pair terms are given by

$$\tilde{G}_{\mathbf{k}, \mathbf{k}'} = \tilde{A}_{\mathbf{k}-\mathbf{k}'} (u_{\mathbf{k}} u_{\mathbf{k}'} + v_{\mathbf{k}} v_{\mathbf{k}'}^*) + \tilde{B}_{\mathbf{k}-\mathbf{k}'} u_{\mathbf{k}} v_{\mathbf{k}'}^* + \tilde{B}_{-\mathbf{k}+\mathbf{k}'}^* v_{\mathbf{k}} u_{\mathbf{k}'}, \quad (26)$$

and

$$\tilde{F}_{\mathbf{k}, \mathbf{k}'} = \tilde{A}_{\mathbf{k}+\mathbf{k}'} (u_{\mathbf{k}} v_{\mathbf{k}'} + v_{\mathbf{k}} u_{\mathbf{k}'}^*) + \tilde{B}_{\mathbf{k}+\mathbf{k}'} u_{\mathbf{k}} u_{\mathbf{k}'} + \tilde{B}_{-\mathbf{k}-\mathbf{k}'}^* v_{\mathbf{k}} v_{\mathbf{k}'}. \quad (27)$$

From the properties of the HP transformation, one can show that these coefficients satisfy the conditions $\tilde{G}_{\mathbf{k}, \mathbf{k}'} = \tilde{G}_{\mathbf{k}', \mathbf{k}}^*$ and $\tilde{F}_{\mathbf{k}, \mathbf{k}'} = \tilde{F}_{\mathbf{k}', \mathbf{k}}$.

The full $\tilde{G}_{\mathbf{k}, \mathbf{k}'}$ and $\tilde{F}_{\mathbf{k}, \mathbf{k}'}$ expressions given above appear to be fairly formidable. Section II D below, however, will show that the relevant parameter for uniform mode two magnon relaxation is $|\tilde{G}_{0, \mathbf{k}}|^2$. Section II E will then consider a further reduction in the form for $|\tilde{G}_{0, \mathbf{k}}|^2$ based on general considerations for the spatial correlation of the Fourier components of the stiffness field tensor $\tilde{\mathbf{h}}(\mathbf{r})$. Keep in mind that the $u_{\mathbf{k}}$ and $v_{\mathbf{k}}$ are defined through the $A_{\mathbf{k}}$ and the $B_{\mathbf{k}}$ coefficients in $\mathcal{U}_{\text{hom}}^{(2)}$. At the same time, the $\tilde{A}_{\mathbf{q}}$ and $\tilde{B}_{\mathbf{q}}$ track back to the Fourier components of $\tilde{\mathbf{h}}(\mathbf{r})$. For all terms, the surviving \mathbf{q} values are specified through the Kronecker delta functions in the terms of Eq. (24), with either \mathbf{k} or \mathbf{k}' set to zero. This means that all of the related parameters in $|\tilde{G}_{0, \mathbf{k}}|^2$ will ultimately track back to correlations between the surviving Fourier components of $\tilde{\mathbf{h}}(\mathbf{r})$, with multipliers that involve products of the homogeneous stiffness field tensor components $H_{xx,\mathbf{k}}$, $H_{yy,\mathbf{k}}$, and $H_{xy,\mathbf{k}}$, for $\mathbf{k}=0$ with those for $\mathbf{k} \neq 0$. A practical and fairly general working expression for $|\tilde{G}_{0, \mathbf{k}}|^2$ will be given in Sec. II E. Part of the power of the Hamiltonian approach is that the needed $|\tilde{G}_{0, \mathbf{k}}|^2$ for real systems can often be extracted in a relatively simple form. This will become clear from the examples considered in Secs. III and IV.

Apart from the apparent complexity of the $\tilde{G}_{\mathbf{k},\mathbf{k}'}$ and $\tilde{F}_{\mathbf{k},\mathbf{k}'}$, it is clear that the previously diagonal equation of motion for $c_{\mathbf{k}}(t)$ is no longer diagonal. This equation of motion now takes the form

$$i\left(\frac{d}{dt} + \eta_{\mathbf{k}}\right)c_{\mathbf{k}}(t) = \omega_{\mathbf{k}}c_{\mathbf{k}}(t) + \sum_{\mathbf{k}'} [\tilde{G}_{\mathbf{k},\mathbf{k}'}c_{\mathbf{k}'}(t) + \tilde{F}_{\mathbf{k},\mathbf{k}'}c_{\mathbf{k}'}^*(t)]. \quad (28)$$

One can see that the inclusion of inhomogeneities in the analysis, in combination with a proper Hamiltonian treatment of the extra terms in the energy, leads directly to new coupling terms in the equation of motion. The main contribution to the two magnon scattering relaxation for a given $c_{\mathbf{k}}$ mode is due to $\tilde{G}_{\mathbf{k},\mathbf{k}'}$ terms for $|\mathbf{k}'|$ values that are within an inverse grain size of the given $|\mathbf{k}|$. If the \mathbf{k} mode of interest is the uniform mode, for example, the coupling will be to all \mathbf{k}' modes within a sphere of radius $\sim \pi/\xi$, where ξ is the size of the grain or other inhomogeneity. As this analysis is applied to specific situations, the parameter ξ will carry over to a correlation length for the inhomogeneity of interest.

The above relations constitute a general formulation of the linearized spin wave equations of motion in the case of local inhomogeneity scattering. Nonlocal inhomogeneity scattering will lead to the same form of the Hamiltonian but with different coupling coefficients. From the development of the equations of motion, one can also see that the analysis can be easily extended beyond the small signal limit. One simply has to take higher order terms in the inhomogeneity energy Taylor expansion into account, along with the appropriate transformations. This relatively simple and conceptually straightforward inclusion of nonlinearity is a particular advantage of the Hamiltonian method. However, in the problems associated with nonlinear magnetization dynamics in the presence of inhomogeneities, it is usually sufficient to take the inhomogeneity contribution in the linearized form along with the higher order terms from the homogeneous Hamiltonian.^{31,33,34}

It is possible, in principle, to diagonalize the new total Hamiltonian (25) and find the new normal modes and the corresponding eigenfrequencies. Such a procedure has been used in Refs. 17 and 18, for example, for the numerical analysis of FMR spectra in thin films with simple types of inhomogeneities characterized by randomly distributed local fields. It is found, however, that the absorption profile for weak scattering is reasonably well described by the approximate solution for the uniform mode relaxation rate that can be found from the above working equations. Uniform mode decay is considered below.

D. Uniform mode free decay rate

A series of simplifications allows one to solve the augmented uniform mode ($\mathbf{k}=0$) free decay problem embodied in the above equations. The first such simplification is to ignore the secondary scattering between the nonuniform or $\mathbf{k} \neq 0$ modes. The basic argument here is that the multiple

scattering events among the $\mathbf{k} \neq 0$ will always occur with a very short characteristic time that can be neglected in the overall sequence of scattering events.

The set of coupled equations of motion for the single $c_0(t)$ and ensemble of $c_{\mathbf{k}}(t)$ amplitudes implicit in Eq. (28) may then be written in a simple form as

$$i\left(\frac{d}{dt} + \eta_0\right)c_0(t) = \omega_0c_0(t) + \sum_{\mathbf{k} \neq 0} [\tilde{G}_{0,\mathbf{k}}c_{\mathbf{k}}(t) + \tilde{F}_{0,\mathbf{k}}c_{\mathbf{k}}^*(t)] \quad (29)$$

and

$$i\left(\frac{d}{dt} + \eta_{\mathbf{k}}\right)c_{\mathbf{k}}(t) = \omega_{\mathbf{k}}c_{\mathbf{k}}(t) + \tilde{G}_{0,\mathbf{k}}^*c_0(t) + \tilde{F}_{0,\mathbf{k}}c_0^*(t), \quad \mathbf{k} \neq 0. \quad (30)$$

It is to be emphasized that the \mathbf{k} parameters in the above are explicitly for $\mathbf{k} \neq 0$ modes. The surviving coupling coefficients now involve only the $\mathbf{k}=0$ mode and individual uncoupled $\mathbf{k} \neq 0$ modes.

The second simplification is to seek $c_0(t)$ solutions in the adiabatic approximation. The uniform mode and $\mathbf{k} \neq 0$ modes are taken to have the forms $c_0(t) = \bar{c}_0(t)e^{-i\omega_0 t}$ and $c_{\mathbf{k}}(t) = \bar{c}_{\mathbf{k}}(t)e^{-i\omega_{\mathbf{k}} t}$, respectively, where the $\bar{c}_0(t)$ and $\bar{c}_{\mathbf{k}}(t)$ specify slowly time varying envelope functions. The above equations may then be combined to yield a $\bar{c}_0(t)$ equation of motion of the form

$$\frac{d\bar{c}_0(t)}{dt} = -\eta_0\bar{c}_0(t) - \int_0^t \tilde{W}(s)\bar{c}_0(t-s)ds, \quad (31)$$

with a driving function $\tilde{W}(s)$ given by

$$\tilde{W}(s) = \sum_{\mathbf{k} \neq 0} e^{-\eta_{\mathbf{k}} s} \{ |\tilde{G}_{0,\mathbf{k}}|^2 e^{i(\omega_0 - \omega_{\mathbf{k}})s} - |\tilde{F}_{0,\mathbf{k}}|^2 e^{i(\omega_0 + \omega_{\mathbf{k}})s} \}. \quad (32)$$

Under the slowly varying envelope assumption, one can neglect the retardation implicit in the $\tilde{W}(s)\bar{c}_0(t-s)$ integral term by setting $\bar{c}_0(t-s) \approx \bar{c}_0(t)$. The differential equation in Eq. (31) can then be solved by separation of variables. For times much longer than the inverse relaxation rate, or for $t \gg 1/\eta_{\mathbf{k}}$, however, the upper integration limit may be set to ∞ . One then obtains a relatively simple equation of motion for the envelope function $\bar{c}_0(t)$ given by

$$\frac{d\bar{c}_0(t)}{dt} \approx -(\eta_0 + \tilde{\Gamma}_0)\bar{c}_0(t), \quad (33)$$

where $\tilde{\Gamma}_0$ is given as a sum over the available nonzero \mathbf{k} states according to

$$\tilde{\Gamma}_0 = i \sum_{\mathbf{k} \neq 0} \left\{ \frac{|\tilde{G}_{0,\mathbf{k}}|^2}{\omega_0 - \omega_{\mathbf{k}} + i\eta_{\mathbf{k}}} - \frac{|\tilde{F}_{0,\mathbf{k}}|^2}{\omega_0 + \omega_{\mathbf{k}} + i\eta_{\mathbf{k}}} \right\} = i\tilde{\omega}_0 + \tilde{\eta}_0. \quad (34)$$

Keep in mind that the original homogeneous sample harmonic frequency response at ω_0 has already been taken out of the problem through the substitution $c_0(t) = \bar{c}_0(t)e^{-i\omega_0 t}$. It is clear, therefore, that the inhomogeneities bring in two effects. First, the inhomogeneity coupling produces a shift of

the uniform mode eigenfrequency ω_0 by an amount that corresponds to the imaginary part of $\tilde{\Gamma}_0$, namely, $\tilde{\omega}_0$. Second, the two magnon scattering also brings in an additional contribution to the relaxation rate given by the real part of $\tilde{\Gamma}_0$, namely, $\tilde{\eta}_0$. Both results are tied directly to the coupling coefficients $\tilde{G}_{0,\mathbf{k}}$ and $\tilde{F}_{0,\mathbf{k}}$. These, in turn, connect back to the fluctuating field Fourier components $\tilde{h}_{xx,\mathbf{q}}$, $\tilde{h}_{yy,\mathbf{q}}$, and $\tilde{h}_{xy,\mathbf{q}}$.

Notice two further characteristics of the $\tilde{\Gamma}_0$ source function for the two magnon decay and frequency shift. First, the denominators for the $\tilde{G}_{0,\mathbf{k}}$ terms are resonant. These terms are large only when $|\omega_0 - \omega_{\mathbf{k}}|$ is on the order of or smaller than the intrinsic spin wave relaxation rate $\eta_{\mathbf{k}}$. Loosely speaking, this means that only those modes within $\eta_{\mathbf{k}}$ of the uniform mode frequency ω_0 will contribute to the scattering. In quantum terms, this corresponds to energy conservation for the individual $\omega_0 \rightarrow \omega_{\mathbf{k}}$ mode scattering events, apart from the caveat of broadened spin wave modes. In contrast with the $\tilde{G}_{0,\mathbf{k}}$ term responses, the $\tilde{F}_{0,\mathbf{k}}$ term denominators are nonresonant. Under the reasonable assumption that $|\omega_0 + \omega_{\mathbf{k}}| \gg |\omega_0 - \omega_{\mathbf{k}}|$ is true, one can safely neglect the contributions of the $\tilde{F}_{0,\mathbf{k}}$ term to either the two magnon frequency shift $\tilde{\omega}_0$ or the two magnon relaxation rate $\tilde{\eta}_0$.

In the $\eta_{\mathbf{k}} \rightarrow 0$ limit the inhomogeneity contribution to the relaxation rate is reduced to the form

$$\tilde{\eta}_0 \approx \pi \sum_{\mathbf{k}} |\tilde{G}_{0,\mathbf{k}}|^2 \delta(\omega_0 - \omega_{\mathbf{k}}). \quad (35)$$

This Fermi golden rule form closely matches the result one would obtain directly from the quantum formulation of spin wave scattering. The usual factor of 2 in front of the sum from the quantum analysis is absent. This is due to the fact that relaxation rate $\tilde{\eta}_0$, as defined, reflects the decay of the uniform mode amplitude c_0 rather than the magnon occupation number which scales with $|c_0|^2$. The delta function in Eq. (35) conveys the stipulation that the usable \mathbf{k} modes must be degenerate with the uniform mode frequency. This degeneracy is one of the key constraints in practical calculations.

E. Randomly distributed inhomogeneities

It was noted in Sec. II C that the sought after $|\tilde{G}_{0,\mathbf{k}}|^2$ factors will all involve correlations between pairs of the surviving Fourier components of $\tilde{\mathbf{h}}(\mathbf{r})$ multiplied by products of the homogeneous stiffness field tensor components for $\mathbf{k}=0$ and those with $\mathbf{k} \neq 0$. The latter are a matter of algebra. The former require some discussion. These correlations may be expressed through a working relation,

$$\begin{aligned} \frac{1}{V} \int_V \tilde{h}_{\alpha\beta}(\mathbf{r}) \tilde{h}_{\alpha'\beta'}(\mathbf{r} + \mathbf{R}) d^3r \\ = \langle \tilde{h}_{\alpha\beta}(\mathbf{r}) \tilde{h}_{\alpha'\beta'}(\mathbf{r}) \rangle C(\mathbf{R}) \quad (\alpha, \beta, \alpha', \beta' = x, y), \end{aligned} \quad (36)$$

where $\langle \cdots \rangle$ denotes a spatial average and $C(\mathbf{R})$ is an appropriate correlation function. For practical purposes, the spatial average may be replaced by a configuration average.

Following Schlömann,²¹ plausible choices for $C(\mathbf{R})$ should generally include functions that are nonzero for $|\mathbf{R}|$

values that are on the order of or smaller than ξ and zero for $|\mathbf{R}| \gg \xi$, where ξ denotes the size of the inhomogeneity. The condition $C(0)=1$ is true, by definition. As a rule, the particular choice for $C(\mathbf{R})$ does not affect the final results in any significant way. For applications to $|\tilde{G}_{0,\mathbf{k}}|^2$, one needs the Fourier transform of Eq. (36). This is given as

$$\tilde{h}_{\alpha\beta,\mathbf{k}}^* \tilde{h}_{\alpha'\beta',\mathbf{k}} = \langle \tilde{h}_{\alpha\beta}(\mathbf{r}) \tilde{h}_{\alpha'\beta'}(\mathbf{r}) \rangle C_{\mathbf{k}}, \quad (37)$$

where $C_{\mathbf{k}}$ is the Fourier transform of $C(\mathbf{R})$. Two points should be noticed here. (1) The upper cutoff wave number in $C_{\mathbf{k}}$ is of the order of $|\mathbf{k}| \approx \pi/\xi$. (2) The limiting value of $C_{\mathbf{k}}$ in the low wave number limit will be on the order of $C_0 \approx V_{\xi}/V$, where V_{ξ} is a mean inhomogeneity volume. Both properties may be readily obtained from the properties of the correlation function $C(\mathbf{R})$ and the Fourier transform.

Based on the outline given in Sec. II C and the above correlation function nomenclature, it is straightforward to obtain $|\tilde{G}_{0,\mathbf{k}}|^2$ in terms of the various parameters developed or defined above. The result is

$$\begin{aligned} |\tilde{G}_{0,\mathbf{k}}|^2 = \frac{|\gamma|^4 C_{\mathbf{k}}}{4\omega_{\mathbf{k}}\omega_0} \{ & \langle \tilde{h}_{xx}^2 \rangle H_{yy,\mathbf{k}} H_{yy,0} + \langle \tilde{h}_{yy}^2 \rangle H_{xx,\mathbf{k}} H_{xx,0} \\ & + 2\langle \tilde{h}_{xx}\tilde{h}_{yy} \rangle (\omega_{\mathbf{k}}\omega_0 |\gamma|^2 + H_{xy,\mathbf{k}} H_{xy,0}) \\ & + \langle \tilde{h}_{xy}^2 \rangle [H_{xx,\mathbf{k}} H_{yy,0} + H_{yy,\mathbf{k}} H_{xx,0} \\ & - 2(\omega_{\mathbf{k}}\omega_0 |\gamma|^2 - H_{xy,\mathbf{k}} H_{xy,0})] \}. \end{aligned} \quad (38)$$

Note that the $H_{xx,\mathbf{k}}$, etc., denote the homogeneous sample stiffness field tensor components, and these occur as products of terms for $\mathbf{k}=0$ and $\mathbf{k} \neq 0$, while the $\langle \tilde{h}_{xx}^2 \rangle$, etc., denote the spatially averaged values of the indicated inhomogeneous stiffness field tensor component products, as indicated.

The evaluation of the specific spatial averages involves only knowledge of the specific energy form of interest. By way of example, Sec. III will present expressions for the spatially averaged product terms for cubic magnetocrystalline anisotropy obtained from previous work,¹⁴ along with general comments on the procedure.

F. Two magnon scattering as a uniform mode frequency perturbation

Before the consideration of specific calculations based on the above working equations, it is useful to examine a relatively simple intuitive result based on spatial linewidth broadening considerations. From Sec. II B, the uniform mode frequency for a homogeneous sample may be written as $\omega_0 = |\gamma|(H_{xx,0}H_{yy,0} - H_{xy,0}^2)^{1/2}$. One may now consider the inhomogeneous sample to be comprised of small grains, each with a slightly different *local* uniform mode frequency, specified as $\omega_0(\mathbf{r})$. The spatial dependence of $\omega_0(\mathbf{r})$ can be then obtained from the spatial variation of the uniform mode stiffness fields $\tilde{H}_{xx,0}(\mathbf{r}) = H_{xx,0} + \tilde{h}_{xx}(\mathbf{r})$, $\tilde{H}_{yy,0}(\mathbf{r}) = H_{yy,0} + \tilde{h}_{yy}(\mathbf{r})$, and $\tilde{H}_{xy,0}(\mathbf{r}) = H_{xy,0} + \tilde{h}_{xy}(\mathbf{r})$. The overall form of $\omega_0(\mathbf{r})$ will be the same as given above, but with the homogeneous sample stiffness fields replaced by the total stiffness fields

$$\omega_0(\mathbf{r}) \approx |\gamma| \sqrt{\tilde{H}_{xx,0}(\mathbf{r})\tilde{H}_{yy,0}(\mathbf{r}) - \tilde{H}_{xy,0}^2(\mathbf{r})}. \quad (39)$$

To the lowest order in the $\tilde{h}_{xx}(\mathbf{r})$, $\tilde{h}_{yy}(\mathbf{r})$, and $\tilde{h}_{xy}(\mathbf{r})$, the spatial frequency deviation from ω_0 , taken as $\delta\omega_0(\mathbf{r})$, is obtained as

$$\begin{aligned} \delta\omega_0(\mathbf{r}) &= \frac{\partial\omega_0}{\partial H_{xx,0}} \tilde{h}_{xx}(\mathbf{r}) + \frac{\partial\omega_0}{\partial H_{yy,0}} \tilde{h}_{yy}(\mathbf{r}) + \frac{\partial\omega_0}{\partial H_{xy,0}} \tilde{h}_{xy}(\mathbf{r}) \\ &= \frac{|\gamma|}{2\omega_0} \{H_{xx,0}\tilde{h}_{yy}(\mathbf{r}) + H_{yy,0}\tilde{h}_{xx}(\mathbf{r}) - 2H_{xy,0}\tilde{h}_{xy}(\mathbf{r})\}. \end{aligned} \quad (40)$$

One can see, therefore, that the spatial variations in the inhomogeneous sample stiffness fields yield a corresponding spatial inhomogeneous broadening in the FMR frequency. One can then take the Fourier transform of $\delta\omega_0(\mathbf{r})$, denoted as $\delta\omega_{0,\mathbf{k}}$, as a coupling coefficient between $\mathbf{k}=0$ and $\mathbf{k} \neq 0$ magnetization modes. Indeed, in the limit of low \mathbf{k} scattering, that is, for scattering to modes with $\mathbf{k} \approx 0$, one can show that $|\tilde{G}_{\mathbf{k},0}|^2$ is reduced to a simple physical form, namely,

$$|\tilde{G}_{\mathbf{k},0}|^2 \approx |\delta\omega_{0,\mathbf{k}}|^2 = \langle \delta\omega_0^2(\mathbf{r}) \rangle C_{\mathbf{k}}. \quad (41)$$

For weak, long wavelength inhomogeneities, therefore, the two magnon scattering process amounts to a frequency broadening effect ameliorated by the correlation function of the fluctuations that are the source of the scattering in the first place.

In the limit of zero intrinsic damping, one can make use of Eq. (35), apply the frequency line broadening connection, and obtain

$$\tilde{\eta}_0 \approx \pi \langle \delta\omega_0^2(\mathbf{r}) \rangle \sum_{\mathbf{k}} C_{\mathbf{k}} \delta(\omega_0 - \omega_{\mathbf{k}}) \approx \pi \langle \delta\omega_0^2(\mathbf{r}) \rangle C_0 g(\omega_0), \quad (42)$$

where $g(\omega_0) = \sum_{\mathbf{k}} \delta(\omega_0 - \omega_{\mathbf{k}})$ is the total density of states for the low \mathbf{k} spin wave modes that are degenerate with the uniform mode. For a well characterized sample, all of the quantities in Eq. (42) are known. One has, therefore, a reasonable expression for the two magnon relaxation rate based on relatively simple physical considerations on the resonance frequency broadening.

III. ANISOTROPY SCATTERING IN A POLYCRYSTALLINE FERRITE SPHERE

This section summarizes a representative calculation of the two magnon scattering relaxation rate for a bulk [three-dimensional (3D)] insulating material. As a specific example, a dense polycrystalline ferrite sphere magnetized to saturation by a uniform static field H is considered. It is assumed that grain orientations are randomly distributed and that each grain is comprised of a single crystal with cubic magnetocrystalline anisotropy. This is the classic two magnon scattering problem first treated by Schlömann.²¹ As in Ref. 21, intrinsic damping will be neglected. The starting point for the analysis is Eq. (35).

The needed parameters for the isotropic sphere sample are (1) the homogeneous sample stiffness fields, $H_{xx,\mathbf{k}}$, $H_{yy,\mathbf{k}}$,

and $H_{xy,\mathbf{k}}$, both for a general \mathbf{k} value and for $\mathbf{k}=0$, (2) the corresponding spatial averages for the inhomogeneous sample stiffness fields given by $\langle \tilde{h}_{xx}^2 \rangle$, $\langle \tilde{h}_{yy}^2 \rangle$, $\langle \tilde{h}_{xy}^2 \rangle$, and $\langle \tilde{h}_{xx}\tilde{h}_{yy} \rangle$, and (3) the correlation function Fourier transform, $C_{\mathbf{k}}$. For computational purposes, one also needs to convert from the \mathbf{k} sum over degenerate spin wave modes to an integral, according to $\sum_{\mathbf{k}} \rightarrow V/(2\pi)^3 \int \int \int k^2 \sin \theta_k dk d\theta_k d\phi_k$. This conversion is justified for typical macroscopic sample sizes.

The homogeneous sample stiffness field algebra is based on the method outlined in the Appendix. The internal effective field is comprised of the static field, uniform demagnetizing fields, exchange fields, and dipole-dipole fields with surface effects neglected. The components of the spin wave stiffness fields are obtained as

$$H_{xx,\mathbf{k}} = H_i + Dk^2 + 4\pi M_s \sin^2 \theta_k \cos^2 \phi_k, \quad (43)$$

$$H_{yy,\mathbf{k}} = H_i + Dk^2 + 4\pi M_s \sin^2 \theta_k \sin^2 \phi_k, \quad (44)$$

and

$$H_{xy,\mathbf{k}} = 4\pi M_s \sin^2 \theta_k \sin \phi_k \cos \phi_k. \quad (45)$$

In the above, $H_i = H - 4\pi M_s/3$ is the internal static field and D is an exchange constant. The ϕ_k and θ_k denote the standard azimuthal and polar spin wave propagation angles, respectively, that define the direction of the wave vector \mathbf{k} relative to the direction of the static field. The above fields combine to give a bulk sample spin wave frequency $\omega_{\mathbf{k}}$ written in the standard form as

$$\omega_{\mathbf{k}} = \sqrt{(H_i + Dk^2)(H_i + Dk^2 + 4\pi M_s \sin^2 \theta_k)}. \quad (46)$$

Note that the bulk sample $\omega_{\mathbf{k}}(\mathbf{k})$ function contains no azimuthal angle dependence. The homogeneous sample stiffness fields for $\mathbf{k}=0$ are given by

$$H_{xx,0} = H_{yy,0} = H = \omega_0/|\gamma| \quad (47)$$

and

$$H_{xy,0} = 0. \quad (48)$$

Note that the FMR frequency ω_0 for a spherical sample is just equal to $|\gamma|H$.

The spatial averages for the inhomogeneous sample stiffness fields $\langle \tilde{h}_{xx}^2 \rangle$, $\langle \tilde{h}_{yy}^2 \rangle$, $\langle \tilde{h}_{xy}^2 \rangle$, and $\langle \tilde{h}_{xx}\tilde{h}_{yy} \rangle$ involve an analysis based on the cubic magnetocrystalline energy density as developed in general terms in Sec. II C. To the lowest order, cubic symmetry leads to an anisotropy energy density of the form $\tilde{W} = K_1(\alpha_X^2\alpha_Y^2 + \alpha_Y^2\alpha_Z^2 + \alpha_Z^2\alpha_X^2)$, where K_1 is the usual first order magnetocrystalline anisotropy energy density parameter and the $\alpha_{X,Y,Z}$ denote the direction cosines between the magnetization vector $\mathbf{M}(\mathbf{r})$ and the local cubic X , Y , and Z axes in the random crystalline grains. It is useful to define a cubic anisotropy field parameter $H_a = 2K_1/M_s$. The extraction of the spatial average quantities $\langle \tilde{h}_{xx}^2 \rangle$, $\langle \tilde{h}_{yy}^2 \rangle$, $\langle \tilde{h}_{xy}^2 \rangle$, and $\langle \tilde{h}_{xx}\tilde{h}_{yy} \rangle$ is a matter of (1) a careful analysis of energy derivatives for \tilde{W} specified in Sec. II C and (2) proper spatial averaging. McMichael and Krivosik gave the details

of such an analysis for a variety of inhomogeneities in Ref. 14. The needed spatial averages for cubic anisotropy are obtained as

$$\langle \tilde{h}_{xx}^2 \rangle = \langle \tilde{h}_{yy}^2 \rangle = \frac{29}{105} H_a^2, \quad (49)$$

$$\langle \tilde{h}_{xy}^2 \rangle = \frac{9}{105} H_a^2, \quad (50)$$

and

$$\langle \tilde{h}_{xx} \tilde{h}_{yy} \rangle = \frac{11}{105} H_a^2. \quad (51)$$

Note that all terms involve the square of the anisotropy field multiplied by some numerical factor. Other types of anisotropy generally lead to the same form, but with different numerical factors.

Finally, turn to the correlations. A relatively standard choice for the correlation function $C(\mathbf{R})$ is²¹

$$C(\mathbf{R}) = e^{-|\mathbf{R}|/\xi}, \quad (52)$$

where ξ is now a characteristic correlation length that may be associated with the grain size in the polycrystalline sample, for example. The Fourier transform of Eq. (52) yields⁴⁸

$$C_{\mathbf{k}} \equiv C_k = \frac{2\pi^2 f(k)}{V k^2}, \quad (53)$$

with

$$f(k) = \frac{4}{\pi} \frac{\xi^3 k^2}{[1 + (k\xi)^2]^2}. \quad (54)$$

The $f(k)$ nomenclature follows the notation of Ref. 21. Note that $f(k)$ is a steeply peaked function with its maximum at $k = 1/\xi$. In wave number space, $f(k)$ will select out only those Fourier components around this peak position for a strong contribution to the scattering.

The stage is now set for the evaluation of the two magnon relaxation rate from Eq. (35). With the sum over \mathbf{k} replaced by a volume integral over \mathbf{k} space as given above, use of the prescribed homogeneous stiffness fields and the spatially averaged inhomogeneous stiffness field products just listed, the final result is obtained as

$$\begin{aligned} \tilde{\eta}_0 &= \frac{\pi |\gamma|^2 H_a^2}{105} \int_0^\infty dk \int_0^1 d \cos \theta_k f(k) \\ &\times \left[1 + 19 \frac{|\gamma|}{\omega_0} (H_i + Dk^2 + 2\pi M_s \sin^2 \theta_k) \right] \\ &\times \delta(\omega_0 - \omega_{\mathbf{k}}). \end{aligned} \quad (55)$$

Keep in mind that even though this is a 3D problem, the $|\tilde{G}_{0,\mathbf{k}}|$ is independent of the azimuthal spin wave propagation angle ϕ_k . The result in Eq. (55) matches the original result given by Eq. (47b) in Ref. 21. This result has formed much of the basis of the linewidth analysis for dense bulk polycrystalline ferrites from the 1960s. The value of the present rendering of this result is in the step by step and relatively

transparent development directly from Hamiltonian principles.

IV. TWO MAGNON SCATTERING LINEWIDTH IN THIN FILMS

Ferromagnetic resonance in a variety of forms is widely used to determine the uniform mode relaxation or damping rate through linewidth measurements for thin magnetic films in general and metallic films, in particular. It has been well known since the late 1960s, moreover, that two magnon scattering can make significant contributions to these linewidths, as in Ref. 6, for example. In spite of this, the predominant popular approach for most workers has been simply to analyze all data on the basis of a single phenomenological damping parameter based Landau-Lifshitz or Gilbert damping model. While there have been notable exceptions to this phenomenological approach for data analysis, mainly through the working equations from the Arias and Mills theory,¹⁰ as provided in Refs. 8, 27, and 49, for example, there has really been no cogent application of the two magnon theory to a wide range of thin film FMR linewidth data. The purpose of this section is to provide such an application based on the equations developed above and the long standing linewidth data from Ref. 6 for a range of Permalloy film thicknesses and FMR frequencies. These data were obtained for in-plane static fields.

The data from Ref. 6 are analyzed in terms of a simple model that includes three contributions to the relaxation rate: intrinsic magnon-electron scattering, eddy current Ohmic losses, and two magnon scattering. The magnon-electron scattering contribution was analyzed in terms of Gilbert damping.^{50,51}

Within the framework of the Gilbert model, the intrinsic contribution to the uniform mode relaxation rate can be written as

$$\eta_{0,m-e} = \alpha_G \omega_0 P_A, \quad (56)$$

where α_G is the Gilbert damping parameter. The α_G parameter can, in principle, be obtained in terms of the band structure, as discussed in Ref. 50 and elsewhere. For the present purposes, α_G will be used simply as an adjustable parameter. The P_A factor is related to the uniform mode ellipticity and can be expressed as⁵⁰

$$P_A = \frac{|\gamma|}{2\omega_0} (H_{xx,0} + H_{yy,0}) = \frac{\partial \omega_0}{\partial |\gamma| H} \Big|_{\text{FMR}}, \quad (57)$$

where H , as in the last section, is the external static field and the derivative is evaluated at the resonance point. Note that the second equality in Eq. (57) is valid only if the change in static field H does not affect the magnetization static equilibrium. In such a case the P_A factor serves also as a conversion factor between the relaxation rate and the field linewidth.^{52,53}

If the x and y directions are taken to be perpendicular and parallel to the film plane, respectively, one has $H_{xx,0} \approx H + 4\pi M_s$ and $H_{yy,0} \approx H$. The off-diagonal $H_{xy,0}$ stiffness field component for this geometry is zero. The films in Ref. 6 had the usual in-plane uniaxial anisotropy that is typical of field deposited Permalloy films. This has not been included in the

analysis here. Trial calculations that include the anisotropy show no appreciable effect.

Eddy current losses can be particularly pronounced for thicker films and higher frequencies. For a negligible exchange interaction and small dissipation, the eddy current relaxation rate can be written in the same form as Gilbert damping given by Eq. (56) with α_G replaced by^{54,55}

$$\alpha_{ec} = \frac{\pi}{3c^2} \frac{|\gamma| 4\pi M_s}{\rho} d^2. \quad (58)$$

Here, ρ is the electrical resistivity, d is the film thickness, and c is the speed of light.

The final and critical contribution to the relaxation rate and the FMR linewidth for this discussion is the two magnon contribution due to inhomogeneities, based on the formalism in Sec. II. For in-plane magnetized high magnetization thin films and relatively low frequency ferromagnetic resonance, the degenerate nonuniform modes have relatively low \mathbf{k} values. In this case, the approximations discussed in Sec. II F are applicable.²⁷

If one further assumes that the inhomogeneous stiffness fields do not differ significantly from each other, one can write $\langle \tilde{h}_{xx}^2 \rangle \approx \langle \tilde{h}_{yy}^2 \rangle \equiv \langle \tilde{h}^2 \rangle$. In this case Eq. (42) is simplified to

$$\tilde{\eta}_0 \approx \pi |\gamma|^2 \langle \tilde{h}^2 \rangle C_0 P_A^2 g(\omega_0). \quad (59)$$

For a very thin film, moreover, the dynamic magnetization does not vary significantly across the film thickness. In this uniform magnetization mode approximation, the calculation of the density of states function $g(\omega_0)$ may be reduced to a two dimensional \mathbf{k} -space formulation for in-plane propagating modes and may be rewritten as

$$g(\omega_0) = \sum_{\mathbf{k}} \delta(\omega_0 - \omega_{\mathbf{k}}) \approx \frac{A}{(2\pi)^2} \int \delta(\omega_0 - \omega_{\mathbf{k}}) d\mathbf{k}, \quad (60)$$

where A is the film area. The integration in Eq. (60) may be evaluated analytically for the ultrathin film limit.^{14,16} In such a case the result does not depend on the film thickness. Here, however, numerical integration has been used, with the full spin wave dispersion $\omega_{\mathbf{k}}$ taken in the uniform magnetization mode approximation.^{14,42} This dispersion can be expressed through $\omega_{\mathbf{k}} = |\gamma| \sqrt{H_{xx,\mathbf{k}} H_{yy,\mathbf{k}}}$, with the homogeneous spin wave stiffness fields given as

$$H_{xx,\mathbf{k}} = H + Dk^2 + 4\pi M_s N_k(kd) \quad (61)$$

and

$$H_{yy,\mathbf{k}} = H + Dk^2 + 4\pi M_s \sin^2 \theta_k [1 - N_k(kd)]. \quad (62)$$

Here, θ_k is now the angle between the in-plane spin wave \mathbf{k} vector and the direction of the external static field H . The ultrathin film dipole field function N_k is given by $N_k = (1 - e^{-kd})/kd$. Finally, a two dimensional Fourier transform of the correlation function given by Eq. (52) in the $\mathbf{k}=0$ limit yields $C_0 \approx 2A_\xi/A$, where A_ξ is a mean inhomogeneity area.

Based on the above working equations, the total relaxation rate may be written as

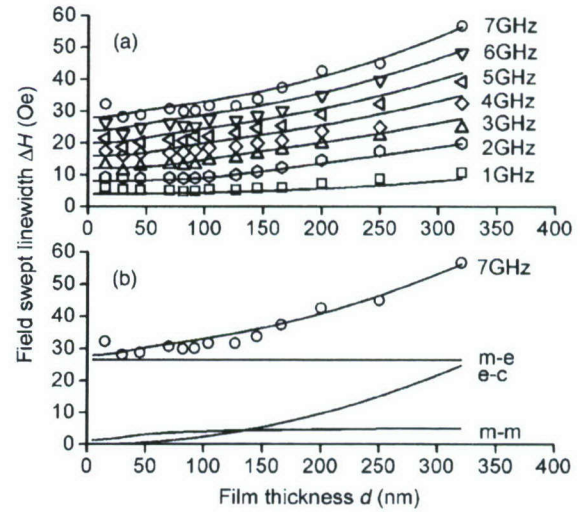


FIG. 1. Field swept linewidth ΔH as a function of film thickness d for a series of $\text{Ni}_{77}\text{Fe}_{23}$ thin films. Graph (a) shows data from Ref. 6 at specified frequencies indicated by the various symbols. The solid lines represent fits of Eq. (64) to the data with fitting parameters as given in the text. Graph (b) shows data and fit results at 7 GHz, along with a breakdown of the component eddy current (ec), magnon-electron (m-e), and two magnon (m-m) contributions to the linewidth, as indicated.

$$\eta_0 = (\alpha_G + \alpha_{ec}) \omega_0 P_A + K P_A^2 \int \delta(\omega_0 - \omega_{\mathbf{k}}) d\mathbf{k}, \quad (63)$$

where $K \approx 0.16 |\gamma|^2 \langle \tilde{h}^2 \rangle A_\xi$. Note that the specific numerical factor in the parameter K will depend on the choice of correlation function. Other than this, the form above for the total relaxation rate can be taken as fairly general, subject to the limits already noted.

The field swept FMR linewidth ΔH is then given as

$$\Delta H(\omega_0, d) = \frac{2\eta_0}{|\gamma| P_A} = \frac{2}{|\gamma|} [\alpha_G + \alpha_{ec}(d)] \omega_0 + \frac{2K}{|\gamma|} P_A(\omega_0) \int \delta[\omega_0 - \omega_{\mathbf{k}}(d)] d\mathbf{k}. \quad (64)$$

Equation (64) has been written in such a form as to keep all dependences on the FMR frequency ω_0 and film thickness d explicit.

Figures 1 and 2 summarize the field linewidth data from the published graphs in Ref. 6 for a series of Permalloy films, along with corresponding fit results based on the above working equations. Graph (a) in Fig. 1 shows the half power field swept linewidth ΔH as a function of film thickness d for the indicated frequencies. The various symbols show the data and the solid curves show the fits. Graph (b) shows the data and fit for 7 GHz only, along with a breakdown of the component eddy current (ec), magnon-electron (m-e), and two magnon (m-m) contributions to the linewidth, as indicated. Figure 2 shows the corresponding results for three of the films in a linewidth versus frequency (f) format.

The fitting was done in a general way, with common material and structure parameters used for all the films. The focus was on the realization of a reasonable overall fit that adequately demonstrates the overall trend of the data rather than a point-by-point matchup. The curves shown were ob-

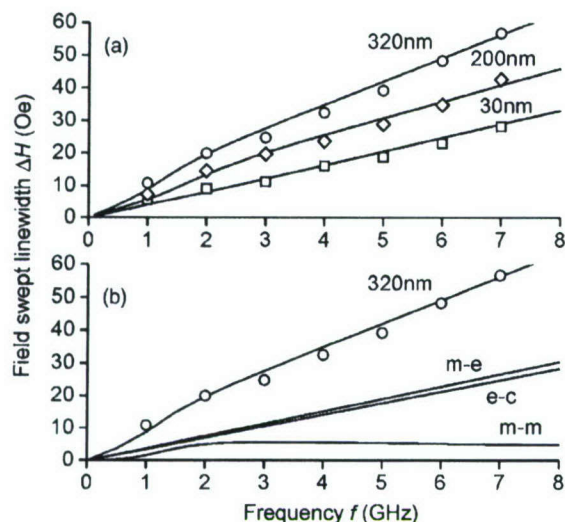


FIG. 2. Field swept linewidth ΔH as a function of frequency f for a series of $\text{Ni}_{77}\text{Fe}_{23}$ thin films. Graph (a) shows data from Ref. 6 at specified thicknesses indicated by the various symbols. The solid lines represent fits of Eq. (64) to the data with fitting parameters as given in the text. Graph (b) shows data and fit results for the 320 nm thick film along with a breakdown of the component eddy current (e-c), magnon-electron (m-e), and two magnon (m-m) contributions to the linewidth, as indicated.

tained for $4\pi M_s = 10$ kG, $|\gamma|/2\pi = 2.9$ MHz/Oe, $\alpha_G = 0.0057$, $\rho = 3415$ s [$38 \mu\Omega$ cm in Systeme International (SI) units], and $\langle \tilde{h}^2 \rangle A_\xi = 9 \times 10^{-9}$ Oe² cm². The ρ value needed to fit the data is somewhat higher than the typical literature values 15–25 $\mu\Omega$ cm for Permalloy.⁵⁶ The $\langle \tilde{h}^2 \rangle A_\xi$ appear reasonable. For an average characteristic inhomogeneity length, $\xi \approx 50$ nm, that corresponds to nominal Permalloy film grain sizes for the deposition conditions in Ref. 6, one obtains a reasonable inhomogeneity field $|\tilde{h}|$ value of about 10 Oe.

One can see that the fits generally replicate the trends of the data in both graphs. Keep in mind that the combination of eddy current damping and magnon-electron damping alone would give only a linewidth that scales linearly with frequency and quadratically with film thickness. Both the data and the fits provide convincing evidence for an additional two magnon component with more complicated d and f dependences. These dependences come from the variation in the density of states for the two magnon scattering. The breakdowns in Figs. 1(b) and 2(b) show these effects. Note, in particular, the small but distinct m-m components in the (b) graphs in both figures. The scatter in the data in Fig. 1 is too large to see the two magnon effect on the response as clearly as one might like, but the overall trend, especially in graph (a), provides reasonably convincing evidence of such a response. The two magnon knee can be discerned somewhat more clearly in Fig. 2.

Considered overall, the data, the fits, and the breakdowns demonstrate fairly clearly the role of the two magnon scattering contribution to the Permalloy film in the linewidth. In spite of the fairly basic simplified model used here, mainly for the sake of simplicity of analysis, the quantitative as well as qualitative match of the theory to the entire ensemble of data for a single set of fitting parameters is remarkable.

V. SUMMARY AND CONCLUSIONS

In summary, this work presents a compact but complete synopsis of two magnon scattering theory done within the framework of the Hamiltonian formalism. It provides general expressions for the inhomogeneity coupling coefficients in the case of localized inhomogeneities. The key ideas may be extended to nonlocal scattering without any modification in the formalism. At the present stage, the theory is applicable to problems where the nonuniform magnetization excitations can be described as plane wave modes. In principle, other types of normal mode expansions could be used in place of the plane waves, but such modifications will, by necessity, significantly expand the amount of algebra. For practical purposes, the plane wave approach as presented appears to be adequate for most material systems of technological interest.

By way of example, two specific applications of the theory are presented. The first involves a representative calculation of the two magnon scattering relaxation rate for anisotropy scattering in bulk polycrystalline spheres. It is shown that the result obtained from the Hamiltonian approach matches exactly the classic solution from Ref. 21. In the second example, previously published FMR linewidth data versus film thickness and frequency for thin NiFe films have been analyzed on the basis of the working TMS equations developed here from the Hamiltonian formalism. It is shown that the theory provides results that are in reasonable agreement with the data.

ACKNOWLEDGMENTS

This work was supported in part by the U.S. Army Research Office, Grant No. W911NF-04-1-0247 (MURI), the Office of Naval Research, Grant No. N00014-06-1-0889, and the Information Storage Industry Consortium (INSIC) Extremely High Density Recording (EHDR) program.

APPENDIX

This appendix provides a roadmap for the evaluation of homogeneous stiffness field tensor introduced in Sec. II B. The analysis starts from the magnetic energy \mathcal{H} written in the form

$$\mathcal{H} = - \int_V \mathbf{M}(\mathbf{r}, t) \cdot \mathbf{H}_{\text{ext}}(\mathbf{r}, t) d^3r - \frac{1}{2} \int_V \mathbf{M}(\mathbf{r}, t) \cdot \mathbf{H}_{\mathbf{M}}(\mathbf{r}, t) d^3r. \quad (\text{A1})$$

Here, the first term represents the Zeeman energy that derives from the interaction of the magnetization with an *external* magnetic field $\mathbf{H}_{\text{ext}}(\mathbf{r}, t)$. The second term represents the interaction energy of the magnetization with the separate and distinct *internal* magnetic self-field $\mathbf{H}_{\mathbf{M}}(\mathbf{r}, t)$. This field is assumed to be a *linear* functional of the magnetization $\mathbf{M}(\mathbf{r}, t)$. Examples of such internal fields include the Maxwellian dipole field, the non-Maxwellian macroscopic exchange field, and the non-Maxwellian effective field associated with a uniaxial anisotropy. Other self-fields that are given by higher order functionals of the magnetization, such

as an effective field due to cubic anisotropy, for example, may be incorporated into a linearized form through an appropriate Taylor expansion. It is important to keep in mind that the magnetization response in the small signal limit is fully described by a Hamiltonian that contains powers of the magnetization up to the second order alone.

For simplicity, take $\mathbf{H}_{\text{ext}}(\mathbf{r}, t) = H\hat{\mathbf{z}}$ as a spatially homogeneous static field. Within the plane wave approximation, the spatial dependences of $\mathbf{M}(\mathbf{r}, t)$ and $\mathbf{H}_{\mathbf{M}}(\mathbf{r}, t)$ in Eq. (A1) can be expanded in the Fourier series according to

$$\mathbf{M}(\mathbf{r}, t) = \sum_{\mathbf{k}} \mathbf{M}_{\mathbf{k}}(t) e^{i\mathbf{k} \cdot \mathbf{r}} \quad (\text{A2})$$

and

$$\mathbf{H}_{\mathbf{M}}(\mathbf{r}, t) = \sum_{\mathbf{k}} \mathbf{H}_{\mathbf{M}, \mathbf{k}}(t) e^{i\mathbf{k} \cdot \mathbf{r}}. \quad (\text{A3})$$

From the linearity of the Fourier transform, it follows that the Fourier components $\mathbf{H}_{\mathbf{M}, \mathbf{k}}$ will depend linearly on $\mathbf{M}_{\mathbf{k}}$. For a *spatially homogeneous sample* one can write this dependence as

$$\mathbf{H}_{\mathbf{M}, \mathbf{k}}(t) = -4\pi \hat{\mathbf{N}}_{\mathbf{k}} \cdot \mathbf{M}_{\mathbf{k}}(t), \quad (\text{A4})$$

where $\hat{\mathbf{N}}_{\mathbf{k}}$ is a 3×3 spin wave tensor. The factor -4π is chosen to give a form for $\mathbf{H}_{\mathbf{M}, \mathbf{k}}$ that resembles expressions for the demagnetization fields of a homogeneously magnetized ellipsoid. The components of the $\hat{\mathbf{N}}_{\mathbf{k}}$ tensor, namely, $N_{ij, \mathbf{k}}$ ($i, j = x, y, z$), depend on the specific type of the internal magnetic field. If the form of the energy is known, these components can be readily evaluated. For example, for exchange, one has a simple functional for the corresponding effective exchange field, $\mathbf{H}_{\text{exch}}(\mathbf{r}, t) \propto \nabla^2 \mathbf{M}(\mathbf{r}, t)$. This corresponds, in turn, to a spin wave tensor $\hat{\mathbf{N}}_{\mathbf{k}}^{\text{exch}} \propto k^2 \mathbf{I}$, where \mathbf{I} is a unitary matrix. Insertion of Eqs. (A2)–(A4) into Eq. (A1) yields a homogeneous sample magnetic energy of the form

$$\mathcal{H}_{\text{hom}} = -V H M_{z,0} + V \frac{4\pi}{2} \sum_{\mathbf{k}} \mathbf{M}_{\mathbf{k}}^{*T} \cdot (\hat{\mathbf{N}}_{\mathbf{k}} \cdot \mathbf{M}_{\mathbf{k}}). \quad (\text{A5})$$

Since the energy in Eq. (A5) is real, one can show that $N_{ij, \mathbf{k}} = N_{ji, \mathbf{k}} = N_{ij, \mathbf{k}}^*$ is satisfied.

The M_z component of the magnetization can be eliminated from Eq. (A5) with the use of a small signal limit approximation, $M_z \approx M_s - (M_x^2 + M_y^2)/2M_s$. The quadratic part of the energy in Eq. (A5) then includes terms that are quadratic in $M_{x, \mathbf{k}}$ and $M_{y, \mathbf{k}}$. This quadratic part of the energy can be written as

$$\mathcal{H}_{\text{hom}}^{(2)} = \frac{V}{2M_s} \sum_{\mathbf{k}} (M_{x, \mathbf{k}}^* M_{y, \mathbf{k}}^*) \cdot \begin{pmatrix} H_{xx, \mathbf{k}} & H_{xy, \mathbf{k}} \\ H_{xy, \mathbf{k}} & H_{yy, \mathbf{k}} \end{pmatrix} \cdot \begin{pmatrix} M_{x, \mathbf{k}} \\ M_{y, \mathbf{k}} \end{pmatrix}, \quad (\text{A6})$$

where the components of the homogeneous stiffness field tensor are given as

$$H_{jj, \mathbf{k}} = H_i + 4\pi M_s N_{jj, \mathbf{k}} \quad (jj = xx, yy) \quad (\text{A7})$$

and

$$H_{xy, \mathbf{k}} = 4\pi M_s N_{xy, \mathbf{k}}, \quad (\text{A8})$$

where $H_i = H - 4\pi M_s N_{zz,0}$ is the internal static field. As a final step, the expression in Eq. (A6) can be transformed into the form in Eq. (12) by means of the connections in Eq. (5) taken in the small signal limit according to $iM_{x, \mathbf{k}} + M_{y, \mathbf{k}} \approx \sqrt{2} M_s a_{\mathbf{k}}$.

¹D. L. Mills and S. M. Rezende, in *Spin Dynamics in Confined Magnetic Structures II*, edited by B. Hillebrands and K. Oundjela (Springer-Verlag, Berlin, 2003).

²M. Sparks, *Ferromagnetic Relaxation Theory* (McGraw-Hill, New York, 1964).

³R. C. LeCraw, E. G. Spencer, and C. S. Porter, *Phys. Rev.* **110**, 1311 (1958).

⁴C. R. Buffler, *J. Appl. Phys.* **30**, S172 (1959).

⁵A. K. Srivastava, M. J. Hurben, C. E. Patton, M. A. Wittenauer, P. Kabos, R. Ramesh, P. C. Dorsey, and D. B. Chrisey, *J. Appl. Phys.* **85**, 7838 (1999).

⁶C. E. Patton, C. H. Wills, and F. B. Humphrey, *J. Appl. Phys.* **38**, 1358 (1967).

⁷S. J. Yuan, L. Sun, H. Sang, J. Du, and S. M. Zhou, *Phys. Rev. B* **68**, 134443 (2003).

⁸K. Lenz, H. Wende, W. Kuch, K. Baberschke, K. Nagy, and A. Janossy, *Phys. Rev. B* **73**, 144424 (2006).

⁹M. Sparks, R. Loudon, and C. Kittel, *Phys. Rev.* **122**, 791 (1961).

¹⁰P. E. Seiden and M. Sparks, *Phys. Rev.* **137**, A1278 (1965).

¹¹R. D. McMichael and A. Kunz, *J. Appl. Phys.* **91**, 8650 (2002).

¹²C. W. Hass and H. B. Callen, in *Magnetism I*, edited by G. T. Rado and H. Suhl (Academic, New York, 1963).

¹³J. F. Cochran, R. W. Qiao, and B. Heinrich, *Phys. Rev. B* **39**, 4399 (1989).

¹⁴R. D. McMichael and P. Krivosik, *IEEE Trans. Magn.* **40**, 2 (2002).

¹⁵A. M. Clogston, H. Suhl, L. R. Walker, and P. W. Anderson, *J. Phys. Chem. Solids* **1**, 129 (1956).

¹⁶R. Arias and D. L. Mills, *Phys. Rev. B* **60**, 7395 (1999).

¹⁷A. Kunz and R. D. McMichael, *IEEE Trans. Magn.* **38**, 2400 (2003).

¹⁸R. D. McMichael, D. J. Twisselmann, and A. Kunz, *Phys. Rev. Lett.* **90**, 227601 (2003).

¹⁹E. Schlömann, *Phys. Rev.* **182**, 632 (1969).

²⁰K. Motizuki, M. Sparks, and P. E. Seiden, *Phys. Rev.* **140**, A972 (1965).

²¹E. Schlömann, *J. Phys. Chem. Solids* **6**, 242 (1958).

²²M. Sparks, *Phys. Rev. B* **1**, 3856 (1970).

²³M. J. Hurben and C. E. Patton, *J. Appl. Phys.* **83**, 4344 (1998).

²⁴P. E. Wigen, *Phys. Rev.* **133**, A1557 (1964).

²⁵R. E. DeWames and T. Wolfram, *J. Appl. Phys.* **41**, 987 (1970).

²⁶B. A. Kalinikos and A. N. Slavin, *J. Phys. C* **19**, 7013 (1986).

²⁷J. Lindner et al., *Phys. Rev. B* **68**, 060102 (2003).

²⁸R. D. McMichael, D. J. Twisselmann, J. E. Bonevich, A. P. Chen, W. F. Egelhoff, and S. E. Russek, *J. Appl. Phys.* **91**, 8647 (2002).

²⁹A. Yu. Dobin and R. H. Victora, *Phys. Rev. Lett.* **92**, 257204 (2004).

³⁰B. B. Maranville, J. Mallett, T. P. Moffat, R. D. McMichael, A. P. Chen, and W. F. Egelhoff, *J. Appl. Phys.* **97**, 10A721 (2005).

³¹E. Schlömann, *Ferromagnetic Resonance at High Power Levels*, Research Division, Raytheon Company Technical Report No. R-48, 1959 (unpublished).

³²V. S. L'vov, *Wave Turbulence under Parametric Excitation* (Springer-Verlag, Berlin, 1994).

³³G. A. Melkov, Yu. V. Kobljanskyj, A. A. Serga, V. S. Tiberkevich, and A. N. Slavin, *Phys. Rev. Lett.* **86**, 4918 (2001).

³⁴G. A. Melkov, V. I. Vasyuchka, Yu. V. Kobljanskyj, and A. N. Slavin, *Phys. Rev. B* **70**, 224407 (2004).

³⁵H. Suhl, *J. Appl. Phys.* **30**, 1961 (1959).

³⁶G. de Loubens, V. V. Naletov, and O. Klein, *Phys. Rev. B* **71**, 180411(R) (2005).

³⁷E. Schlömann, *Phys. Rev.* **116**, 828 (1959).

³⁸V. E. Zakharov, V. S. L'vov, and S. S. Starobinets, *Sov. Phys. Usp.* **17**, 896 (1975).

³⁹A. N. Slavin and I. V. Rojdstvenski, *IEEE Trans. Magn.* **30**, 37 (1994).

⁴⁰V. L. Safonov and H. N. Bertram, *J. Appl. Phys.* **93**, 6912 (2003).

⁴¹A. Yu. Dobin and R. H. Victora, *Phys. Rev. Lett.* **90**, 167203 (2003).

⁴²K. J. Harte, *J. Appl. Phys.* **39**, 1503 (1968).

⁴³R. M. White, *Quantum Theory of Magnetism* (Springer-Verlag, New York, 1970).

- ⁴⁴V. L. Safonov, J. Appl. Phys. **91**, 8653 (2002).
- ⁴⁵A. G. Gurevich and G. A. Melkov, *Magnetization Oscillations and Waves* (CRC, New York, 1996).
- ⁴⁶R. D. McMichael, M. D. Stiles, P. J. Chen, and W. F. Egelhoff, Jr., J. Appl. Phys. **83**, 7037 (1998).
- ⁴⁷T. Holstein and H. Primakoff, Phys. Rev. **58**, 1098 (1940).
- ⁴⁸Yu. A. Brychkov, *Multidimensional Integral Transformations* (Gordon and Breach, Philadelphia, 1992).
- ⁴⁹A. Azevedo, A. B. Oliveira, F. M. de Aguiar, and S. M. Rezende, Phys. Rev. B **62**, 5331 (2000).
- ⁵⁰V. Kambersky and C. E. Patton, Phys. Rev. B **11**, 2668 (1975).
- ⁵¹L. Berger, J. Phys. Chem. Solids **38**, 1321 (1977).
- ⁵²S. S. Kalarickal, P. Krivosik, M. Wu, C. E. Patton, M. L. Schneider, P. Kabos, T. J. Silva, and J. P. Nibarger, J. Appl. Phys. **100**, 084905 (2006).
- ⁵³B. Kuanr, R. Camley, and Z. Celinski, Appl. Phys. Lett. **87**, 012502 (2005).
- ⁵⁴D. O. Smith, in *Magnetism III*, edited by G. T. Rado, and H. Suhl (Academic, New York, 1963).
- ⁵⁵A. Magni, G. Bertotti, I. D. Mayergoyz, and C. Serpico, Physica B **306**, 121 (2005).
- ⁵⁶A. F. Mayadas, J. F. Janak, and A. Gangulee, J. Appl. Phys. **45**, 2780 (1974).

Magnetic properties and structural implications for nanocrystalline Fe-Ti-N thin films

Jaydip Das, Sangita S. Kalarickal, Kyoung-Suk Kim, and Carl E. Patton

Department of Physics, Colorado State University, Fort Collins, Colorado 80523, USA

(Received 3 October 2006; revised manuscript received 25 January 2007; published 29 March 2007)

The magnetization and ferromagnetic resonance (FMR) profiles have been measured for a series of soft-magnetic nanocrystalline Fe-Ti-N films. Magnetization (M) measurements were made as a function of temperature (T) from 2 to 300 K and in-plane field (H) up to 1 kOe. Additionally, room temperature easy and hard direction in-plane field hysteresis loops were measured for fields between ± 100 Oe, and 10 GHz FMR measurements were performed. The 50 nm thick films were made by magnetron sputtering in an in-plane field. The nominal titanium concentration was 3 at. % and the nitrogen concentrations (x_N) ranged from 0 to 12.7 at. %. The saturation magnetization (M_s) vs T data and the extracted exchange parameters as a function of x_N are consistent with a lattice expansion due to the addition of interstitial nitrogen in the body-centered-cubic (bcc) lattice and a structural transition to body-centered-tetragonal (bct) in the 6–8 at. % nitrogen range. The hysteresis loop and FMR data show a consistent picture of the changes in both the uniaxial and cubic anisotropy as a function of x_N . Films with $x_N \geq 3.9$ at. % show an overall uniaxial anisotropy, with an anisotropy field parameter H_u that increases with x_N . The corresponding dispersion averaged uniaxial anisotropy energy density parameter $\langle K_u \rangle = H_u M_s / 2$ is a linear function of x_N , with a rate of increase of 950 ± 150 erg/cm³ per at. % nitrogen. The estimated uniaxial anisotropy energy per nitrogen atom is 30 J/mol, a value consistent with other systems. For x_N below 6 at. %, the scaling of coercive force H_c data with the sixth power of the grain size D indicate a grain averaged effective cubic anisotropy energy density parameter $\langle K_1 \rangle$ that is about an order of magnitude smaller than the nominal $\langle K_1 \rangle$ values for iron, and give a quantitative $\langle K_1 \rangle$ vs D response that matches predictions for exchange coupled random grains with cubic anisotropy.

DOI: 10.1103/PhysRevB.75.094435

PACS number(s): 75.30.Cr, 75.30.Gw, 76.50.+g

I. INTRODUCTION

The nanocrystalline Fe-Q-N thin film system, with Q = Al, Ti, Ta, or Zr, for example, has been a subject of great interest over the last decade or so.^{1–10} This interest has been driven, in part by the seminal work on binary Fe-N films by Kim and Takahashi,¹¹ who were the first to show that the addition of nitrogen appears to give a magnetization higher than pure iron, even at small nitrogen levels. While the nitrogen is generally taken to reside on interstitial sites and result in an expansion of the iron lattice,¹² the actual effect of the nitrogen atoms on the magnetization is still a matter of controversy.^{13–15} The shift in interest to the three element Fe-Q-N film system has been driven by the realization that small amounts of the third element can provide an enhanced thermal stability.^{16,17} In addition to the challenges to understand the fundamental magnetic properties of Fe-Q-N films, the system shows a number of attractive properties for microwave device and magnetic information storage applications. These include large magnetization, field-induced uniaxial anisotropy, high permeability, low coercive force, and low microwave loss.

The recent work by Alexander and co-workers on the Fe-Ti-N film systems, as cited above, has shown evidence for a low microwave loss with strong microstructure correlations.^{8,9} Work from this group has also provided concise data on structure, room temperature magnetization, and anisotropy.^{5–7,10} Apart from these studies, however, there has been very little definitive work to elucidate the magnetic interactions, identify structural transitions, and changes in the magnetic properties associated with these transitions, or to separate the different contributions to the magnetic anisotropy.

The purpose of this work was to perform a comprehensive study of the fundamental magnetic properties of the Fe-Ti-N film system. This has been done for a range of nitrogen concentrations from 0–13 at. %, the range over which most of the interesting and useful property changes occur. Three types of measurements were made, magnetization vs temperature from 2 to 300 K at a fixed field of 1 kOe, hysteresis loops for fields from –100 to +100 Oe at 300 K, and room temperature field swept ferromagnetic resonance (FMR) at 9.5 GHz. All data were for in-plane fields only.

The different types of data all indicate some sort of a structural transition in the 6–8 at. % nitrogen range. This applies to the effective exchange as extracted from the magnetization vs temperature data, the coercive force data, and the cubic and uniaxial anisotropy parameters obtained from the hysteresis loop and the FMR data. There is a clear transition from cubic anisotropy dominance to uniaxial anisotropy dominance in the same 6–8 at. % nitrogen range.

The paper is organized as follows: Section II provides a brief overview of the structure and magnetic properties of the Fe-N and Fe-Q-N film systems. Section III gives a description of the film materials and the magnetization and microwave measurement procedures. Section IV presents magnetization vs temperature data and an analysis of the data in terms of effective exchange parameters. Section V presents the room temperature microwave and hysteresis loop data, summarizes results on the coercive force, and shows a qualitative analysis of the data in terms of cubic and uniaxial anisotropy. Section VI elucidates the dependence of derived cubic and uniaxial anisotropy energy density parameters on nitrogen content, based on the data presented in Sec. V, and examines the ferromagnetic exchange length implications for these nanocrystalline films.

II. OVERVIEW OF THE Fe-N AND Fe-Q-N FILM SYSTEMS

The introduction gave a brief overview of Fe-N and Fe-Q-N thin films, with an emphasis on magnetic properties. This section focuses on structure. For the film thicknesses of interest here, typically in the 50 nm range, no special thickness effects are expected and only bulk structure considerations are needed. The available literature indicates that as one adds nitrogen, there are progressive changes in structure.¹⁸ One starts with body-centered-cubic (bcc) α -Fe and a saturation induction $4\pi M_s$ of about 21 kG. For $\text{Fe}_{1-x_N}\text{N}_{x_N}$, with a nitrogen content x_N up to 0.4 at. % or so, the nitrogen atoms can be dissolved in the bcc lattice with essentially no change in the structure.^{18,19} It is important to emphasize that the nitrogen enters the bcc lattice interstitially and the x_N parameter here simply denotes the atomic fraction of the nitrogen in the overall material.

As one moves above $x_N \approx 0.4$ at. %, the interstitial nitrogen becomes sufficient to produce a tetragonally distorted α' -Fe-N phase. At some level between $x_N \approx 0.4$ at. % and $x_N \approx 11$ at. %, the literature indicates an overall structure change to a body-centered-tetragonal (bct) α'' -Fe-N phase.¹⁸ Reported values of the saturation induction of the α'' phase vary over a wide range, typically from 20 to 30 kG or so.^{13-15,20} Neither the details on this bcc-bct transition point nor the problem with the wide variance in $4\pi M_s$ have been resolved to date. Above $x_N \approx 11$ at. %, there appears to be a transition to a face-centered-cubic (fcc) γ' -Fe-N phase with the nitrogen atoms at interstitial octahedral sites. At about $x_N \approx 25$ at. %, one further structural change gives rise to a hexagonal-closed-packed ϵ -Fe-N phase. Finally, for $x_N \approx 50$ at. %, the orthorhombic ζ -Fe-N phase forms.¹²

Even though the sequences of changes summarized above produce interesting phase transitions and potentially useful magnetic properties in some regimes, the metastability of these binary Fe-N phases^{18,21} limits the practical use of these films. It has been found that the addition of small amounts of a third element Q to form ternary Fe- Q -N phases, typically Hf, Ta, Ti, or Zr, can serve to increase thermal stability.^{4,16,17} For pure iron, additions of such a Q element at levels up to about 5 at. % have been found to dissolve substitutionally into the bcc lattice with no substantial effect on the structure or magnetic properties.³ Similar levels of substitution for these elements in the Fe-N system also appear to have little effect except for the enhanced thermal stability. This is one reason for the focus on Fe-Ti-N films in this work. The distorted bcc to bct structural transition noted above for the Fe-N film system also appears to be operative for Fe-Ti-N films. Data in Ref. 6, for example, indicate that films with about 3 at. % Ti, have a structural transition at about $x_N \approx 7$ at. %.

By way of example, Fig. 1 shows schematic crystal structure diagrams for (a) bcc iron and (b) tetragonally distorted bcc iron with an interstitial nitrogen atom in place, as indicated. The shaded circle in each diagram serves to indicate the possible presence of iron site titanium atoms in the overall Fe-Ti-N structure. The labels indicate nominal atom spacings. The nonparentheses and parentheses values in (a) are for pure bcc iron and Fe-Ti with about 3 at. % titanium,

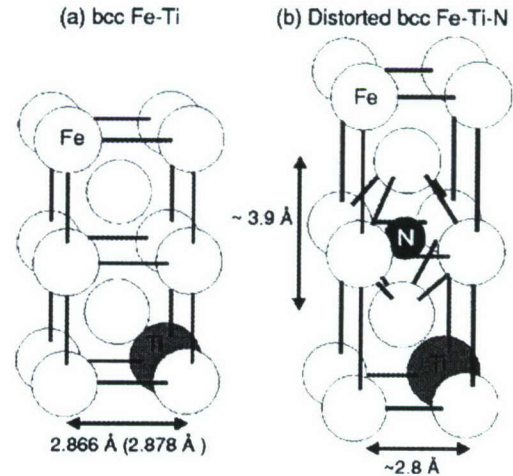


FIG. 1. Schematic illustrations of (a) the bcc iron structure and (b) the tetragonally distorted bcc Fe-N structure for about 5 at. % nitrogen. The shaded atoms indicate possible titanium additions. The separation distances in (a) are for pure iron (nonparentheses) and iron with about 3 at. % titanium (parentheses). The separation distances in (b) are estimated values for Fe-N with about 5 at. % nitrogen and no structural transition to bct.

respectively. The values in (b) are estimates for Fe-N with $x_N \approx 5$ at. %, under the assumption that there is no phase transition to bct at this level.

Overall, Fig. 1 shows two things. First, the addition of nitrogen to the bcc Fe or Fe-Ti system causes a tetragonal distortion to the lattice. Second, the titanium, if present, resides on iron sites. The choice to place a single interstitial nitrogen atom on the lattice diagram in Fig. 1(b) is simply for purposes of illustration. As noted above, one can have a tetragonally distorted bcc structure at low x_N levels or a bonafide body-centered-tetragonal structure for high x_N levels.¹⁸ Insofar as no unit cell is indicated, the (b) diagram could actually apply to either of these situations. The main point of Fig. 1(b) is that the addition of nitrogen breaks the cubic symmetry. One should notice that the interstitial nitrogen in the (b) diagram serves to push away the two nearest-neighbor iron atoms.¹² It is this symmetry breaking effect that can lead to a uniaxial magnetic anisotropy in field deposited alloys or films.

The additional point to be drawn from the figure concerns the bcc site titanium. It was noted above that the Fe-N system with interstitial nitrogen is generally unstable and that the presence of bcc site titanium atoms serves to stabilize the Fe-N system. This is believed to occur because the increase in the lattice parameter caused by the larger titanium atom increases the space available for the interstitial nitrogen.¹⁰ The data show that for small levels of Ti, this makes for a more stable alloy.

The role of the nitrogen in modifying the magnetic anisotropy in Fe-Ti-N films is one of the main aspects of this paper. The body-centered-cubic Fe-Ti alloy has cubic anisotropy. As nitrogen is added to the lattice, there is a decrease in the cubic anisotropy, up to the structural transition to bct at $x_N \approx 7$ at. %.⁷ The nitrogen induced distortion in the lattice might be one possible reason for this decrease. Above the

$x_N \approx 7$ at. % structural transition point, the cubic anisotropy is essentially zero.

There is no literature data available on the effect of nitrogen on the field induced uniaxial anisotropy in Fe-Ti-N films. For Fe-Ta-N and Fe-Zr-N films, deposition in an in-plane field produces a uniaxial anisotropy that increases with x_N .^{22,23} One can presume that this is a pair ordering effect. One can also speculate that Fe-Ti-N films should show a similar response. It seems clear that the symmetry breaking due to the nitrogen, first in producing a tetragonally distorted bcc lattice at low x_N levels and then in producing a bonafide bct structure at higher levels, should produce such an anisotropy when a field is used to promote a preferred direction in the overall polycrystalline film.

One of the key results from the present work is a clear map of the change in the anisotropy, both cubic and uniaxial, as a function of the nitrogen level in the Fe-Ti-N system. Based on the above, one would expect to see a drop in the cubic anisotropy to zero as one goes from Fe-Ti to Fe-Ti-N with $x_N \approx 7$ at. %. At the same time, one should see an increase in the uniaxial anisotropy component, and this anisotropy will become dominant as the alloy changes to bct for $x_N > 7$ at. % or so. One can also speculate that these anisotropy changes will be accompanied by signature changes in the magnetization. Data from the literature do show that the magnetization drops as x_N is increased.⁵ There has been no work that demonstrates any connection between the structural change induced effects on the anisotropy with related effects on the magnetization. The data given below will demonstrate such connections.

In addition to structural changes, the presence of nitrogen affects the grain-growth process in Fe-Ti-N films. Transmission electron microscopy data on films similar to those used in this work indicate a decrease in grain size from about 28 nm at $x_N = 0$ to 4 nm at $x_N \approx 12.7$ at. %.^{8,9} This effect is relevant to the present work because the hysteresis loop properties depend on microstructure as well as anisotropy. References 8 and 9 also show a connection between grain size and the FMR linewidth. However, it is not clear that the linewidth effect is related to grain size or to a structural change. The hysteresis loop data below will make a case for correlations with both structure and grain size.

III. FILM PREPARATION AND MEASUREMENT TECHNIQUES

The samples were kindly provided by Alexander of the University of Alabama MINT Center. The film preparation and the materials analysis work was done by Ding and Alexander. The nanocrystalline Fe-Ti-N films of nominal 50 nm thickness were prepared on glass substrates in a nitrogen-argon atmosphere by dc magnetron sputtering from Fe-Ti alloy targets with a nominal titanium content of about 5 at. %. A 300 Oe static magnetic field was applied in the plane of the substrate to define a specific axis for the possible development of the field induced uniaxial anisotropy. For purposes of discussion this direction will be termed the "easy" direction, even for films with no uniaxial anisotropy. The films were then removed from the deposition system and

annealed at 100 °C in an easy axis oriented 300 Oe field. The atomic concentrations of the different elements were measured by x-ray photoelectron spectroscopy (XPS). All films had about 3 at. % of titanium. The noted difference in titanium content between the target and the film for sputtering in an argon-nitrogen atmosphere is consistent with that reported in Ref. 10. The nitrogen content x_N varied from zero to 12.7 at. %. Grain sizes were determined by transmission electron microscopy (TEM). The nitrogen content and average grain sizes of various films are listed in Table I. Further details are given in Refs. 6 and 8.

The magnetization measurements were made as a function of temperature and magnetic field with a superconducting quantum interference device (SQUID) magnetometer. The fields were always applied in-plane. Prior to the SQUID measurements, FMR measurements as a function of the in-plane field direction were used to ascertain the easy and hard axes for the films with uniaxial anisotropy. The details of the FMR measurements are given below. Three types of magnetization data were then obtained. First, full magnetization vs field hysteresis loop data were obtained for easy direction in-plane fields from -100 to +100 Oe at 300 K. Fields of 100 Oe were found to be adequate to achieve magnetic saturation in all cases. Second, saturation magnetization vs temperature was then measured from 300 K down to 2 K at a fixed field of 1 kOe. All of the magnetization values in Table I and the magnetization data below are based on a nominal film thickness of 50 nm for all the samples.

Finally, in order to determine the threshold nitrogen level needed for uniaxial anisotropy and determine the uniaxial anisotropy field values for samples above this threshold, additional hysteresis loop data were obtained at 300 K for both easy and hard direction fields. Samples with $x_N \geq 3.9$ at. % showed uniaxial anisotropy. Those with $x_N < 3.9$ at. % showed no uniaxial anisotropy. The coercive force values from the easy direction hysteresis loop measurements were also used to estimate values of the cubic and uniaxial anisotropy energy density parameters based on established coercive force models. Anisotropy nomenclature will be introduced as needed in Secs. V and VI.

Room temperature ferromagnetic resonance measurements at 9.5 GHz were used to check the uniaxial anisotropy field values for the high nitrogen content samples. The FMR profiles were measured by a shorted waveguide reflection technique^{24,25} with field modulation and lock-in detection. The samples were mounted on the waveguide-short such that the external static and microwave fields were in the plane of the films and mutually perpendicular. The raw data consisted of plots of the field derivative of the FMR absorption peak response as a function of applied field. The resonance field position was determined from the zero crossing point on the derivative profile. Data were obtained as a function of the in-plane static field orientation in 10 degree steps over a half-circle. The FMR field position vs angle was then used to obtain the uniaxial anisotropy field parameter H_u . For films with $x_N < 3.9$ at. %, the derivative FMR profiles were too broad and the shifts in the FMR field position with angle were too small to obtain usable values of H_u .

Table I shows a summary of basic film parameters as a function of the nitrogen level. The nitrogen content and grain

TABLE I. Summary of sample parameters as a function of nitrogen content. The nitrogen content and grain size for different films were obtained from XPS and TEM measurements at the MINT Center, University of Alabama. Other parameters were obtained from SQUID and FMR measurements as part of this work. These parameters are discussed in detail in Secs. IV and V.

Nitrogen content x_N (at %)	Grain size D (nm)	Saturation induction $4\pi M_s(300\text{ K})$ (kG)	Spin-spin exchange energy J_{ex} (10^{-15} erg)	Coercive force $H_c(300\text{ K})$ (Oe)	Hard axis hysteresis loop determined uniaxial anisotropy field parameter $H_u(300\text{ K})$ (Oe)	FMR Uniaxial anisotropy field parameter $H_u(300\text{ K})$ (Oe)
0	28	19.4	6.7	13.5		
1.9	20	19.0	4.4	7.5		
3.9	15	18.8	3.7	6.7	7	4.0
5.4	10	18.2	3.0	6	9	6.5
7.0	8.5	16.8	2.5	5.3	11	8.7
8.4	7.5	15.3	2.4	6.5	16	12.5
10.9	5	14.2	2.1	8.5	19	12.5
12.7	4	13.9	2.1	11.0	23	19.0

size shown in the first two columns were obtained from XPS and TEM measurements by Alexander of the University of Alabama MINT Center.²⁶ The other columns show results from the SQUID and FMR measurements. The saturation induction and spin-spin exchange energy results will be considered in Sec. IV. The coercive force and uniaxial anisotropy field results will be considered in Sec. V.

IV. EFFECT OF NITROGEN ON SATURATION INDUCTION

As noted in the Introduction, the initial interest in Fe-N thin films was driven, in large part, by an apparent increase in the magnetization for small additions of nitrogen. Interestingly, there has been little work on the change in the magnetization with the nitrogen level. The use of titanium to achieve thermally stable films makes the current series of films ideal for a full study of the magnetization as a function of the nitrogen content as well as temperature.

There are two parts to this section. The first focuses on the actual data on the saturation induction $4\pi M_s$ vs temperature T for the full series of samples. The second presents an analysis of the $M_s(T)$ response, sample by sample, to give the x_N dependence of the average nearest-neighbor spin-spin exchange interaction for the Fe-Ti-N films. The analysis shows a strong correlation between the expected structural changes in the films with increasing x_N and the exchange. One finds, specifically, that the Heisenberg exchange parameter J_{ex} shows a very strong decrease with increasing x_N up to about 6–8 at. % nitrogen and then shows only a very small change, if any, for larger x_N values. This response is consistent with the expected expansion of the lattice with the addition of nitrogen and a structure change at 6–8 at. %.

A. Nitrogen loading and temperature dependence of saturation induction

Figure 2 shows experimental results on the saturation induction vs temperature and nitrogen level. The data for each sample were obtained as a decreasing function of temperature and for a constant in-plane field H of 1 kOe. Graph (a) shows the full ensemble of data in a $4\pi M_s(T)$ format for all of the samples, with the x_N values as indicated. Graph (b) shows selected data in $4\pi M_s$ vs x_N format at two specific

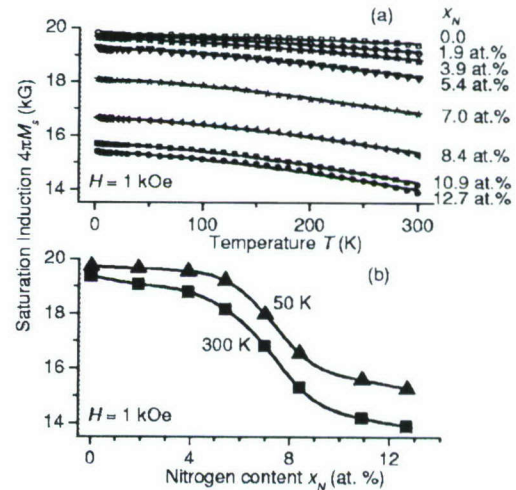


FIG. 2. (a) Saturation induction $4\pi M_s$ as a function of temperature T for films with different nitrogen concentrations (x_N), as indicated. The data were obtained for an in-plane field H of 1 kOe and taken as a decreasing function of temperature. The solid lines show Bloch $T^{3/2}$ law fits. (b) Variation in $4\pi M_s$ with x_N at 50 K and 300 K. The curves provide a guide to the eye only.

temperature points, 50 K and 300 K. The solid curves in (a) represent fits to a Bloch $T^{3/2}$ law. The curves in (b) are a guide to the eye.

Figure 2(a) shows four things. First, at a given x_N level, $4\pi M_s$ is a decreasing function of temperature. Second, the $4\pi M_s(T)$ response can always be fitted nicely to a Bloch $T^{3/2}$ type response. Third, the curvature of the $4\pi M_s(T)$ response generally increases with x_N . This is an indication that the exchange coupling is a decreasing function of x_N . Finally, at any given temperature, $4\pi M_s$ generally decreases with increasing nitrogen content. There is never an increase in $4\pi M_s$ with x_N .

Figure 2(b) elaborates on the last point made above. These data show that the $4\pi M_s$ vs x_N response at fixed temperature shows an interesting structure. In particular, the 50 and 300 K data both show a gradual decrease in $4\pi M_s$ up to about $x_N=6$ at. %, followed by a rather rapid change in the $x_N=6-8$ at. % range, and then a gradual leveling off for higher x_N values. It is also useful to take note of the numerical values in graph (b). First, the $4\pi M_s$ value at 300 K and $x_N=0$ is about 19.5 kG. This value is very close to the $4\pi M_s$ value of 21 kG for pure α -Fe noted above. The small difference is attributed to the nonmagnetic titanium in these films. Second, one can see that there is very little scatter in the point-to-point data for either temperature. Keep in mind that all of the data are for different films with assumed nominal thicknesses of 50 nm. The lack of scatter indicates that all of the films have the same thickness to within a few percent or so. This means that overall, the $4\pi M_s$ data in Fig. 1 show the true relative response for the different x_N values.

Turn now to the Bloch $T^{3/2}$ law fits in Fig. 2(a). Within the framework of the Heisenberg exchange spin-wave model for a three-dimensional ferromagnetic system at temperatures well below the Curie temperature, the temperature dependence of the saturation induction can be written as²⁷

$$4\pi M_s(T) = 4\pi M_{s0}(1 - BT^{3/2}). \quad (1)$$

Here, $4\pi M_{s0}$ is the extrapolated saturation induction at $T=0$ and B is the Bloch coefficient. The B parameter allows one to test the experimental response against the spin-wave model and quantify the curvature of the $4\pi M_s(T)$ response. As noted above, the solid line fits to the Bloch law in Fig. 2(a) are quite good. The R^2 (correlation coefficient squared) of the fit for the $x_N=0$ film is equal to 0.96 and for all other films, this value is above 0.99. These fits, in turn, yield empirical values of $4\pi M_{s0}$ and x_N as a function of x_N . The fitted $4\pi M_{s0}$ as a function of x_N shows the same basic response as the Fig. 2(b) data at 50 K, but with values that are slightly above the points shown. The fitted B values range from $(3.1 \pm 0.4) \times 10^{-6} \text{ K}^{-3/2}$ at $x_N=0$ to $(17 \pm 1) \times 10^{-6} \text{ K}^{-3/2}$ at $x_N=12.7$ at. %. The overall $B(x_N)$ response is essentially linear up to $x_N=10.9$ at. % and then appears to level off. The value for $x_N=0$ closely matches literature value for bulk α -Fe, $B_{\alpha\text{-Fe}} = 3.3 \times 10^{-6} \text{ K}^{-3/2}$.²⁸ The increase in the B parameter with x_N is an indication of a decrease in the average exchange interaction between the spins. A quantitative analysis of the $B(x_N)$ results in terms of exchange will be considered below.

It is useful to note that for, temperatures well below the Curie temperature T_c , Eq. (1) may also be written in terms of T_c instead of the Bloch parameter B according to $4\pi M_s = 4\pi M_{s0}[1 - 0.1167(T/T_c)^{3/2}]$.²⁹ The conversion yields $T_c = 1055 \pm 90 \text{ K}$ at $x_N=0$, in nominal agreement with the known Curie temperature for iron.²⁷

Finally, consider the $4\pi M_s$ vs $x-N$ responses in Fig. 2(b). The $4\pi M_s(x_N)$ profile follows the same decreasing trend with x_N that has been reported for binary Fe-N films prepared by dc magnetron sputtering.¹³ In this context, one should note that an increase in $4\pi M_s$ was observed in rf sputtered and molecular beam epitaxy deposited films.^{11,20} Therefore, after the discussion in Ref. 14, it is likely that the preparation technique plays an important role in setting the $4\pi M_s$ vs x_N response. In case of ternary Fe-Ti-N, the decrease in $4\pi M_s$ with increasing x_N at a given temperature can be attributed to the magnetic dilution caused by more and more nitrogen on interstitial sites. One can surmise, moreover, that the rapid change in $4\pi M_s$ in the $x_N=6-8$ at. % range is indicative of some sort of a structural transition. Such a transition is, in fact, reflected in the exchange response as a function of the nitrogen content. The following section considers the actual exchange energy parameter J_{ex} as a function of x_N .

B. Variation in the spin-spin exchange energy with nitrogen content

The standard starting point for a spin-wave analysis for $M_s(T)$ is a mean-field nearest-neighbor Heisenberg Hamiltonian of the form

$$\mathcal{H} = -2J_{\text{ex}} \sum_i \mathbf{S}_i \cdot \mathbf{S}_{i+1}, \quad (2)$$

where the \mathbf{S}_i denote individual lattice site spins. From the standard Heisenberg analysis,²⁷ one obtains an $M_s(T)$ as given in Eq. (1) with a $J_{\text{ex}}-B$ connection given by

$$J_{\text{ex}} = \left(\frac{k_B}{2S} \right) \left(\frac{SQB}{0.0587} \right)^{-2/3}. \quad (3)$$

In the above, k_B is the Boltzmann constant, S is the dimensionless spin value for the site, and Q is the number of atoms per cubic unit cell in the lattice. The numerical factor derives from the boson statistics for spin waves. For bcc iron, one has $S=5/2$ and $Q=2$. This isotropic mean-field model is taken to be applicable for polycrystalline films of the sort used here. The important point for this discussion is that J_{ex} varies as $B^{-2/3}$. This means that the linear increase in B with x_N noted above will translate into a nonlinear decrease in J_{ex} with x_N .

One final caveat is needed. Equation (3) is explicitly for a bcc structure. In accord with the $4\pi M_s(x_N)$ data in Fig. 2(b), the J_{ex} results indicate the possibility of a structure transition that will, in turn, invalidate the specific form of Eq. (3). This point will be revisited at the end of the section.

Figure 3 shows the change in J_{ex} with x_N from the data fits to Eq. (1) and the conversion in Eq. (3). The open circles show the J_{ex} values obtained for a bcc structure. An exponential fit, as specified in the caption, is shown by the solid

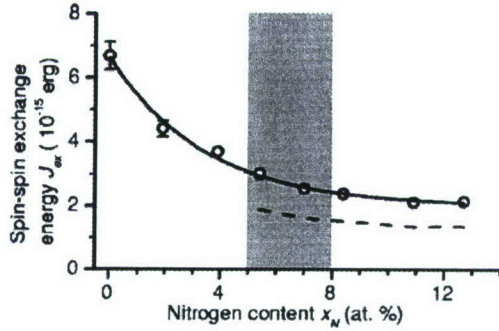


FIG. 3. Spin-spin exchange energy J_{ex} as a function of nitrogen content x_N . The open circles show the application of the Heisenberg model to the measurement results. The solid line shows a best fit based on an exponential decay function of the form $U + Ve^{-Wx_N}$ with $U = 2 \times 10^{-15}$ erg, $V = 4.6 \times 10^{-15}$ erg, and $W = 0.3$. The shaded region for $5 < x_N < 8$ at. % indicates a possible bcc to bct structural transition region. The errors for the points without error bars are smaller than the size of the symbol. The dashed line shows the inferred J_{ex} values if the bcc to bct transition is taken into account according to the discussion in text.

curve. The gray shading in the $5 < x_N < 8$ at. % range is shown to indicate a possible structural transition. The dashed line indicated the revised J_{ex} vs x_N response for $x_N > 5$ at. % that one obtains if the working formula is revised to match a bct lattice. This point will be revisited shortly at the end of this section.

In line with the discussion above, the overall decrease in J_{ex} with increasing x_N can be attributed to the increase in the spin-spin distance as the added interstitial site nitrogen causes the lattice to expand. The strong decrease in J_{ex} for $x_N < 5$ at. % or so, indicates an increase in the average spin-spin distance in this range. For higher concentrations, the apparent leveling off in J_{ex} indicates that some sort of transition has occurred. As noted in Sec. II, there is a structural transition somewhere in the $0.4 < x_N < 11$ at. % range for Fe-N, and it is reasonable to expect a similar effect for Fe-Ti-N. X-ray data by Ding *et al.*,⁶ on films similar to those studied here do indicate a structural change.

What do these data mean? After the discussion of Sec. II, it is clear that the random distribution of the nitrogen atoms at the octahedral interstices first distorts the bcc structure for relatively low x_N levels and then results in a bcc to bct structural transition at large x_N . Recall that the $4\pi M_s(x_N)$ data in Fig. 2(b) also indicate a possible structure transition in the $5 < x_N < 8$ at. % range. Based on these considerations and the results in Fig. 3, the overall $J_{\text{ex}}(x_N)$ response can be explained as follows. (1) At small values of x_N , likely below 5 at. % or so, there is a dilation in the overall bcc lattice due to an increase in the Fe site-to-site distance induced by the presence of the interstitial nitrogen, and this dilation causes J_{ex} to decrease rapidly. (2) As x_N moves above 5 at. % or so, the structural transition suggested in Ref. 6 and evident from Fig. 2(b) causes an apparent leveling off in the $J_{\text{ex}}(x_N)$ response. As noted above, however, a structural transition invalidates the rigorous use of Eq. (3) to extract a J_{ex} from the fitted Bloch coefficient B with the Q value of 2 for a bcc lattice. This means that the numerical values of J_{ex} in Fig. 3

for large x_N levels may not be strictly applicable.

Because of the structural transition from the distorted bcc to a bct phase in the $5 < x_N < 8$ at. % range, and as just noted, one should revise the $B \rightarrow J_{\text{ex}}$ calculation algorithm for x_N levels above the transition point. In order to keep the calculation procedure as simple as possible, however, one can consider the structure of the bct α'' phase as a distorted fcc lattice.¹⁴ In this case, Eq. (3) can still be taken as valid, but with Q increased from 2 to 4. This gives a lowering in the corresponding J_{ex} values for $x_N > 5$ at. %, as shown by the dashed line in Fig. 3. The revised J_{ex} values are lower by a factor of about 1.6 than the previous values. However, this does not modify the overall result of a decreasing J_{ex} vs x_N response.

As an aside, it is useful to recast the exchange parameter J_{ex} in terms of the often-used exchange stiffness constant parameter A . For a bcc lattice, the A - J_{ex} connection is given by $A = 2J_{\text{ex}}S^2/a$, where a is the lattice parameter.³⁰ The A format is used extensively and one can readily compare present results with values in the archival literature. Typical A values for many materials, from metals to insulators, are in the 10^{-6} erg/cm range. For α -Fe, one has $A = 2.1 \times 10^{-6}$ erg/cm,³¹ for example. For Fe-Ti films, Ding *et al.*¹⁰ report an a value of 2.878 Å. Based on the J_{ex} results in Fig. 3, this gives $A = (2.9 \pm 0.2) \times 10^{-6}$ erg/cm at $x_N = 0$.

V. COMPETITION BETWEEN CUBIC AND UNIAXIAL ANISOTROPY

This section focuses on the effect of the nitrogen level on the cubic and the field induced uniaxial anisotropy. Both ferromagnetic resonance and hysteresis loop results are considered. Nitrogen is known to affect the magnetic anisotropy in Fe-N and Fe-Q-N films. The bcc $x_N = 0$ film has a predominant cubic magnetocrystalline anisotropy and no measurable field induced uniaxial anisotropy. As x_N is increased from zero and nitrogen goes to the interstitial sites, there is a local breaking of the cubic symmetry. This symmetry breaking might cause a reduction in the usual cubic anisotropy. At the same time, the interstitial nitrogen, in combination with film deposition in a field, gives rise to a uniaxial anisotropy. Further, it is well known that the grain size governs the anisotropy in the nanocrystalline systems. As discussed earlier, the nitrogen also serves to slow the grain growth in the Fe-Ti-N system. This gives the grain size decrease with increasing nitrogen content shown in Table I.

There are two parts to this section. Section V A presents room temperature FMR results that show a clear signature of a deposition field induced uniaxial anisotropy. The uniaxial field parameter increases with x_N for nitrogen levels above about 4 at. %. Section V B presents room temperature hysteresis loop results. The easy direction loop based coercive force data and the hard direction loop anisotropy data for $x_N \geq 3.9$ at. % reveal systematic changes in both the cubic and uniaxial anisotropy with nitrogen content as well as a competition between these anisotropies. Both results are consistent with the considerations outlined above. Section VI will provide a semiquantitative analysis of these results in terms of energy density considerations.

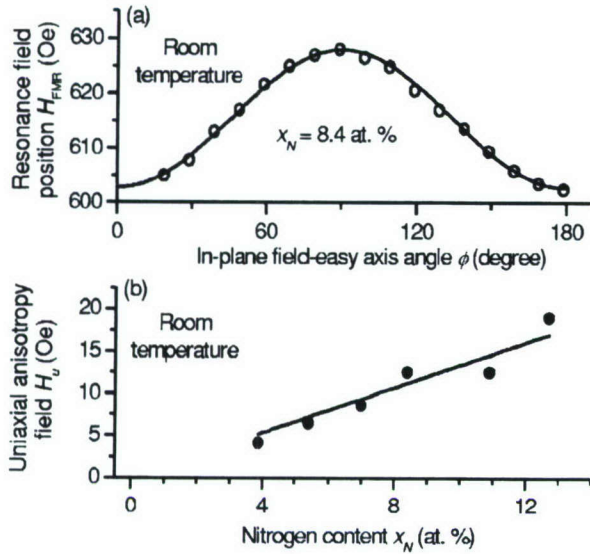


FIG. 4. (a) Room temperature FMR resonance position H_{FMR} as a function of the angle ϕ between the in-plane field and easy direction for the $x_N = 8.4$ at. % film. The solid curve shows the fit to Eq. (4) with $4\pi M_s = 15.3$ kG and $H_u = 12.5$ Oe. (b) Uniaxial anisotropy field parameter H_u as a function of nitrogen content x_N . The solid line shows a linear fit to the data.

A. Microwave results

Measurements of the fixed frequency FMR field H_{FMR} as a function of the angle ϕ between the in-plane applied field and the easy axis can be used to determine the uniaxial anisotropy field parameter H_u . For iron based films and x -band frequencies, the operational FMR formula that connects H_{FMR} , ϕ , and H_u can be written as³²

$$\omega_{FMR} = |\gamma| \sqrt{4\pi M_s (H_{FMR} + H_u \cos 2\phi)}, \quad (4)$$

where ω_{FMR} is the resonance frequency and γ is the electron gyromagnetic ratio for the material. For most transition metal alloys, one can make the pure spin approximation and use a nominal spin only $|\gamma|/2\pi$ value of 2.8 GHz/kOe. It is important to emphasize that Eq. (4) is valid only if two conditions are satisfied, (1) a saturated film and (2) $4\pi M_s \gg H_{FMR}$. Subject to these conditions, fits from Eq. (4) to data on H_{FMR} as a function of ϕ can be used to determine H_u . The data show that for the films with $x_N \geq 3.9$ at. %, there is generally a clear in-plane uniaxial anisotropy for these field deposited films. As noted in Sec. III, the FMR linewidths for films with $x_N < 3.9$ at. % were too broad to obtain a discernable $H_{FMR}(\phi)$ response or usable values of H_u .

Figure 4 shows room temperature microwave results for samples with $x_N \geq 3.9$ at. %. Graph (a) shows representative FMR resonance position vs angle data for one particular film with $x_N = 8.4$ at. %. The open circles show the data and the solid curve shows a best fit from Eq. (4). The curve shown is for $4\pi M_s = 15.3$ kG, as obtained from the room temperature saturation induction measurements discussed in Sec. IV and an H_u value of 12.5 Oe. The R^2 value for the fit was 0.99. Graph (b) shows the full ensemble of microwave results on H_u as a function of x_N , based on data and fits similar to those

in (a). The solid line shows a linear fit to the data shown. Films with $x_N < 3.9$ at. % showed no measurable uniaxial anisotropy.

The results in Fig. 4 show that (1) the FMR field vs in-plane easy axis-field angle data fit nicely to a uniaxial anisotropy model, and (2) the uniaxial anisotropy field parameter H_u appears to increase with x_N for $x_N \geq 3.9$ at. %. The response is approximately linear. The slope of the fitted line in Fig. 4(b) is 1.3 Oe/at. %. This increase is consistent with a picture of localized tetragonal distortions to the lattice induced by nitrogen additions and a directional ordering of these local regions for field deposited films.

It is important to emphasize that these FMR determinations of H_u vs x_N are done for saturated samples. In contrast with the hysteresis results in the next section, models based on magnetization processes do not enter into the results.

It is also important to note here that FMR field position data on polycrystalline films cannot be used to access the cubic anisotropy. The cubic anisotropy can be estimated from FMR linewidth data and a two magnon scattering analysis.^{33,34} The focus of this paper is on static properties rather than FMR losses and related mechanisms. Brief remarks on the connection between results reported in Refs. 33 and 34 and cubic anisotropy determinations from the hysteresis loop data will be given in the next section.

B. Hysteresis loop results

Hysteresis loop measurements as a function of the field angle also provide information on anisotropy. Ideally, easy direction in-plane fields will give square loops with a coercive force H_c . One can use easy direction H_c data to estimate either the uniaxial anisotropy energy density parameter K_u or the cubic anisotropy energy density parameter K_1 , depending on which one is dominant. If the cubic anisotropy plays the dominant role in the magnetization processes, hard direction hysteresis loops will be similar to the easy direction loops. If, however, uniaxial anisotropy plays the dominant role, the ideal hard direction loop response will take the form $M = (M_s/H_u)H$ for $H < H_u$ and $M = M_s$ for $H > H_u$. Here, M is the magnetization and H is the static external field. For non-ideal uniaxial systems with, for example, interactions between misaligned grains, these ideal hard direction uniaxial loops will be somewhat widened and the apparent H_u values will be somewhat larger. The data below will show this effect.

The hysteresis loops look quite different for the films with $x_N < 3.9$ at. % and those with greater amounts of nitrogen. Figure 5 shows representative 300 K easy and hard direction in-plane field hysteresis loops for samples below and above this cut. The data are shown in a normalized $M(H)/M_s$ format. Graph (a) is for $x_N = 1.9$ at. % and (b) is for $x_N = 7$ at. %. The solid and dashed lines in each graph show the easy and hard direction loop data, respectively. The loops in (a) are quite square and nearly identical, and with a coercive force of about 7.5 Oe. The fact that the sample shows no evidence of uniaxial anisotropy is consistent with the FMR results.

The loops in (b), on the other hand, have a clear uniaxial anisotropy signature. The saturation point for hard direction

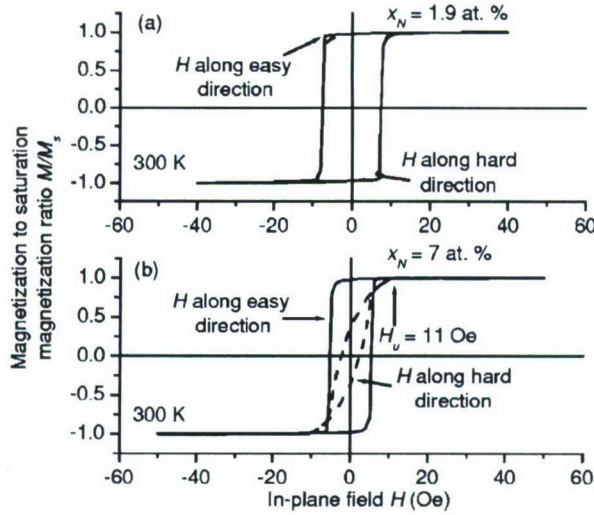


FIG. 5. Example of room temperature hysteresis loops of the magnetization M , normalized to the saturation magnetization M_s , as a function of the in-plane field H for two Fe-Ti-N films. Graphs (a) and (b) are for nitrogen contents (x_N) of 1.9 at. % and 7 at. %, as indicated. The solid and dashed lines show the data for easy and hard direction fields, as indicated. The hard direction saturation field indicated in the first quadrant of (b) is taken as the uniaxial anisotropy field parameter H_u for the sample.

loop in (b) is taken as the H_u parameter for the sample. The easy direction loop is nearly square and the coercive force is about 5 Oe. The saturation point at 11 Oe noted for the hard direction loop is consistent with the 9 Oe value for H_u obtained by FMR. One can also note that the hard direction loop in (b) has an open character. This is an indication of a fairly high degree of anisotropy dispersion for these polycrystalline films.

Figure 6 shows summary data from the hysteresis loop measurements for all samples. The solid square data in (a) show results on the coercive force H_c values from the easy direction loops as a function of the nitrogen content x_N . The inset shows the same H_c data, but plotted as a function of the average grain size D from Table I. The solid curve in the inset shows a fit to a model function $H_c(D) = X + YD^6$. Following Herzer and co-workers,^{35,36} a D^6 response would be expected for a system of randomly oriented single-domain interacting cubic grains. Keep in mind that the large grain size end of the inset graph corresponds to low nitrogen and the low grain size region corresponds to high nitrogen. These H_c vs D data and the fit shown will be important for the discussion below.

In Fig. 6(b), the solid triangles show the H_u vs x_N results from the hard direction loops for the samples with $x_N \geq 3.9$ at. %. The solid circles show the corresponding H_u vs x_N results from the FMR measurements. The solid straight lines represent linear fits to the respective sets of data. The open square points and the dashed lines show the H_u vs x_N prediction based on a Stoner-Wohlfarth (S-W) random uniaxial grain model.³⁷ This model suggests a coercive force to anisotropy field conversion recipe given by $H_c = 0.479H_u$.

In Fig. 6(a), one sees that the coercive force decreases with increasing nitrogen content for low x_N values, goes

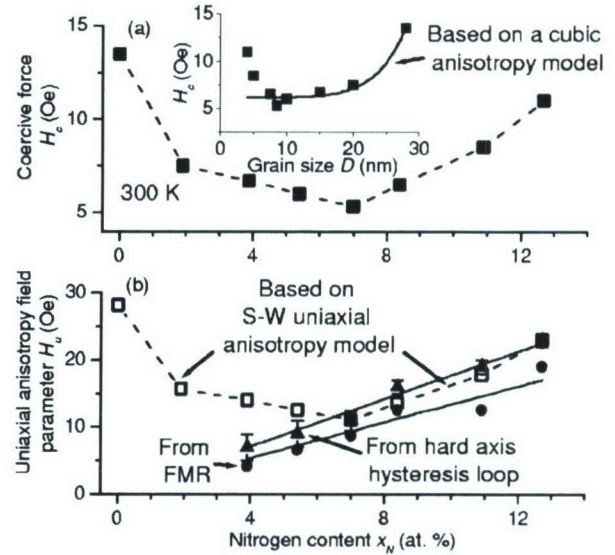


FIG. 6. (a) Coercive force H_c as a function of nitrogen content x_N at 300 K. The solid squares show the data. The inset shows H_c as a function of grain size D . The solid line shows a fit based on $X + YD^6$, with $X = 6$ Oe and $Y = 1.53 \times 10^{34}$ Oe/cm⁶. (b) Uniaxial anisotropy field parameter H_u as a function of x_N . The solid triangles show the H_u values from the hard axis hysteresis loop data. The solid circles show the FMR based H_u values from Fig. 4(b). The solid lines show linear fits to these two data sets. The open squares show inferred H_u values based on the H_c data in (a) and a Stoner-Wohlfarth model for randomly oriented noninteracting uniaxial grains. The dashed lines give a guide to the eye.

through a minimum for $x_N \approx 7$ at. % film, and then increases for higher concentrations. This type of response has been confirmed by separate measurements by the Alabama group²⁶ and is also found for Fe-Zr-N films.²³ The same data in an H_c vs D format, and the fit to the random cubic grain model, serve to illustrate the possible cubic anisotropy origin of the H_c vs x_N response at low nitrogen levels and the need for another mechanism at high x_N . The fit shows that the data for $7.5 \text{ nm} \leq D \leq 28 \text{ nm}$ and $8.4 \text{ at. \%} \geq x_N \geq 0$ matches such a model, and that there are significant deviations from the predictions of a random cubic grain coercive force model for smaller grain sizes and higher nitrogen levels.

Figure 6(b) provides complimentary information based on uniaxial anisotropy considerations. The data show good consistency between the hard axis hysteresis loop saturation field H_u points for $x_N \geq 3.9$ at. % and the FMR results. The up shift for the hysteresis loop data can be attributed to the choice of the hard direction loop saturation field as a measure of H_u . The slope of the fit to the loop results is about $1.8 \pm 0.1 \text{ Oe/at. \%}$. This consistency is noteworthy, insofar as the loop data involve magnetization processes that take a high dispersion sample from a partially magnetized state to a saturated state, while the FMR data are for saturated samples at high field.

The H_u vs x_N response shown by the open square points and connecting lines in graph (b), estimated on the basis of the S-W randomly oriented uniaxial anisotropy model, follow the similar trend as the H_c data in (a). The more interesting aspect is that these points appear to match the actual

H_u data reasonably well for $x_N \geq 7$ at. %. For lower x_N values, this model gives a rapidly increasing H_u prediction that is completely different from the data trend.

These data provide several previously unrealized connections between nitrogen content and anisotropy in Fe-Ti-N films. Keep in mind that an increasing x_N level has two effects. It produces an emerging uniaxial anisotropy for x_N values above 4 at. % or so. At the same time, the induced tetragonal distortion is also expected to ameliorate the sizable cubic anisotropy that is present for the pure Fe-Ti system. The main graph in Fig. 6(a) shows both effects nicely. The drop in H_c with increasing x_N on the left-hand side of the graph is due to a decrease in the cubic anisotropy. The increase in H_c with x_N on the right-hand side is due to the increase in H_u . The inset results reinforce this scenario. The good fit to the random cubic H_c model for large grain sizes corresponds to the low nitrogen regime where the cubic anisotropy is expected to dominate. As one moves to the low D part of the inset graph, the data depart drastically from the D^6 fit based on cubic anisotropy. This is a signature of the rising uniaxial effects. Viewed as a whole, these data show a clear transition in the coercive force mechanism in the 6–8 at. % nitrogen range.

Figure 6(a) and the discussion above provided arguments for a coercive force based on cubic anisotropy for low x_N values. Figure 6(b) provides parallel arguments for a coercive force origin in the rising uniaxial anisotropy for the high x_N range of compositions. This is the message given by the match up between the data and the S-W random uniaxial grain model predictions for $x_N \geq 7$ at. % or so. The validity of a cubic mechanism for lower nitrogen levels also explains the rapid rise in the S-W model prediction away from the data at low x_N .

This match up in Fig. 6(b) for $x_N \geq 7$ at. %, however, raises an important question. The FMR derived and the hard direction loop based H_u values shown by the solid points in (b) correspond to the overall uniaxial anisotropy for the entire film in a saturated state. The S-W model and the open points, on the other hand, are based on the random distribution of uniaxial grains. How can these two very different situations give a match? Most likely, the answer lies in the nature of the interactions between the random grains in the film. The same arguments used by Herzer in Refs. 35 and 36 that lead to the cubic random grain model D^6 coercive force response used in (a) would suggest that a large local uniaxial anisotropy is reduced substantially because of the grain-to-grain interactions.³⁸ This would lead to the type of match-up shown, as will be considered further in the next section. From an empirical point of view, this appears directly in the high dispersion in the uniaxial anisotropy evident from the open hard direction hysteresis loop in Fig. 5(b).

VI. ANISOTROPY ENERGY, EXCHANGE LENGTH, AND GRAIN INTERACTIONS

Section V considered FMR and hysteresis loop data and, based on these data, presented qualitative arguments on coercive force origins due to cubic anisotropy at low nitrogen levels and uniaxial anisotropy at high nitrogen levels. This

section provides a more quantitative perspective on these conclusions. The analysis below is based on the classic Néel³⁹ and S-W³⁷ coercive force models for polycrystals with random cubic or uniaxial grains, respectively.

Following Harte³⁸ and Herzer,^{35,36} the usual cubic anisotropy energy density parameter K_1 is replaced by an averaged $\langle K_1 \rangle$ that takes the exchange coupling between the random cubic grains into account. The connection between $\langle K_1 \rangle$ and the local K_1 is related to the grain size D and the so-called ferromagnetic exchange length L_{ex} , defined here as $\sqrt{A/\langle K_1 \rangle}$. For situations with $L_{ex} > D$, one has a $\langle K_1 \rangle/K_1$ ratio that is less than one and on the order of $(D/L_{ex})^{3/2}$. Now add coercive force considerations. As shown by Néel, the coercive force in a system of randomly oriented particles with cubic anisotropy follows the relation $H_c = 0.64K_1/M_s$. For interacting grains, this carries over to $H_c = 0.64\langle K_1 \rangle/M_s$. The coercive force data presented in Sec. V, when cast into a $\langle K_1 \rangle$ vs x_N format, shows this down-scaling effect nicely. These results will be considered shortly.

Similar arguments should apply to polycrystals with a random uniaxial anisotropy. Here, one deals with the corresponding uniaxial energy density parameter $K_u = H_u M_s/2$, but with K_u replaced by $\langle K_u \rangle$ to account for the substantial anisotropy dispersion. Recall that both the open hard direction loops in Fig. 5(b) and the H_u fits to a random uniaxial anisotropy model at high nitrogen levels shown in Fig. 6(b) support a conclusion that there are large fluctuations in the easy axis directions from grain to grain. In this case, the working formula from the classic S-W analysis for noninteracting grains with random uniaxial axes is given as $H_c = 0.96K_u/M_s$. Interactions then give a $K_u \rightarrow \langle K_u \rangle$ replacement just as in the cubic case. The present samples, however, have a field induced rather than a random anisotropy. The interesting point is that the H_u obtained from the random model, as applied to the coercive force data, matches nicely to the H_u values from the hard direction loop and FMR results. The same situation is reflected when all of the data are cast into a K_u or $\langle K_u \rangle$ vs x_N format.

Figure 7 presents results on $\langle K_1 \rangle$ and $\langle K_u \rangle$ vs x_N , as extracted from the coercive force and anisotropy field data in Fig. 6, based on the working relations given above. The open squares and circles show the $\langle K_1 \rangle$ and $\langle K_u \rangle$ values, respectively, as obtained from the easy direction H_c data. The grain size D is marked for the data points for the films with $x_N < 7$ at. %. The solid curve shows a generated line following $\langle K_1 \rangle = 15 \times 10^3 + 3.7 \times 10^{37} D^6$ and a linearized $x_N(D)$ folded in from Table I for $D \geq 10$ nm. Recall that a D^6 exchange coupled random grain response was verified for the H_c data in Fig. 6(a). The solid triangles and circles are from the $H_u \rightarrow \langle K_u \rangle$ conversion, based on the FMR and hard axis hysteresis loop data. The dashed straight line provides a guide to the eye for the more-or-less linear response indicated by the open circle, solid circle, and triangle data points. Note that this line extends through the origin of the graph. The shaded region shows the inferred transition region between cubic anisotropy dominant to uniaxial anisotropy dominant coercive force processes in the $6 < x_N < 8$ at. % range of nitrogen.

Figure 7 underscores three important results. First, the extracted $\langle K_1 \rangle$ values for low x_N are in the range of 15–30

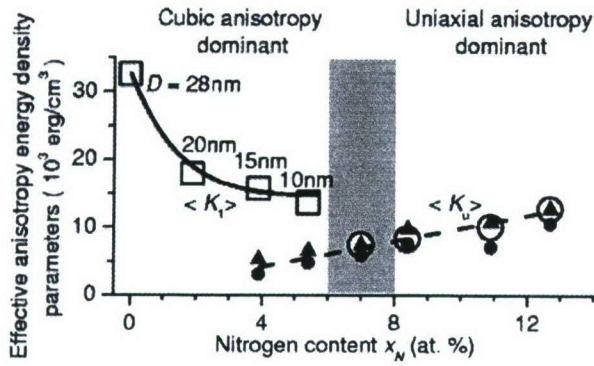


FIG. 7. Effective anisotropy energy density parameters as a function of x_N at 300 K. The open squares and circles show the effective cubic and uniaxial anisotropy energy density parameters $\langle K_1 \rangle$ and $\langle K_u \rangle$, respectively, as obtained from the easy axis coercive force data. The open symbols were made bigger to give a clear visual display of all the points. The grain sizes (D) for low x_N films are as marked. The solid curve shows a generated line of form $\langle K_1 \rangle = X' + Y'D^6$. The solid circles and triangles show the $\langle K_u \rangle$ values from the FMR and hard axis hysteresis loop data, respectively. The dashed line is drawn as a guide to the eye. The shaded region shows the possible changeover region from a dominant cubic to a dominant uniaxial anisotropy.

$\times 10^3$ erg/cm³ or so, much smaller than typical K_1 values for iron and iron alloys with low substitution levels. This order of magnitude reduction in the $\langle K_1 \rangle$ for the low x_N regime is due to the exchange coupling random grain effects noted above. With $L_{ex} = \sqrt{A/\langle K_1 \rangle}$, one obtains an exchange length of about 95 nm for the $x_N=0$ film, that is about 3–4 times higher than the literature value for iron and iron alloys.^{35,40} However, the relation $\langle K_1 \rangle/K_1 \approx (D/L_{ex})^{3/2}$, along with the numerical data given above, gives the single grain K_1 value at $x_N=0$ to be about 200×10^3 erg/cm³, that is the same order as known values for iron.

Second, the fall-off in $\langle K_1 \rangle$ with x_N in this same range appears to match nicely with the D^6 prediction from the exchange coupled random grain model. This match can also be made quantitative. The formulas given above can be combined to give a $\langle K_1 \rangle = (K_1^4/A^3)D^6$ type response. The solid line fit in Fig. 7 corresponds to a function $\langle K_1 \rangle (\text{erg/cm}^3) = X' + Y'[D(\text{cm})]^6$, with $X' = 15 \times 10^3$ erg/cm³ and $Y' = 3.7 \times 10^{37}$ erg/cm⁹. A comparison between the Y' from the fit and the K_1^4/A^3 prediction gives a K_1 value of about 180×10^3 erg/cm³, also in the right range for iron.

Finally, the coercive force data in the $x_N > 4$ at. % regime convert to $\langle K_u \rangle$ values that match the anisotropy energy density parameters extracted from the H_u values from both the FMR and the hard direction loops. These values also match $\langle K_u \rangle$ estimates recently obtained from a two magnon analysis of FMR linewidth data for Fe-Ti-N films.^{33,34} One can see, moreover, that at the low end of this range, the FMR and hard direction loop data give $\langle K_u \rangle$ values that are significantly lower than the $\langle K_1 \rangle$ values inferred from the easy direction loop coercive force data. These larger $\langle K_1 \rangle$ values are the reason that the coercive force origins for the x_N

= 3.9 at. % and $x_N = 5.4$ at. % samples lie in the cubic anisotropy, even though the uniaxial anisotropy dominates the FMR and hard axis loop responses.

The nice match up for the $\langle K_u \rangle$ values for all three types of measurements for $x_N > 7$ at. % reaffirms the dominance of uniaxial anisotropy in this region. The linear increase in $\langle K_u \rangle$ with x_N also reinforces the origin of the uniaxial anisotropy in the field induced directional ordering of the interstitial site nitrogen atoms. From the dashed line in Fig. 7, $\langle K_u \rangle/x_N$ is equal to about 950 ± 150 erg/cm³ per at. % nitrogen. van de Riet *et al.*²² have calculated the averaged single ion uniaxial anisotropy energy for nanocrystalline Fe-Ta-N films to be $\sqrt{15k_B T_s \langle K_u \rangle / 2N}$, where T_s is the temperature of the system during the field induced ordering in-field deposition and N is the concentration of the nitrogen atoms. For sputtering onto substrates at room temperature, the $\langle K_u \rangle/x_N$ ratio from Fig. 7 give an effective uniaxial anisotropy energy per nitrogen atom of about 30 ± 10 J/mole. This is the same value as obtained in Ref. 22 for Fe-Ta-N. Reference 22 also cites values of 38 J/mol for Mn-Bi and 34 J/mol for Fe-C. The reasonable match for these different systems strongly supports a model for the anisotropy based on impurity atom induced structural ordering.

VII. SUMMARY AND CONCLUSION

In summary, the above sections have described the preparation details and measurement results on the fundamental magnetic properties of Fe-Ti-N films with nitrogen concentrations ranging from 0 to 12.7 at. % and a nominal amount of titanium at 3 at. %. The films were deposited by magnetron sputtering in an in-plane field. The focus of this work was on the effect of interstitial nitrogen on the magnetization, the exchange, the coercive force, the cubic magnetocrystalline anisotropy, and the field induced uniaxial anisotropy. The data were obtained from SQUID measurements of the magnetization vs field and temperature and from room temperature FMR measurements.

The magnetization vs temperature data indicate an expansion in the lattice with increasing nitrogen content and a structural transition in the 6–8 at. % nitrogen range. A Bloch spin-wave analysis of these data to give the nearest-neighbor spin-spin exchange energy as a function of x_N also indicates a lattice expansion with nitrogen below about 6 at. % and a leveling off above this level. This is also suggestive of a structural transition.

The hysteresis loop and FMR data show significant and systematic changes in the magnetic anisotropy as a function of nitrogen content. The hard direction saturation field and FMR data show the increase in the uniaxial anisotropy field with nitrogen content for $x_N > 4$ at. %, and no uniaxial character for lower nitrogen levels. The easy direction coercive force H_c shows a decrease with increasing x_N for nitrogen levels below about 7 at. % and then an increase for higher concentrations.

In the low nitrogen regime, H_c scales with the sixth power of the grain size D , more or less as expected for random grains with cubic anisotropy. Extracted values of the averaged cubic anisotropy energy density parameter $\langle K_1 \rangle$ show

both the expected order-of-magnitude reduction from the usual iron-based K_1 values and quantitative agreement with the predicted D^6 response.

In the high nitrogen regime, the H_c values, in combination with predictions from the Stoner-Wohlfarth model, give values of the uniaxial anisotropy field H_u and uniaxial anisotropy energy density parameter that are consistent with both the hard axis and the FMR data. The single ion anisotropy energies extracted from the data are also consistent with the corresponding energies for other systems, and support the origin of the anisotropy from an impurity induced structural ordering model.

ACKNOWLEDGMENTS

Chester Alexander, Jr. and Yunfei Ding of the University of Alabama, MINT Center kindly provided the Fe-Ti-N films for this research as well as extensive work on materials characterization and many useful discussions. One of the referees is gratefully acknowledged for making the authors aware of Ref. 21. This work was supported in part by the U.S. Office of Naval Research, Grant No. N00014-06-1-0889, the U.S. Army Research Office, Grant No. W911NF-04-1-0247, and the Information Storage Industry Consortium (INSIC) EHDR Program.

- ¹D. J. Rogers, S. Wang, D. E. Laughlin, and M. H. Kryder, IEEE Trans. Magn. **28**, 2418 (1992).
- ²A. Chakraborty, K. R. Mountfield, G. H. Bellesis, D. N. Lambeth, and M. H. Kryder, J. Appl. Phys. **80**, 1012 (1996).
- ³B. Viala, M. K. Minor, and J. A. Barnard, J. Appl. Phys. **80**, 3941 (1996).
- ⁴H. Y. Wang, E. Y. Jiang, H. L. Bai, P. Wu, Y. Wang, and F. F. Gong, J. Phys.: Condens. Matter **9**, 8443 (1997).
- ⁵C. Byeon, Y. Ding, and C. Alexander, Jr., IEEE Trans. Magn. **36**, 2502 (2000).
- ⁶Y. Ding, S. C. Byeon, and C. Alexander, Jr., IEEE Trans. Magn. **37**, 1776 (2001).
- ⁷Y. Ding and C. Alexander, Jr., J. Appl. Phys. **91**, 7833 (2002).
- ⁸J. Rantschler, Y. Ding, S. C. Byeon, and C. Alexander, Jr., J. Appl. Phys. **93**, 6671 (2003).
- ⁹J. Rantschler, Ph.D. thesis, University of Alabama, 2003.
- ¹⁰Y. Ding and C. Alexander, Jr., IEEE Trans. Magn. **42**, 5 (2006).
- ¹¹T. K. Kim and M. Takahashi, Appl. Phys. Lett. **20**, 492 (1972).
- ¹²K. H. Jack, Proc. R. Soc. London, Ser. A **208**, 200 (1951).
- ¹³M. Takahashi, H. Shoji, H. Takahashi, T. Wakiyama, M. Kinoshita, and W. Ohta, IEEE Trans. Magn. **29**, 3040 (1993).
- ¹⁴K. H. Jack, J. Appl. Phys. **76**, 6620 (1994).
- ¹⁵R. M. Metzger, X. Bao, and M. Carbucicchio, J. Appl. Phys. **76**, 6626 (1994).
- ¹⁶N. Ishiwata, C. Wakabayashi, and H. Urai, J. Appl. Phys. **69**, 5616 (1991).
- ¹⁷A. Makino and Y. Hayakawa, IEEE Trans. Magn. **31**, 3874 (1995).
- ¹⁸A. V. Mijiritskii and D. O. Boerma, Phys. Rev. B **64**, 035410 (2001).
- ¹⁹J. M. D. Coey and P. A. I. Smith, J. Magn. Magn. Mater. **200**, 405 (1999).
- ²⁰Y. Sugita, K. Mitsuoka, K. Komuro, H. Hoshiya, Y. Kozono, and M. Hanazono, J. Appl. Phys. **70**, 5977 (1991).
- ²¹H. M. Du, P. Wu, E. Y. Jiang, Z. Q. Li, C. Zhao, and H. L. Bai, J. Magn. Magn. Mater. **292**, 227 (2005).
- ²²E. van de Riet, W. Klaassens, and F. Roozeboom, J. Appl. Phys. **81**, 806 (1997).
- ²³A. R. Chezan, Ph.D. thesis, University of Groningen, 2002.
- ²⁴R. Karim, S. D. Ball, J. R. Truedson, and C. E. Patton, J. Appl. Phys. **73**, 4512 (1993).
- ²⁵S. V. Lebedev, C. E. Patton, M. A. Wittenauer, L. V. Saraf, and R. Ramesh, J. Appl. Phys. **91**, 4426 (2002).
- ²⁶Y. Ding and C. Alexander, Jr. (private communication).
- ²⁷C. Kittel, *Introduction to Solid State Physics*, 5th ed. (Wiley, New York, 1976).
- ²⁸S. Gangopadhyay, G. C. Hadjipanayis, B. Dale, C. M. Sorensen, K. J. Klabunde, V. Papaefthymiou, and A. Kostikas, Phys. Rev. B **45**, 9778 (1992).
- ²⁹M. D. Kuz'min, Phys. Rev. Lett. **94**, 107204 (2005).
- ³⁰S. Chikazumi, *Physics of Ferromagnetism* (Oxford University Press, New York, 1997), p. 409.
- ³¹H. Kronmüller and M. Fähnle, *Micromagnetism and the Microstructure of Ferromagnetic Solids* (Cambridge University Press, Cambridge, 2003), p. 17.
- ³²R. Lopusnik, J. P. Nibarger, T. J. Silva, and Z. Celinski, Appl. Phys. Lett. **83**, 96 (2003).
- ³³S. S. Kalarickal, Ph.D. thesis, Colorado State University, 2006.
- ³⁴S. S. Kalarickal, P. Krivosik, J. Das, K. S. Kim, and C. E. Patton, Paper AE-08, 10th Joint MMM/Intermag Conference, January 7–11, 2007, Baltimore, Maryland.
- ³⁵G. Herzer, IEEE Trans. Magn. **26**, 1397 (1990).
- ³⁶G. Herzer and L. K. Varga, J. Magn. Magn. Mater. **215-216**, 506 (2000).
- ³⁷E. C. Stoner and E. P. Wohlfarth, Philos. Trans. R. Soc. London, Ser. A **240**, 599 (1948).
- ³⁸K. J. Harte, J. Appl. Phys. **39**, 1503 (1968).
- ³⁹L. Néel, C. R. Acad. Sci. URSS **224**, 1488 (1947).
- ⁴⁰J. F. Löffler, H. B. Braun, and W. Wagner, Phys. Rev. Lett. **85**, 1990 (2000).

Direct Detection of Nonlinear Ferromagnetic Resonance in Thin Films by the Magneto-Optical Kerr Effect

Thomas Gerrits,¹ Pavol Krivosik,^{2,3} Michael L. Schneider,¹ Carl E. Patton,² and T.J. Silva¹

¹National Institute of Standards and Technology, Boulder, Colorado 80305, USA

²Department of Physics, Colorado State University, Fort Collins, Colorado 80523, USA

³Slovak University of Technology, 812 19 Bratislava, Slovak Republic

(Received 9 January 2007; published 16 May 2007)

The longitudinal magneto-optical Kerr effect is used to obtain a calibrated measure of the dynamic magnetization response over the ferromagnetic resonance (FMR) profile for in-plane magnetized Permalloy films excited with high power in-plane transverse microwave fields at 1.25 to 3.75 GHz and in-plane precession angles up to about 20°. The data provide a profound demonstration of the Suhl threshold effect for parametric spin wave generation for angles above about 14°, the magnetization precession lock-up just above threshold, and the complicated response over the full FMR profile at very high powers.

DOI: 10.1103/PhysRevLett.98.207602

PACS numbers: 76.50.+g, 72.10.Di, 75.30.Ds, 78.20.Ls

Ferromagnetic resonance (FMR) can be separated into two regimes. First, there is the low power small angle response regime that can be described by a linearized damped precession model [1]. Second, there is the high power and generally larger angle response regime that involves Suhl spin wave instability processes and threshold effects [2]. The thresholds can occur at precession angles at fractions of a degree for some single-crystal ferrites [3], or tens of degrees for metallic thin films [4,5].

With the exception of inductive pick-up loop techniques used for some of the early high power work on microwave ferrites [6], the nonlinear Suhl response has generally been inferred from microwave cavity measurements [4]. In recent years, however, new coplanar waveguide (CPW) techniques have been developed to study the FMR response, particularly for metallic ferromagnetic films, in the time domain with step field excitation [7,8] and in the field or frequency domain with cw microwave excitation [1,9]. While CPW excitation is highly attractive for nonlinear dynamics studies, the time domain FMR response to fast rise time step fields does not appear to produce parametric spin waves or show Suhl instability effects, even when the dynamic magnetization deflection angles are in excess of 90° [10,11]. Recent time-resolved FMR measurements on Permalloy films made with large amplitude microwave pulses, however, do indicate a substantial increase in the apparent damping as well as a decrease in the spatially averaged magnetization [12]. These are precisely the effects associated with Suhl processes. Recent work has also demonstrated the use of magneto-optical methods for FMR measurements [13–15].

This Letter reports on a technique for the direct measurement of the quantitative magnetization dynamics associated with nonlinear ferromagnetic resonance (NLFMR) in a thin film under cw microwave excitation in a CPW structure. The method involves a new quantitative analysis of the nonlinear response, obtained by direct longitudinal

magneto-optic Kerr effect (MOKE) measurements of the change in the longitudinal component of the magnetization M_z as a function of the static field, frequency, and microwave field amplitude.

By way of example, specific results are given below for a 20 nm thick Permalloy film and a range of microwave excitation frequencies from 1.25 to 3.75 GHz. The data show the classic near uniform mode linear FMR response for powers below the Suhl threshold, a lock-up in the precession cone at and just above the threshold, and the complicated nonlinear response that occurs at high power. The MOKE-NLFMR method gives quantitative information on the critical precession angle and microwave field amplitude at the onset of the Suhl instability. In combination with theory, the data also yield a determination of the spin wave relaxation rate for the critical modes. One special advantage of the MOKE-NLFMR technique is that the Suhl processes, both at and above threshold, can be identified directly.

The threshold microwave field amplitude for this process, h_{crit} , may be written as

$$h_{\text{crit}} = \Delta H_{\text{FMR}} \left(\frac{2\eta_k}{W_k \omega_M} \right)^{1/2}. \quad (1)$$

Here, ΔH_{FMR} is the half-power FMR field swept line-width and η_k denotes the relaxation rate of the critical spin wave mode. The real positive dimensionless W_k parameter reflects the coupling between the uniform mode and the critical spin wave mode for the thin film geometry [16]. W_k is generally a function of the film parameters, the field, and the frequency. In the present case, W_k is in the 0.1–0.4 range, depending on the pumping frequency. The parameter $\omega_M = \mu_0 \gamma |M_s|$ expresses the saturation magnetization of the film, M_s , in frequency units. Here, μ_0 and γ denote the permeability of free space and the electron gyromagnetic ratio, respectively. Equation (1) shows that a mea-

surement of h_{crit} , coupled with a proper theoretical evaluation of W_k , can yield a determination of the critical mode spin wave relaxation rate. This is one of the key realizations from the Suhl theory.

The 20 nm thick $\text{Ni}_{80}\text{Fe}_{20}$ films were sputter deposited on glass in an in-plane field of 20 kA/m (250 Oe) to define the uniaxial anisotropy easy axis. This ensures a symmetric response around the equilibrium axis even at low bias fields and large pump fields when the bias field is aligned parallel to the easy axis. The films were capped with a 12 nm silicon nitride protective overcoat. Standard magnetometry gave a saturation induction $\mu_0 M_s$ value of 1.07 T (10.7 kG).

The experimental arrangement is shown in Fig. 1. The sample was placed film side down on a CPW structure with the film easy axis parallel to the static field \mathbf{H} and the CPW line axis, as indicated. The film was insulated from the CPW structure with a 1 mm polyimide layer. The microwave pump field \mathbf{h} was applied through the application of 1 kHz square-wave modulated microwave power to the signal line. The amplitude (h) of the pump field was calibrated from the voltage at the CPW output. We measured the magnetization response across the center conductor and found a homogeneous response until close to the edges, where the pump field direction changes from in-plane to out-of-plane.

The longitudinal MOKE setup was composed of an s polarized 800 nm, 4 mW laser beam focused to a 20 μm diameter spot size at the sample, a standard polarization analyzer, a photodiode, and a lock-in amplifier for detection. The magnetization M_z component serves to rotate the plane of polarization of the incident beam slightly, but with little if any elliptical distortion. The M_y component makes no contributions to the polarization change to first order, as we probe the magnetization with incoming s polarization.

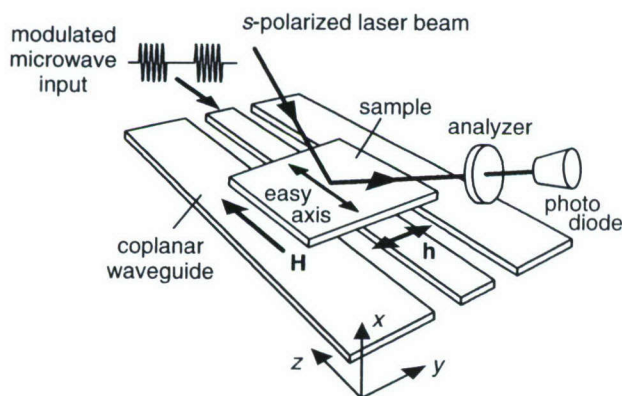


FIG. 1. Schematic of experiment. The thin film is placed on top of a coplanar waveguide (CPW) structure with the film easy axis and the static applied field \mathbf{H} parallel to the CPW line and the z direction. The field \mathbf{h} is generated by the CPW line and the modulated microwave input. The longitudinal magneto-optical Kerr effect detection scheme is shown schematically by the s -polarized laser beam, the analyzer, and the photodiode.

The polar MOKE M_x signal, as well as the quadratic contribution of $M_x \cdot M_y$, average to zero because of the low 10 kHz bandwidth of the photodiode that is far below the nominal 1–4 GHz range of FMR excitation frequencies in the experiments. Possible polarization rotation contributions originating from the glass substrate are subtracted by the nature of the lock-in detection technique. For Permalloy films with an angle of incidence of 45° , the maximum Kerr rotation for a full magnetization reversal is about 500 μrad . For an analyzer setting at 1° off the crossed polarizer-analyzer configuration as used here, the output light intensity is approximately linear in M_z .

Because of the nanosecond time scale for the FMR response and the anticipated parametric Suhl response, in combination with the low bandwidth of the photodiode, the detected signal will correspond to the change in the time averaged z component of the magnetization, taken as $\Delta\langle M_z \rangle$, between the power on and power off time intervals of the square-wave modulation. The raw signals were calibrated against the maximum possible MOKE response obtained by alternatively saturating the film in the $\pm z$ directions. This was done by the application of a symmetric 4.8 kA/m (60 Oe) peak-to-peak square-wave field drive at 2 Hz. The calibrated signal then corresponds to $\Delta\langle M_z \rangle / M_s$. For in-plane magnetized Permalloy films and the range of microwave frequencies used here, the precession cone is effectively flat and constrained to lie in the y - z plane, as defined in Fig. 1. The maximum change in the magnetization z component ΔM_z over a precession cycle, taken as ΔM_z , is then close to $2\Delta\langle M_z \rangle$ and the in-plane precession angle is equal to $\cos^{-1}(1 - \Delta M_z / M_s)$.

Full sets of $\Delta M_z / M_s$ vs H profiles that correspond to the FMR response were obtained for h values from about 70 to 400 A/m (0.9 to 5.0 Oe). The FMR field H_R was obtained as the maximum response point on a given $\Delta M_z / M_s$ vs H profile at low power. The $H_R(\omega)$ response generally matched the thin film FMR condition in the low frequency limit, $\omega = |\gamma| \mu_0 [(H_R + H_k) M_s]^{1/2}$, where H_k is the uniaxial anisotropy field. Fits to this relation gave $|\gamma|$ and H_k values consistent with field-deposited Permalloy films.

Figure 2 gives results for the frequency $\omega/2\pi = 2.25$ GHz. Similar results were found at other frequencies. Figure 2(a) shows $\Delta M_z / M_s$ vs H profiles for the full range of h values noted above. The solid circles identify the maximum $\Delta M_z / M_s$ points from curve to curve. Under the assumption of a constant overall magnetization vector, generally valid only at low power, the numbers on the vertical axis give in-plane precession angles from about 8° at $\Delta M_z / M_s = 0.01$ to about 20° at $\Delta M_z / M_s = 0.06$. The break in the data at $\Delta M_z / M_s \approx 0.03$ and $h = h_{\text{crit}} \approx 130$ A/m (1.6 Oe) corresponds to the Suhl threshold. The in-plane precession angle at this point is about 14° . The corresponding critical ΔM_z value, taken as $\Delta M_{z,c}$, is close to $0.03 M_s$. For h values below 120 A/m (1.5 Oe), the $\Delta M_z(H)$ profiles translate into transverse magnetization amplitude $|m_y(H)|$ response that closely matches linear FMR theory.

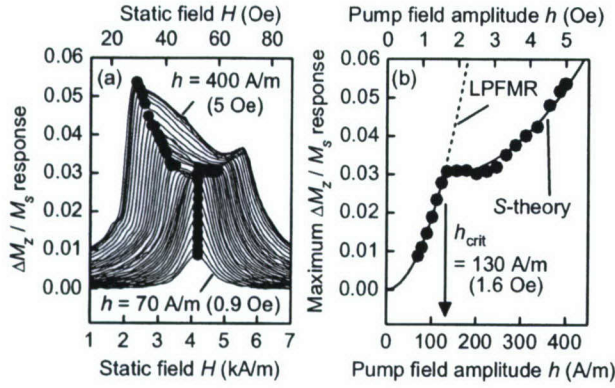


FIG. 2. (a) Collage of profiles of the measured change in the longitudinal magnetization component ΔM_z , normalized to the magnetization M_s , as a function of the static field H for a range of microwave field amplitude h values, as indicated. The maximum values at a given h are shown by the solid circles. (b) Maximum $\Delta M_z / M_s$ values from (a) versus h , with fitted curves from low power FMR (LPFMR) theory and the nonlinear S theory, as indicated. The microwave frequency was 2.25 GHz.

Figure 2(b) shows the maximum $\Delta M_z / M_s$ points from Fig. 2(a) as a function of h . The solid circles show the data. There are three distinct regions: (i) There is a smooth quadratic increase for h values below h_{crit} ; (ii) there is an apparent lock-up in ΔM_z at ΔM_{zc} as h moves from h_{crit} up to about 200 A/m (2.5 Oe); (iii) as h moves to higher h values, the increase in $\Delta M_z / M_s$ resumes. The quadratic increase at low h is related to the linear FMR response. Both the lock-up and resumed increase for $h \geq h_{crit}$ relate to the Suhl NLFMR response. As these data show, the MOKE-NLFMR technique makes all of these responses accessible by simple and direct experimental means, and in a form that is amenable to ready analysis.

Consider the low power response in somewhat more detail. When the anisotropy easy axis is aligned parallel to the bias field direction the transverse m_y response will be linear in h . In the small signal limit, with $|M| = M_s$ and $|m_y| \ll M_s$, one can write $\Delta M_z / M_s \approx |m_y|^2 / 2M_s^2$. The theoretical low power FMR (LPFMR) $\Delta M_z(h)$ response, therefore, is quadratic in h . The dashed LPFMR labeled line in Fig. 2(b) shows a quadratic fit to the data for $h < 130$ A/m. The linear theory gives an overall LPFMR response with $|m_y| \approx 2M_s h / \Delta H_{FMR}$ and $\Delta M_z / M_s \approx 2h^2 / \Delta H_{FMR}^2$. The fit shown corresponds to an FMR linewidth of 980 A/m (12.2 Oe). This value matches the half-power linewidth obtained directly from the low power $|m_y(H)|$ profiles for $h < h_{crit}$.

The lock-up and the high power $\Delta M_z / M_s$ vs h response are related to the above-threshold steady-state dynamics. Various approaches have been used to model this type of nonlinear response. These include a back reaction of the parametric spin waves on the FMR mode [2], nonlinear damping associated with the spin waves [17], and a phase limiting mechanism through what is often called the S theory [18].

Following L'vov [19], the S theory yields a working equation for ΔM_z above threshold of the form:

$$R \frac{\Delta M_z}{\Delta M_{zc}} + \sqrt{\left(\frac{\Delta M_z}{\Delta M_{zc}}\right)^2 - 1} = R \frac{h}{h_{crit}} \sqrt{\frac{\Delta M_z}{\Delta M_{zc}}} \quad (2)$$

The R parameter controls the level of the phase limitation and is on the order of unity. In physical terms, this limitation is due to a power dependent change in phase between the pair of parametrically excited spin waves and the microwave field that results in a decrease in the effective pumping power. There is no phase limitation for $R = 0$ and the lock-up would remain constant at $\Delta M_z = \Delta M_{zc}$. For a very large R , parametric spin wave excitation would be suppressed at any power. The S theory curve in Fig. 2 was obtained for $\Delta M_{zc} / M_s = 0.03$, $h_{crit} = 130$ A/m, and $R = 0.6$. One can see that Eq. (2) models the above-threshold data extremely well with a moderate choice of R . Applications of the first two approaches cited above do not give acceptable fits to the data. Taken more generally, these results may well be an indication that the phase limitation mechanism also plays a dominant role in the large angle dynamic magnetization response in metallic thin films.

Figure 3 summarizes key results for all frequencies. Figures 3(a) and 3(b) show the ΔH_{FMR} and h_{crit} versus frequency results. The lines show linear fits. Figure 3(c) shows the theoretical variation in W_k with frequency from the S theory. The solid circles in Fig. 3(d) show final results on the spin wave relaxation rate η_k versus frequency, based on Eq. (1) and the results in Figs. 3(a)–3(c). As a basis of comparison, the open circles in 3(d) show the uniform mode relaxation rate η_0 versus frequency, and the horizontal line shows the mean η_0 value. The linear frequency dependence for ΔH_{FMR} in Fig. 3(a) is typical for metallic thin films [1]. The slope of the linear fit corresponds to a Gilbert damping parameter α value of about 0.005. The zero-frequency linewidth intercept at $\Delta H_{inh} = 302$ A/m (3.8 Oe) can be ascribed to inhomogeneous line broadening. One can see that the h_{crit} response in 3(b) is also more or less linear in frequency. When combined with the nearly linear W_k versus frequency response in 3(c), along with the effects of the nonzero intercepts in 3(a)–3(c), the end result is an η_k that appears to be relatively level for $\omega / 2\pi > 2.5$ GHz, and drops off at lower frequencies.

The correlation between the η_k results and the intrinsic FMR relaxation rate η_0 is significant. The open circle points come from the working equation that connects the assumed intrinsic FMR linewidth, $\Delta H = \Delta H_{FMR} - \Delta H_{inh}$, to α in the narrow linewidth limit, namely $\Delta H = 2\alpha\omega / |\gamma|$, in combination with the relaxation rate connection applicable in the low frequency limit, $\eta_0 \approx \alpha\omega_M / 2$ [1].

The results in Fig. 3(d) indicate that the critical spin wave mode relaxation rate is more or less frequency independent and very close to the intrinsic uniform mode relaxation rate for frequencies above 2.5 GHz. This indi-

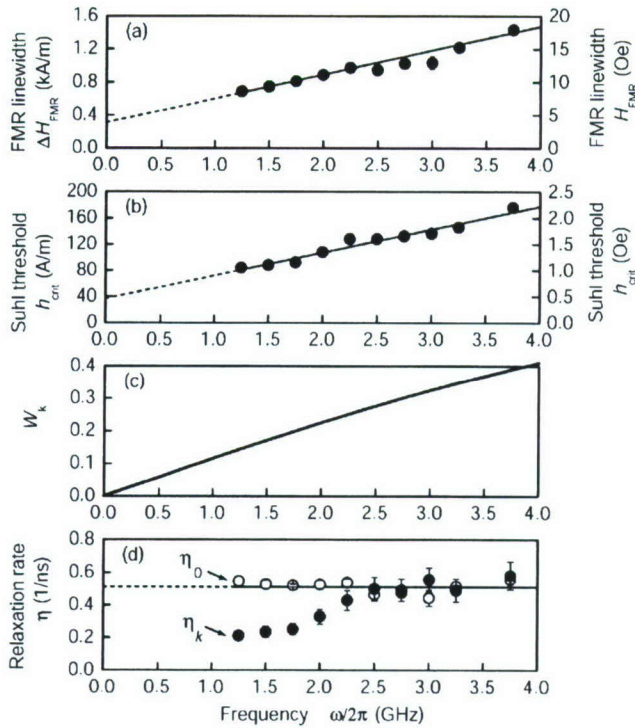


FIG. 3. (a)–(d) show, respectively, the low power FMR linewidth ΔH_{FMR} , the threshold field h_{crit} , the theoretical critical mode coupling factor W_k , and the extracted spin wave relaxation rate η_k versus frequency. The lines in (a) and (b) show a linear fit. (d) also shows the uniform mode relaxation rate η_0 versus frequency.

cates that both the spin wave relaxation rate from the Suhl threshold data and the α -based uniform mode relaxation rate have a common origin. Suhl instability is generally taken to depend on intrinsic relaxation rates. The clear match up between η_k and η_0 , therefore, supports a conclusion that both are due to the magnon-electron relaxation processes that are generally accepted as the source of the intrinsic ferromagnetic relaxation in metals [20]. For frequencies below 2.5 GHz, interestingly, η_k appears to drop off. The important point for this Letter, as noted earlier, is that MOKE-NLFMR allows one to access these behaviors in a direct way. Significant work remains to fully understand the ramifications of these spin wave loss parameters and connections with the FMR loss.

In summary, a new MOKE based analysis for direct nonlinear FMR measurements has been developed. The data reveal a wide range of spin wave instability effects that include clear signatures for the second order Suhl threshold h_{crit} and the above-threshold steady-state response. The h_{crit} values are consistent with fundamental relaxation rate considerations. The response above threshold can be well modeled in terms of dephasing effects, as quantified through the S theory of Zakharov and L'vov.

Anthony Kos is acknowledged for assistance with the measurements. The authors also want to acknowledge Hans Nembach for fruitful discussions during the preparation of this Letter. T. G. was supported in part by the Post-doctoral Program of the German Academic Exchange Service (DAAD). The Colorado State University participants were supported in part by the U. S. Army Research Office, Grant No. W911NF-04-1-0247 (MURI), the Office of Naval Research (USA), Grant No. N00014-06-1-0889, and the INSIC EHDR program.

- [1] See, for example, S. S. Kalarickal, M. Wu, P. Krivosik, C. E. Patton, M. L. Schneider, P. Kabos, T. J. Silva, and J. P. Nibarger, *J. Appl. Phys.* **99**, 093909 (2006).
- [2] H. Suhl, *J. Phys. Chem. Solids* **1**, 209 (1957).
- [3] M. Chen and C. E. Patton, *Nonlinear Phenomena and Chaos in Magnetic Materials*, edited by P. E. Wigen (World Scientific, Singapore, 1994).
- [4] See, for example, S. Y. An, P. Krivosik, M. A. Kraemer, H. M. Olson, A. V. Nazarov, and C. E. Patton, *J. Appl. Phys.* **96**, 1572 (2004).
- [5] H. M. Olson, P. Krivosik, K. Srinivasan, and C. E. Patton, in *Technical Digest of the IEEE International Magnetism Conference*, San Diego, CA, 2006 (IEEE, New York, to be published), p. 77.
- [6] N. Bloembergen and S. Wang, *Phys. Rev.* **93**, 72 (1954).
- [7] T. J. Silva, C. S. Lee, T. M. Crawford, and C. T. Rogers, *J. Appl. Phys.* **85**, 7849 (1999).
- [8] R. Lopusnik, J. P. Nibarger, T. J. Silva, and Z. Celinski, *Appl. Phys. Lett.* **83**, 96 (2003).
- [9] G. Counil, J. V. Kim, T. Devolder, C. Chappert, K. Shigeto, and Y. Otani, *J. Appl. Phys.* **95**, 5646 (2004).
- [10] Th. Gerrits, H. A. M. van den Berg, J. Hohlfield, L. Bär, and Th. Rasing, *Nature (London)* **418**, 509 (2002).
- [11] Th. Gerrits, T. J. Silva, J. P. Nibarger, and Th. Rasing, *J. Appl. Phys.* **96**, 6023 (2004).
- [12] Th. Gerrits, M. L. Schneider, A. B. Kos, and T. J. Silva, *Phys. Rev. B* **73**, 094454 (2006).
- [13] R. Meckenstock, M. Möller, and D. Spoddig, *Appl. Phys. Lett.* **86**, 112506 (2005).
- [14] M. Möller, D. Spoddig, and R. Meckenstock, *J. Appl. Phys.* **99**, 08J310 (2006).
- [15] K. Gnatzig, H. Dötsch, M. Ye, and A. Brockmeyer, *J. Appl. Phys.* **62**, 4839 (1987).
- [16] P. Krivosik, K. Srinivasan, H. M. Olson, and C. E. Patton, in *Technical Digest of the IEEE International Magnetism Conference*, San Diego, CA, 2006 (IEEE, New York, to be published), p. 70.
- [17] J. D. Bierlein and P. M. Richards, *Phys. Rev. B* **1**, 4342 (1970).
- [18] V. E. Zakharov, V. S. L'vov, and S. S. Starobinets, *Sov. Phys. Usp.* **17**, 896 (1975).
- [19] V. S. L'vov, *Wave Turbulence Under Parametric Excitation* (Springer-Verlag, Berlin, 1994).
- [20] V. Kambersky and C. E. Patton, *Phys. Rev. B* **11**, 2668 (1975).